Mechanical Behaviors at Elevated Temperature and Fatigue Strength Analysis of E-Beam PBF Additively Manufactured Ti6Al4V Components

by

Md Jamal Mian

A Dissertation Presented in Partial Fulfillment
of the Requirements for the Degree
Doctor of Philosophy

Approved April 2022 by the
Graduate Supervisory Committee:

Leila Jannesari Ladani, Chair
Abdelrahman Shuaib
Barzin Mobasher
Jafar Razmi
Qiong Nian

ARIZONA STATE UNIVERSITY

August 2022

ABSTRACT

High-temperature mechanical behaviors of metal alloys and underlying microstructural variations responsible for such behaviors are essential areas of interest for many industries, particularly for applications such as jet engines. Anisotropic grain structures, change of preferred grain orientation, and other transformations of grains occur both during metal powder bed fusion additive manufacturing processes, due to variation of thermal gradient and cooling rates, and afterward during different thermomechanical loads, which parts experience in their specific applications, could also impact its mechanical properties both at room and high temperatures. In this study, an in-depth analysis of how different microstructural features, such as crystallographic texture, grain size, grain boundary misorientation angles, and inherent defects, as byproducts of electron beam powder bed fusion (EB-PBF) AM process, impact its anisotropic mechanical behaviors and softening behaviors due to interacting mechanisms.

Mechanical testing is conducted for EB-PBF Ti6Al4V parts made at different build orientations up to 600°C temperature. Microstructural analysis using electron backscattered diffraction (EBSD) is conducted on samples before and after mechanical testing to understand the interacting impact that temperature and mechanical load have on the activation of certain mechanisms. The vertical samples showed larger grain sizes, with an average of 6.6 µm, a lower average misorientation angle, and subsequently lower strength values than the other two horizontal samples. Among the three strong preferred grain orientations of the α phases, <1 1 $\bar{2}$ 1> and <1 1 $\bar{2}$ 0> were dominant in horizontally built samples, whereas the <0 0 0 1> was dominant in vertically built samples. Thus, strong microstructural variation, as observed among different EB-PBF Ti6Al4V samples, mainly resulted in anisotropic behaviors. Furthermore, alpha grain showed a significant increase in average grain size for all samples with the increasing test temperature, especially from 400°C to 600°C, indicating grain growth and coarsening as potential softening mechanisms along with temperature-induced possible dislocation motion. The severity of internal and external defects on fatigue strength has been evaluated non-destructively using quantitative methods, i.e., Murakami's square root of area parameter model and Basquin's model, and the external surface defects were rendered to be more critical as potential crack initiation sites.

ACKNOWLEDGMENTS

I would like to take the opportunity to express my heartiest gratitude to all my colleagues and faculty members who have helped me generously throughout this research approach. I am most indebted to Dr. Leila Ladani, the chair of my dissertation committee, for her continuous support, inspiration, and unparalleled guidance in reaching my research goals. I would also like to thank Dr. Jafar Razmi, a member of my committee, for helping me with his support and motivation during my various experiments. I would like to thank my other committee members Dr. Abdelrahman Shuaib, Dr. Barzin Mobasher, and Dr. Qiong Nian, for their concerns and valuable insights.

Again, I would also like to thank my teachers, advisors, family, friends, and well-wishers for their motivation and inspiration. This research would not have been possible without mental support from my family members and friends, who never get tired of inspiring me. Finally, I thank the University of Texas at Arlington and Arizona State University for allowing me to use various machines and tools for my research. I acknowledge the use of facilities within the Eyring Materials Center at Arizona State University, supported in part by NNCI-ECCS-2025490. I also acknowledge the technical support of Mr. Bill Hayes from Waygate Technologies with the porosity measurements of the specimens using a 3D X-ray computed tomography (CT).

TABLE OF CONTENTS

Page

CHAPTER

CHAPTER Page

APPENDIX

LIST OF TABLES

Table Page

Table Page

LIST OF FIGURES

Figure Page

Figure Page

Figure Page

Figure Page

Figure Page

Figure Page

CHAPTER 1

INTRODUCTION

1.1 Overview of Additive Manufacturing

Additive manufacturing (AM) is the current state-of-the-art in manufacturing and has revolutionized many industries. Key advantages of AM include significant economic benefits due to the reduction in the waste material produced during manufacturing, lower production time and elimination of complex tools, the expedition of the design to the production process, lowering energy cost, and feasibility of complicated and advanced designs that are not feasible with traditional manufacturing [1][2]. Additive processes, as opposed to subtractive processes, involve the building of parts layer by layer. Many different techniques of additive manufacturing have been developed in recent years. However, most of these techniques can be classified as the following: powder bed processes, liquid bed processes, and material deposition processes. Powder bed processes include selective laser melting (SLM), selective laser sintering (SLS), direct metal laser sintering (DMLS), and electron beam processes (EBM). Liquid bed processes are stereolithography (SLA) and digital light processing (DLP). Whereas materials deposition processes include techniques such as material jetting, binder jetting, fused deposition modeling (FDM), and directed energy deposition (DED) [3–5]. Some of the commonly used DED technologies are laser engineering net-shaping (LENS), laser metal deposition (LMD), electron beam welding (EBW), electron beam free-form fabrication (EBF), and wire arc AM (WAAM) [6].

In powder bed fusion (PBF) processes, a thin layer of metal powders is spread on a platform and eventually fused using a power source, as presented in **Figure 1**. Subsequent layers are deposited and melted by lowering the platform step by step until the final desired shape is obtained. Thus, in PBF processes, the desired CAD model is sliced into a large number of individual layers and eventually built in a layer-by-layer fashion, which makes it possible to make easily any complicated component design in a single step in a short lead time. As opposed to traditional processes, which require costly tooling and machining for hard materials, powder bed fusion (PBF) AM processes only require the melting of powder feedstock with a heat source like a laser or electron beam [7]. The use of various processing parameters such as scanning speed, source power, powder layers, sample position, and direction dictates the cooling rates and thermal gradient towards the build table and, eventually, the microstructure of the melt pool and the overall component. Therefore, the mechanical properties and performance of the parts vary from process to process and build to build. However, nowadays, various powder bed fusion (PBF) metal additive manufacturing techniques have gained popularity because of their added advantages over the traditional subtractive manufacturing processes, like milling, drilling, and turning, for fabricating various metal components like Ti6Al4V parts [8–11]. However, significant variability in properties and microstructure in different build processes and also among a single particular process are still a concern for its potential users making the PBF process less popular as compared to the traditional processes. Further, issues involved with this PBF process are discussed in the following problem statement.

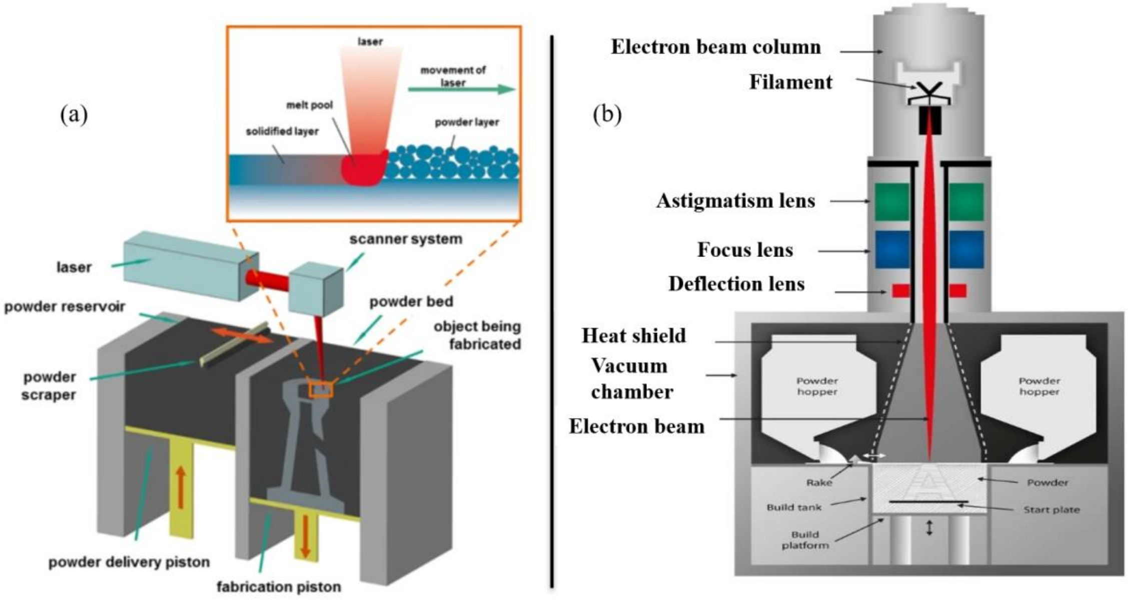

Figure 1 Schematic of the powder bed fusion (PBF) metal additive manufacturing processes, (a) laser-beam (SLM) and (b) electron-beam (EBM) [12,13].

1.2 Importance and Applications of Ti6Al4V Alloy

Titanium alloy Ti6Al4V is a two-phase α+β alloy. The crystal structures of α-phase is hexagonal-close-packed (hcp), and β-phase is body-centered-cubic (bcc). The HCP structures are made of repeated hexagonal unit cells with hexagonal bases and sides of equal length which is called a basal parameter. In contrast, the BCC structures are made of cubes with sides having the same length. The unit cell of the BCC has atoms on each corner and also in the center of it [14,15]. Ti6Al4V falls in the category of α+β alloy since it has a combination of both α (Al) and β (V) stabilizers. A vertical section of the phase diagram of this Titanium alloy is presented in **Figure 2**, in which the β-transus temperature and weight percent (wt%) change in the alpha phase with temperatures in the two-phase field.

The chemical composition of various Ti6Al4V alloys is presented in the **Table 1,** as comparison among different manufacturing processes.

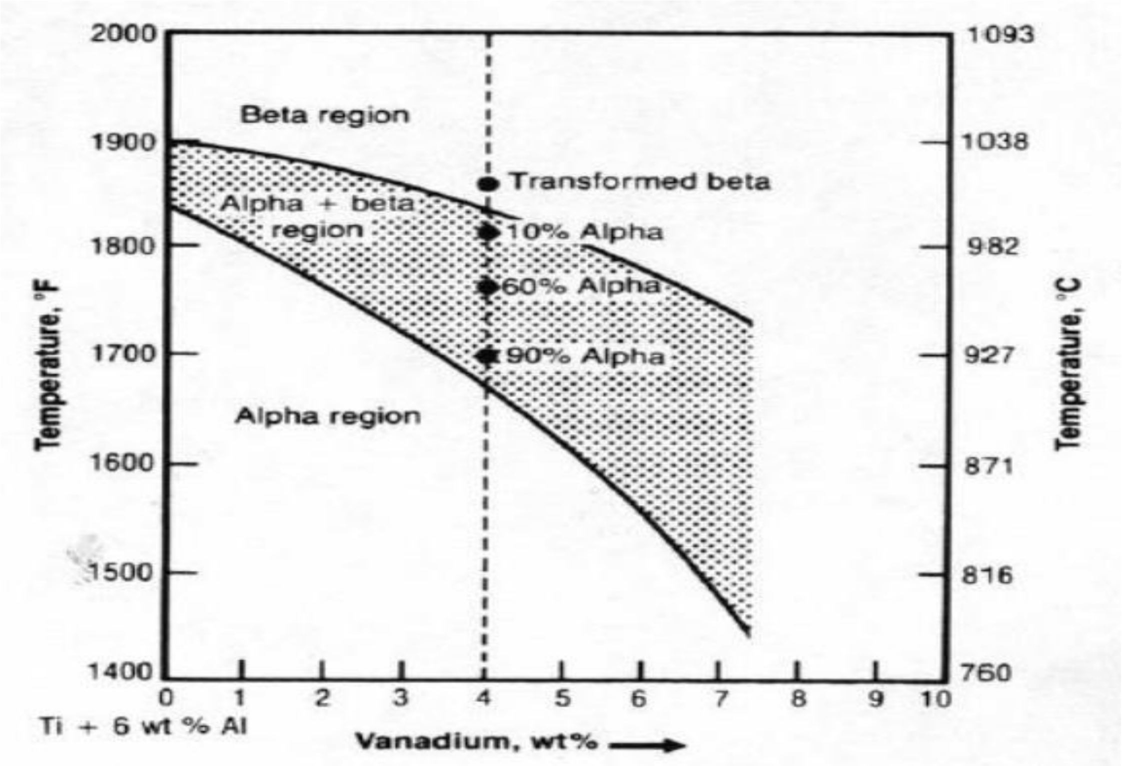

Figure 2 The vertical section of the phase diagram of Ti-6Al-xV, exhibiting β-transus temperature and weight percent (wt%) of Alpha at different temperatures within a two-phase region [14].

Table 1 Chemical composition of Ti6Al4V [16].

Constituents	Cast Material	Wrought Material	Typical Arcam* provided powder
Aluminum, Al	5.5-6.75%	5.5-6.75%	6%
Vanadium, V	3.5-4.5%	3.5-4.5%	4%
Carbon, C	<0.1%	<0.08%	0.03%
Iron, Fe	<0.3%	<0.3%	0.10%

Oxygen, O	<0.2%	<0.2%	0.15%
Nitrogen, N	<0.05%	<0.05%	0.01%
Hydrogen, H	<0.015%	<0.015%	0.003%
Titanium, Ti	Balance	Balance	Balance

*Arcam EBM system is an additive manufacturing (AM) company.

Ti6Al4V alloy has various applications in different critical environments because of its structural efficiency and some of its exceptional mechanical properties like lightweight, high strength, excellent corrosion resistance, and high melting temperature[15,17]. Some of such applications are airframes, jet engines, medical implants, heat exchangers, sports goods, and so on [14][18]. Though Ti6Al4V is mainly used in various weight reduction applications in aerospace, automotive, and marine equipment, it is also used in the biomedical industry as a hard tissue replacement due to its good biocompatibility [19]. However, lately, various PBF processes are being employed extensively for shaping this hard Ti6Al4V alloy, particularly in aerospace and biomedical industries [20].

1.3 Statement of the Problem

Though PBF-produced parts have various added advantages over traditionally produced parts, they also suffer from some crucial issues, like higher surface roughness, internal defects, and mechanical anisotropy, which are preventing them from being widely accepted in various industries [21]. The PBF processed Ti6Al4V parts are also a good candidate for elevated temperature applications because of having high specific strength and high melting temperature. But, in many structural applications of Ti6Al4V parts, where this alloy gets exposed to high-temperature environments, they can undergo variation or degradation in terms of some of their mechanical properties [22–24].

Moreover, PBF-processed Ti6Al4V alloy can be used in different critical environments under different loading conditions, as it has high strength and high corrosion resistance [25][26]. In some of these applications, such as turbine blades, where the material is subject to cyclic mechanical and thermo-mechanical load, fatigue failure and degradation of mechanical strength become critically important [27]. EBM has been utilized extensively for producing Ti-6Al-4V parts because of its higher power and higher speed as compared to other AM methods [28]. This technology has shown possibility in producing similar or better mechanical properties as compared to the traditional manufacturing processes [8].

However, powder bed fusion (PBF) AM processed Ti6Al4V parts are known to possess distinctive microstructure, significant anisotropy, and various inherent defects such as lack of fusion (LOF) porosity, keyhole porosity, and high surface roughness [17,29,30]. Some of these inherent issues of PBF techniques are inhibiting them from being widely adopted in different manufacturing industries [21]. These intrinsic microstructural aspects of PBF processes are very crucial for the resultant mechanical behavior of AM parts, especially under various high-temperature applications. Therefore, analysis of inherent defects and anisotropic microstructural behavior is very important.

Besides, the surface roughness of parts made using the EBM process is typically higher than other PBF processes, which could cause the fatigue performance of EBM-built Ti6Al4V parts to be less optimal [31]. Therefore, analyzing the fatigue performance of AM-built metal parts is very crucial for their successful implementation in these applications. To address some of these issues, an extensive investigation has been conducted in this study in an effort to analyze various inherent manufacturing defects and their impacts on the mechanical and fatigue performance of EBM-built Ti6Al4V parts. Furthermore, potential root causes of the observed anomaly of this alloy and manufacturing process combination have been discussed, and possible insight, resolutions, and future research scopes have been recommended to further improve the metal AM processes towards industrialization.

CHAPTER 2

BACKGROUND LITERATURE

2.1 Powder Bed Fusion Metal AM Processes

Different powder bed fusion (PBF) additive manufacturing (AM) processes have proven to be excellent prospects lately for manufacturing near-net shape Ti6Al4V parts due to their poor machinability in conventional removal techniques [32]. Consequently, many of the issues of the different PBF processed parts, such as SLM and EBM parts, including mechanical behaviors, have been investigated at room temperature by numerous researchers [17,29,33–39]. Electron beam melting (EBM) and selective laser melting (SLM) are the two most popular PBF processes which are being analyzed extensively as alternative manufacturing techniques for the production of complex bulk components. Ti6Al4V parts produced by these two processes exhibit slightly different microstructural and mechanical properties. The SLM processed Ti6Al4V parts generally have a distinctive α'martensitic phase, whereas the EBM processed counterparts have mainly α phase along with a small amount of prior β phase on the grain boundaries [17,40]. These phase variation in microstructures is primarily because of the difference in processing conditions and the difference in cooling rates between these two methods. The cooling rate during the formation of the hcp α-phase from the allotropic transformation of the bcc β-phase dictates the final microstructure of the various PBF parts [41–43]. In the SLM process, the thermal gradient is much higher, resulting in a higher cooling rate, as compared to the EBM process, where the build chamber is kept at an elevated temperature causing a lower thermal gradient [17].

2.2 Microstructure Formation in EBM Process

During the initial solidification of the EBM process, the Ti6Al4V melt pool speedily solidifies into primary β grains when the temperature is still higher than the β-transus temperature (around 980 °C), as shown in **Figure 3**. These prior β (β') grains then transform into the martensitic α' phase following a rapid cooling rate. The martensitic α' phase subsequently decomposes into α colony, α basketweave, and β phases during the solid phase transformation because of a near-isothermal annealing process at the building temperature of around 650 °C [44]. Consequently, the tensile and fatigue properties of Ti6Al4V parts built by this EBM process also differ because of this microstructural variation and changes in orientation and texture of the α and β phases, which depend on the cooling rates[17,40].

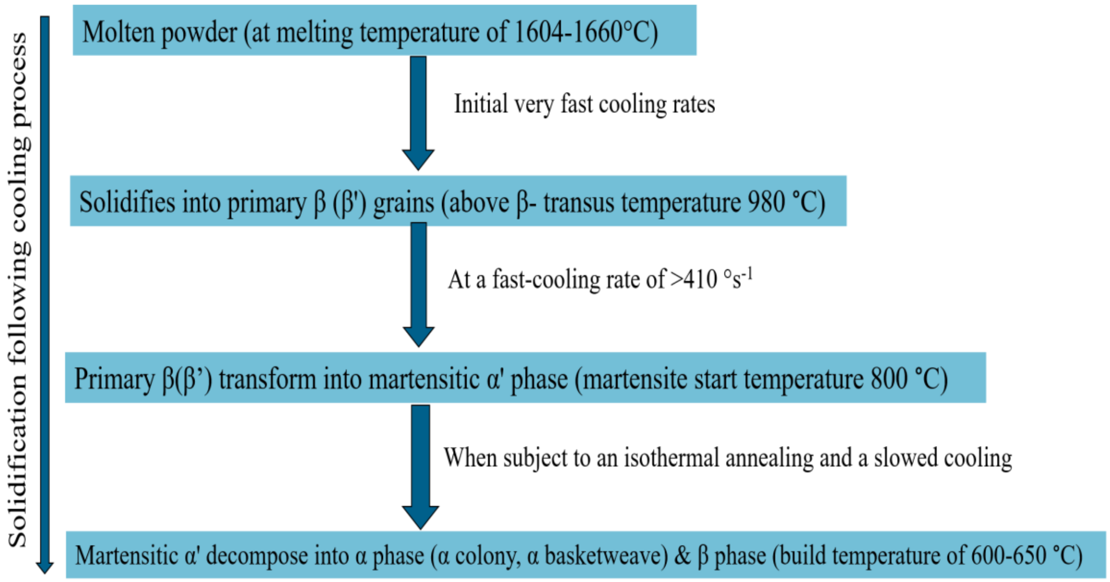

Figure 3 Illustration of the microstructure formation in Ti6Al4V component following electron-beam PBF process.

2.3 Anisotropy in Room Temperature Mechanical Behaviors of PBF AM-Built Parts

However, the PBF AM-built Ti6Al4V parts show significant anisotropic behavior under tensile loading. This anisotropic mechanical behavior might be due to numerous reasons. Various internal defect distributions and variations of microstructure and slip plane directions are rendered as the key components for the anisotropy of PBF parts. Especially the difference in columnar grain growth and slip system activation directions mainly dictate the observed anisotropy behavior of any metal parts. Usually, the columnar grain boundary grows along the build direction, and the slip systems become active parallel to the α platelets [17,45,46]. The change of the orientation and maximum intensity of the α phase from their preferred strong <2 $\bar{1}$ $\bar{1}$ 4> type texture to the other types would contribute to the anisotropic behaviors of EBM parts[40].

In their study, Ladani et al. [45] have studied the room temperature mechanical behaviors of as-built EBM Ti6Al4V parts through various testing and microstructural analysis. They have found significant anisotropic elastic and plastic behaviors and strain rate dependency for the samples built in different orientations. The variation of columnar grain growth and slip system activation directions were found to be the main reasons for this anisotropy, where columnar grain boundary was seen to grow along build direction and slip systems were found to be active parallel to the α platelets. Interestingly, they have also observed that the hardness and microstructure change locally from the base plate to a further location along the build direction. They have anticipated that these variations are due to the change in cooling rates. During the melting and solidification process, most of the heat is conducted towards the build table since the conductivity of the surrounding powder is very poor. As a result, the bottom section of the sample has finer α-plates due to a faster solidification rate as compared to the top section, where the solidification rate is low. In another study, H.K. Rafi et al. [17] demonstrated the comparison between the two most common PBF processes, which are SLM and EBM, depending on the room temperature microstructural and mechanical properties of Ti6Al4V parts produced by these two processes. The most crucial difference is the resulting microstructural variation. The SLM processed parts have an α'martensitic phase while the EBM processed parts have an α phase along with a small amount of β phase. And the variation of these microstructures is due to the different processing conditions and cooling rates. They have also observed that the tensile and fatigue properties of these two processes also vary because of these different microstructures.

The microstructural variation of the as-built and heat-treated EBM-built Ti6Al4V alloys and their effect on the resultant mechanical properties was investigated by Formanoir et al. [42]. With the help of numerical reconstruction of the primary β phase, they have shown that the prior β grain grows along the build direction following a columnar morphology during the solidification phase of the melt pool. They have also observed that the vertically built samples have lower yield strength than the horizontally built sample. The subtransus temperature heat treatment produced a modest microstructural variation with a very low mechanical property shift from the as-built sample. Whereas the supertransus heat treatment resulted in a very different microstructure with a rapid β grain growth and transformation of columnar morphology into an equiaxed one as noticed in the isotropic material.

The microstructure and property variations resulting from the processing build chamber temperature of the EBM Ti6Al4V parts have been analyzed by Al-bermani et al. [43]. This study again confirms that the initial columnar β grain transforms to the diffusional alternate α/β microstructure from the transitional martensitic structure after completion of the build process of the EBM Ti6Al4V component. From the prior β reconstruction following EBSD analysis, they have observed the substructure formation as low-angle grain boundaries in-between the columnar dendrites resulting in a complex deformation mechanism. The build temperature variation was found to have a significant effect on the resulting microstructure and mechanical properties. They have observed that increasing the build temperature above

678°C resulted in a significant decrease in mechanical properties because of the coarsening of the microstructure in the as-printed condition. The effect of build thickness on the consequent microstructure was analyzed by Tan et al. [44]. They have observed the presence of α'martensite along with alternate α/β microstructure in the sample, which is very thin with a thickness of 1 mm. Whereas, inside the thick samples with a thickness of 5- 20 mm, all the martensitic α'decomposes into alternate α/β with both the basket-weave and colony morphologies, due to the slow cooling rates as compared to the thin sample.

2.4 High-Temperature Mechanical Behaviors of Titanium Alloy

Moreover, various high-temperature properties of Titanium alloy, produced by traditional manufacturing processes, have been analyzed by many researchers. For example, J. Kim et al. [23] have studied the high-temperature tensile properties of conventional Ti6Al4V samples using instrumented indentation testing (IIT) and a modified representation method. They have also conducted high-temperature tensile testing along with IIT. They have found that with increasing temperature, the yield strength and tensile strength of Ti6Al4V parts get reduced, and the ductility gets increased due to the activation of atoms and movements of dislocations. In another study, W. S. Lee et al. [22], have examined the mechanical behaviors of hot-rolled Ti6Al4V alloy at various strain rates and temperatures using the compressive split-Hopkinson bar technique. They have found significant sensitivity of the flow stress behavior of Ti6Al4V parts to both the strain rate and temperature. They have also observed that work hardening rates also decrease with the increasing temperature and strain rate.

Y. Y. Zong et al.[47], have investigated the hydrogenated conventional Ti6Al4V alloy, with equiaxed α phase and transformed β phase, at high temperature using isothermal hot compression test. They observed that the flow stress decreased by 11.2% with the addition of 0.3 wt% hydrogen in the titanium alloy when the plasticity increased by 20% due to low dislocation density, decreased stacking fault energy, twinning, dislocation mobility, and dynamic recrystallization, which were induced by hydrogen. Besides, with the increasing temperature, the flow stress decreases because of the increase in dynamic recrystallization. And J. H. Zhu et al. [48] have analyzed the high-temperature mechanical properties of Ti6Al4V matrix alloy and TiC_P/Ti6Al4V composite material produced using cold and hot isostatic pressing (CHIP) up to 538°C. They have found that the yield strength, tensile strength, and creep resistance of the composite material TiC_P/Ti6Al4V are greater than the matrix alloy Ti6Al4V when the ductility is lower than the former one. They have also noticed that the ductility is very sensitive to strain rate due to the stress relaxation mechanism. The mechanical properties of hot rolled Cu-1.5 wt.% Ti alloy in the solution treated and peak aged conditions at high temperatures up to 550°C have been analyzed by S. Nagarjuna and M. Srinivas [49]. They have found that the yield strength and tensile strength of solution-treated alloy increase with increasing temperature up to 450°C because of the metastable and ordered Cu4Ti (β^1) phase precipitation, created during the elevated temperature age hardening, and then decreases with further increase of temperature due to the coarsening of β^1 precipitation. On the contrary, in the peak-aged condition, the yield strength and tensile strength remain almost constant with an increase of temperature up to 350°C and decrease beyond this temperature. This decrease at high temperature again can be attributed to coarsening of precipitates and easier dislocation movements due to thermally activated slip glide.

The high-temperature tensile properties of as-rolled Ti-40Al-15Nb alloy were studied by C. T. Yang et al. [50] up to 1150°C at a strain rate of 10^{-3} s^{-1}. They have found that the ultimate tensile strength of this alloy shows a positive temperature dependence up to 800°C, then decreases with temperature. The increment of the UTS was described as the result of the introduction of dislocation dipoles and numerous jogs and debris defects due to the increase of interactions of 1/2<110> screw dislocations with strain. Above 800°C, the decrease in tensile strength with temperature might be due to thermal activation and weak 1/2<110> screw dislocations. The laser melting deposited (LMD) TiC/TA15 composite was examined by D. Liu et al. [51] at various high temperatures with the crosshead moving rate of 0.2 mm/min. They have observed that the ultimate tensile strength decreases from 625 MPa to 342 MPa, while the percent elongation increase from 7% to 18% with the increase of temperature from 600°C to 700°C. The tensile properties of cold-rolled Ti-6Al-4V at a strain rate of 6.6×10^{-4} s^{-1} were studied by S.H. Wang et al. [52] up to 450°C. They have observed that the tensile strength increases and the ductility decrease with increasing temperature. Interestingly, they have noticed that at around 300°C temperature, there is a rapid drop of ductility, which might be because of the oxide film and temperature dependence of the activation of slip systems.

The evolution of microstructure and underlying mechanisms of conventional Ti6Al4V alloy undergoing different thermomechanical processing has been reported by various researchers [53–59]. Various mechanisms have been found to be activated during high-temperature deformation resulting in softening behaviors. In the temperature range of 500°C-850°C, which falls in the α phase field, the potential softening mechanisms are grain coarsening, elongation, rotation, platelet local shear deformation, and dislocation glide and climb [59,60]. On the contrary, during hot pressing at high temperature, adiabatic heating and α→β phase transformation (between temperatures 850°C to 950°C) and dynamic recovery and dynamic recrystallization (DRX) (between temperatures 1000°C to 1050°C) have been identified as possible flow softening mechanisms by Ding et al. [53]. The observed microstructural evolution was found to be manipulated by the initial microstructure, hot working temperature, strain rate, and successive cooling rate. The different cooling rates also determine the morphology of the resultant α phase as Widmanstätten or acicular, equiaxed, plate-like, and basket weave. The adiabatic heating might raise the actual temperature of the sample and thus increase the softer β phase, which is responsible for softening behavior of the sample. He et al. [54] also reported the dynamic recrystallization and globularization of α layers to be activated during hot deformation at a temperature higher than β-transus, resulting in microstructural evolution and softening of Ti6Al4V alloy. Dynamic α-grain coarsening was also observed to be activated during slow hot deformation and subsequent quenching at 500°C and 600 °C.

The dominant softening mechanisms of Ti6Al4V alloy in steady-state hot forming deformation have been discussed and modeled by Bai et al. [56]. They have molded the globalization of lamellar alpha phase, dislocation density, temperature rise due to plastic deformation, texture change, and phase transformation as potentials flow softening mechanisms. During the phase transformation starting at around 600°C, the volume fraction of the hcp α phase decrease with the increase of temperature. The complete transformation of the alpha phase to the bcc β phase can be obtained by reaching the beta transus temperature. Thus, the proposition of a softer beta phase has a significant effect on material flow properties. The alpha phase is harder than the beta phase, and the former deforms less than the latter phase causing strain concentrations in the softer beta phase. Furthermore, the globalization of the colony alpha occurs due to the localization of the strain into shear bands within the alpha lamellae during hot deformation [61,62].

The deformation temperature during thermomechanical processing plays a significant role in controlling the evolution of the α and β phases. The initial sample has a mixture of equiaxed α and β grains. The α phase becomes coarser with the increasing processing temperature. Furthermore, the Ti6Al4V alloy having high stacking fault energy stimulates sub-structure formation during deformation. On the contrary, deformation at high temperature reduces the dislocation density due to the thermally activated dislocation motion resulting in softening behavior in the alloy [58].

The flow softening of Ti6Al4V alloy during high-temperature deformation has been described by Park et al. [57] as well. The evolution of the lamellar alpha to globular alpha, the colony rotation, and alpha particle coarsening were proposed and investigated as potential softening mechanisms. They have observed that alpha coarsening is the dominant mechanism over dynamic spheroidization at the thermomechanical processing temperature range of 815-950°C and strain rates of 0.1 and 1.0 s^{-1}. Souza et al. [58] have investigated the evolution of the beta phase during the hot deformation of Ti6Al4V alloy. During the hot working process, vanadium diffusion was observed to take place, increasing the volume fraction of the beta phase. Therefore, strain-induced phase transformation was noticed due to the adiabatic heating in α+β working. The deformation temperature during thermomechanical processing plays a significant role in controlling the evolution of the α and β phases. The sample deformed at 720 °C has a mixture of equiaxed α and β grains. The volume fraction of the α phase decreases, and they become coarser with the increasing processing temperature. Furthermore, the Ti6Al4V alloy having high stacking fault energy stimulates sub-structure formation during deformation. On the contrary, deformation at higher temperatures reduces the dislocation density due to the thermally activated dislocation motion resulting in softening behavior in the alloy.

2.5 Inherent Manufacturing Defects in Metal AM-built Parts

Furthermore, various PBF AM process-built Ti6Al4V parts are known to have various internal defects, such as lack of fusion (LOF) porosity, keyhole porosity, and entrapped gas porosity [30,63–66]. LOF porosity occurs due to insufficient energy density, whereas keyhole porosity builds up along the scanning path because of excessive energy density. Non-uniform supply of the powder layer, deviation of the process parameters from the desired ones caused by the change of the power source and scanning system, etc., are some of the reasons responsible for both of these porosities [67]. Whereas the gas porosity could originate from the trapped argon in powder feedstock during the atomization process and from the water vapor on the powder surface as hydrogen pores [64]. All these porosities are detrimental to the mechanical performance of the PBF parts. X-ray tomography has been an excellent tool in non-destructively analyzing these inherent defects of various metals AM parts.

2.6 Fatigue Performance of Metal AM-built Titanium Parts

On the other hand, past research has shown a correlation between fatigue failure and inherent material defects, microstructure, surface roughness, and residual stress [68–74]. Surface and sub-surface defects are found to be the most likely locations for fatigue crack initiations sites as compared to the other types of defects. Different post-processing treatments have shown the potential to enhance the fatigue resistance of these AM parts. For example, machining, shot peening, electropolishing, etc., can be used to reduce surface roughness, whereas various internal defects like pores and unmelted zones can be minimized by hot isostatic pressing (HIP). Likewise, heat treatment can be used to lessen various microstructural defects and residual stresses. But, these post-processing techniques are very costly, time-consuming, and sometimes very difficult for complex geometries [75]. Besides, the most significant benefits of adopting additive manufacturing over traditional subtractive methods are being able to produce near-net-shape parts, cost and waste minimization, and producing complex geometries [76].

Therefore, the as-built specimens produced by one of the PBF additive manufacturing processes, which is electron beam melting (EBM), have been analyzed here. However, one of the major objectives of the authors is being able to minimize various inherent defects, which are very common to the PBF parts, through various process parameters optimization instead of expensive post-processing, it is equally important to understand the effects of various defects on the performance of parts. Hence, various surface and internal defects of EBM-built parts have been investigated here to determine their potential effects on their fatigue performance of them.

Numerous researchers have studied the inherent defects, and fatigue performance of PBF processed parts. For example, Chastand et al. [77] have studied the fatigue properties of Ti-6Al-4V parts produced by EBM and SLM using high cycle fatigue tests at a stress ratio ($R = \sigma_{min}/\sigma_{max}$) of -1 and with a constant stress amplitude. They have found that a HIP treatment, in addition to the machining and polishing of the as-built specimens, has significantly improved the fatigue strength for both EBM and SLM processes. They have also observed that fatigue properties vary with the build directions of the specimens in these two processes. Further analysis showed that post-processing treatment could improve fatigue properties to the level of classical casting and wrought processes. In another study, it has been demonstrated that the high cycle fatigue properties of EBM and direct metal laser sintering (DMLS) produced Ti6Al4V parts are controlled by the inherent surface roughness [78]. Moreover, it has been tried to estimate the fatigue performance based on a simple estimation model approach of linear fracture mechanics, where an equivalent initial flaw size (EIFS) was back extrapolated from the experimental stress-life data and correlated to the surface roughness parameter R_t which is the total height of the roughness profile. From the fatigue crack growth experiments, it was found that the crack growth rate of EBM is lower than DMLS near the threshold stress intensity (ΔK_{TH}) region.

The effects of the surface roughness and microstructure on the high cycle fatigue (HCF) life of Ti-6Al-4V parts produced by SLM and EBM have been evaluated through load control fatigue testing at stress ratio R= - 1 and with frequency f = 120 Hz by Vayssette et al. [79]. They have found that for both SLM and EBMAM processes, the as-built sample has lower fatigue strength than the machined HIPed sample. In their study, Cao et al. [80]

have also investigated the fatigue performances of Ti-6Al-4V produced with different additive manufacturing processes. They have found that the fatigue properties of AM-built Ti-6Al-4V parts are controlled preferentially by the surface roughness, porosity, and microstructure. They have also noticed that wire-feed and SLM processed Ti-6Al-4V have better fatigue performance than EBM Ti-6Al-4V because of reduced as-built surface roughness and less porosity in the former cases. The higher surface roughness in EBM-built Ti-6Al-4V could be due to some of the processing parameters, such as coarser powder, thicker deposition layer, faster scan speed, and larger beam size, that are used in available Arcam machines as compared to some other AM processes. Finally, they have concluded that since all as-fabricated AM Ti-6Al-4V has a lower crack growth threshold (∇K_{th}) due to finer grain than the wrought materials, they are not appropriate for fatigue-critical applications without substantial post-processing treatment like HIP, surface machining, and polishing.

The residual stress in the EBM-produced Ti-6Al-4V parts is very low since the build chamber is maintained at a high temperature of around 700°C throughout the build process [17]. However, it was found that the fatigue life of the as-built EBM Ti-6Al-4V sample with a rough surface didn’t improve much with hot isostatic pressure (HIP) operation [78],[81]. As a result, it can be noted that the porosity doesn’t have as severe an effect as the surface finish has on the fatigue properties of EBM samples [82].

2.7 Gaps in the Literature

Finally, though the anisotropic mechanical behavior and underlying microstructural variation inherent to PBF-AM-built Ti6Al4V parts have been analyzed by various researchers, most of these studies are either inconclusive or have conflicting observations. Moreover, a comprehensive analysis, including various microstructural features such as intrinsic defects, grain sizes, crystallographic texture, preferred grain orientation, and their effects on the mechanical anisotropic behaviors, was felt highly necessary by the authors to provide further insight and precaution for the users of EBM Ti6Al4V in various critical applications.

Furthermore, the microstructural evolution and related mechanical behaviors of traditionally produced Ti6Al4V alloy during various thermomechanical processing and hot deformation have been examined by various researchers identifying various mechanisms responsible for these behaviors. But, most of these studies are again either inconclusive or have conflicting findings. Moreover, there are very limited works reported in the literature, according to the author's knowledge, focusing on and analyzing high-temperature mechanical behavior and corresponding microstructural evolution of AM-built Ti6Al4V alloy.

On the contrary, according to the author’s knowledge, very few works have been conducted focusing on the elevated temperature elastic and plastic behaviors of PBF metal parts. Limited available high-temperature data of conventional Ti6Al4V alloy are presented in **Table 2** to indicate how they vary with testing temperature and with strain rates. Aliprandi et al. [83] have investigated the tensile and creep behavior of EB-PBF-produced Ti6Al4V alloy after hot isostatic pressing and surface machining. They have found that the applied post-processing has improved the tensile and creep behavior considerably by relieving stresses and reducing detrimental defects like porosity and surface roughness. Besides, they have analyzed the high-temperature mechanical properties up to 800°C and found that the ultimate tensile strength and yield strength decrease, while the ductility increases with the increasing temperature. They have examined the sample printed only in the XZY direction. But available literature indicates that printing orientation could have significant effects on high-temperature mechanical properties. The microstructural evolution and related mechanical behaviors of traditionally produced Ti6Al4V alloy during various thermomechanical processing and hot deformation have been examined in depth, identifying various mechanisms responsible for these behaviors. But there has been hardly any work reported in the literature, according to the author's knowledge, analyzing high-temperature mechanical behavior and corresponding microstructural evolution of AM-built Ti6Al4V alloy.

Table 2 Mechanical Behaviors of Conventional Ti6Al4V Parts Available at Literature. (RT means room temperature).

Sample Type	Temperature (°C)	Modulus of Elasticity (GPa)	Yield Strength (MPa)	UTS (MPa)	Elongation (%)	Strain rate (s^{-1})	Reference

Ti6Al4V (Wrought material)	RT	105-107	860-962	930-1008	>10	8×10^{-4}	[25,84,85]
Ti6Al4V (Conventional)	500	NA	436	467	31.2	8.3×10^{-3}	J. Kim, 2016
	RT		968	1015	12		
Ti6Al4V (CHIP)	538	NA	356	430	13.4	6.7×10^{-5}	J.H. ZHU, 1999
			382	463	15.5	6.7×10^{-4}	
Ti6Al4V (Hot-rolled)	700	NA	580	NA	NA	8×10^{2}	W.S. Lee, 1998
	RT		998				
Ti6Al4V (cold rolled)	450	NA	505	592	28	6.6×10^{-4}	S.H. Wang, 2002
	RT		903	982	19		

Moreover, the fatigue strength of the as-built EBM parts could be 65-75% lower than the classically produced wrought parts [17]. So, it is apparent that the most critical issue with respect to the fatigue critical applications of EBM Ti6Al4V parts is the surface roughness. These surface irregularities could be formed due to various reasons such as balling, stair-steeping, and partially melted powder particles attached to the surface [86,87]. Again, the surface roughness of the EBM sample also varies with built orientations with respect to the built table [8],[77],[81]. For this reason, the fatigue strength of EBM Ti-4Al-4V parts might also vary with their built orientation of them.

From the above literature analysis, it is obvious that various defects, especially the surface or sub-surface ones, inherent to the EBM processed parts are very crucial to their fatigue-critical applications. Nevertheless, the quantitative correlation between the fatigue strength and the inherent defects has not been analyzed well enough, according to the author's knowledge, though it is very crucial for various fatigue-critical applications. Furthermore, there is a lack of understanding of how these defects contribute to crack initiation and propagation in a part that has inherently anisotropic behavior.

CHAPTER 3

OBJECTIVE AND RESEARCH PLAN

From the above discussion, it can be seen that the mechanical behavior of various Titanium alloys produced by various conventional processes could be highly temperature-sensitive. Furthermore, it can be intuitively hypothesized that Ti6Al4V parts, produced by various PBF processes, would be pretty temperature sensitive as well. However, investigating the high-temperature characteristics of the PBF processed part is very crucial because of its numerous high-temperature application needs. Hence, this study investigated the mechanical behaviors of EBM-built Ti6Al4V parts at various high temperatures up to 600°C temperatures. In addition to that, the anisotropy of the mechanical behavior was also examined using EB-PBF Ti6Al4V samples built in three different orientations at those specified temperatures. The fracture surfaces of all the tested samples were investigated using an optical microscope and a field emission secondary electron microscope (FESEM) for a deeper understanding of the possible failure mechanism.

Electron backscattered diffraction (EBSD) techniques have been used for the microstructural analysis of samples both before tensile testing and after tensile testing. The effect of the as-built microstructural aspect and inherent defects on the intrinsic anisotropic behavior of EB-PBF AM-built Ti6Al4V alloy have been investigated as well. Again, because of having various crucial high-temperature applications in aerospace and other industries [88,89], this study also focuses on the high-temperature mechanical behaviors of Ti6Al4V parts built by EB-PBF at different temperatures up to 600°C. The microstructural evolution and subsequent changes of texture, phase, preferred grain orientation, and sizes of the grains after tensile testing of the samples at different temperatures have been analyzed further to understand potential softening mechanisms and their effect on the resultant mechanical properties. EBSD techniques have been used for the microstructural analysis of the sample after careful preparation of them using standard polishing processes and to observe their respective microstructural evolution due to the applied thermomechanical loading.

Besides, the surface profiles from different faces parallel to the loading direction of EBM-produced Ti-6Al-4V parts built in different orientations have been measured using a stylus profiler. Various surface roughness parameters have been obtained from the surface profile measurements to analyze the anisotropy in surface roughness. Finally, from these measured surface profile, the projected areas of surface roughness defects on a plane perpendicular to the maximum principal stress has been calculated. Although the as-built surface defects are more crucial to fatigue performance, the internal defects with considerable size could be detrimental too. Therefore, X-ray computed tomography (CT) analysis was conducted to determine the inherent internal porosity defects of the as-built EBM Ti6Al4V parts. The obtained defect areas are then used along with the hardness of the parts to predict the fatigue strength of these parts mathematically, utilizing Murakami's square root area model [90]. The fatigue strength at 1000 cycles is estimated using Basquin's model. Eventually, the stress vs. number of the cycle (S-N) curves obtained through these two models were compared with the experimental data available in the literature. The fatigue life prediction model shows pretty good agreement with the experimental data. Further analysis of the effects of various defects on fatigue crack initiation and propagation can be conducted using finite element analysis in conjunction with continuum damage mechanics models in the future study.

CHAPTER 4

WORK ACCOMPLISHED

4.1 Materials and Methods

The standard sub-sized and dog-bone-shaped specimens for tensile testing were CAD modeled and manufactured, according to the ASTM E8/E8M [91] standard, using the Arcam® A2 EBM system [92]. All the specimens were printed in a layer-by-layer fashion at three different orientations, as shown in **Figure 4**. The used EBM system produces high-energy electrons with the help of an electron gun containing tungsten filament when 60 kV is applied to the filament. The generated electron beams, having a power density of up to 100 kW/cm^2, were focused using electromagnetic focusing lenses, whereas the lateral motion of the focused beam and scanning were controlled using the deflection coils. The cross-raster scanning strategy was utilized for melting the powder layers. The hatching distance was around 200 µm. The average powder particle size used for fabricating the specimens was 70 µm. The powder layer thickness was 70 µm which was reduced to 69 µm after the melting process. The incident beam size was 500 µm. The scanning speed varied between 0.5 m/s to 15 m/s for different steps. The pre-heating of the powder bead was done at a higher speed (15 m/s), while the melting step was done at a lower scanning speed (0.5 m/s). The beam power was varied between 100 W - 400 W. To ensure the quality of the electron beam, the upper chamber was maintained at 7.5×10^{-7} Torr (1 Torr = 0.00131578947 atm). The build chamber was kept at 7.5×10^{-5} Torr to prevent the oxidation of titanium. The powder bed was preheated and maintained at around 700°C temperature throughout the whole building process to minimize the thermal stress buildup on the specimens due to the temperature gradient [93],[94]. After the completion of the printing process, the side-built samples had overhang support structures which were removed through machining to make the samples ready for tensile testing. Further details of the EBM process parameters can be found elsewhere [95].

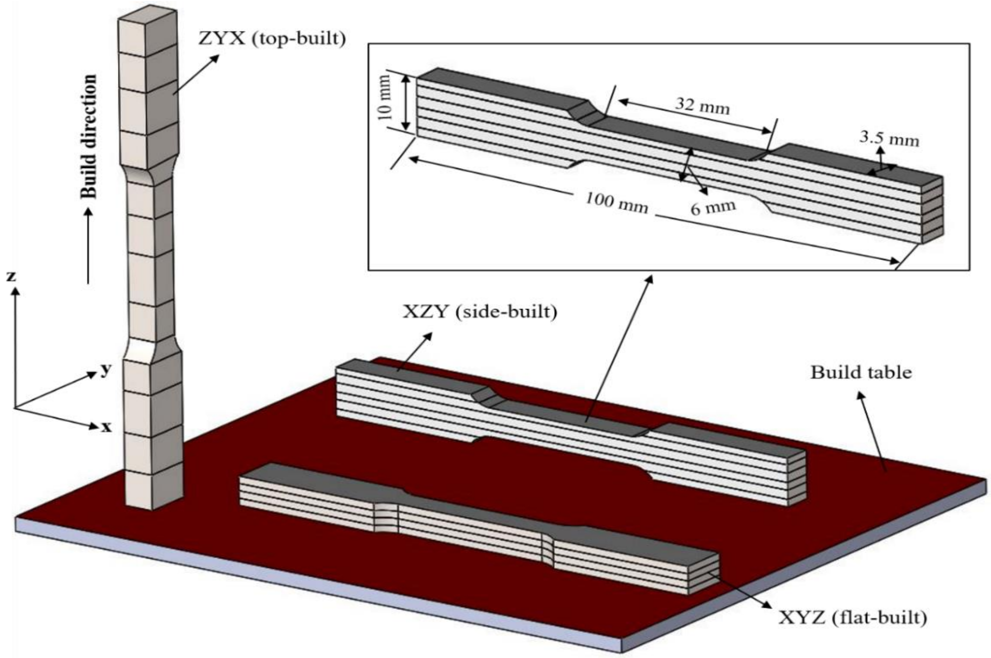

Figure 4 CAD design with dimensions (inserted image) of the sub-sized Ti6Al4V tensile specimens for the EBM process with samples organized in three orientations with respect to the build table.

Samples printed in three different orientations are named flat-built, side-built, and top-built samples (Figure 1), where deposition layers are stacked along with the thickness, width, and longitudinal directions, respectively. The Z-axis implies the build direction and is always normal to the deposited layers. Tensile tests were conducted on the three types of samples to determine their respective mechanical properties. Test coupons for microstructural structural analysis were collected from all three samples along the XZ plane, parallel to the build direction, to make a direct comparison among them. Furthermore, another batch of test coupon was collected from the XY plane, perpendicular to the build direction, of the flat-built sample to observe the microstructural variations on two different planes of the same sample.

4.2 Elevated Temperature Anisotropic Mechanical Behavior of EB-PBF AM Produced Ti6Al4V Parts

4.2.1 Experimental Procedures

4.2.1.1 High-Temperature Tensile Testing

High-temperature tensile testing was conducted on all the specimens using an MTS Criterion® Electromechanical Universal Test System modeled as MTS C45 in conjunction with a Thermcraft® Inc. environmental chamber. The experimental setup is shown in **Figure 5**. The load cell used MTS LPS.504, which had a force capacity of 50 kN (11 kip). The temperature inside the chamber was controlled using a Eurotherm® 2404 temperature controller which had a temperature limit of up to 620°C. Since the strain data computed from the extensometer reading provided more accurate values than the measurements using the crosshead reading, all the testing was carried out at strain control mode until the fracture occurred with the strain rate of 0.05 mm/mm/min. The extension data during the test was collected using an Epsilon® axial extensometer modeled as 7642-010M-075M with a gauge length of 10 mm. The mechanical properties that were analyzed in this study at various high temperatures are elastic modulus (E), 0.2% yield strength (Y), the ultimate tensile strength (UTS), percent elongation, strength coefficient (K), and strain hardening exponent (n). Three specimens from each orientation were tested at three different temperatures, which are 600 °C, 400 °C, and 200 °C. Then, the average values of these properties at each orientation and each temperature were calculated. To avoid compressive forces created during the temperature ramp-ups, the crosshead location was continuously adjusted. Moreover, before starting any experiment, all the specimens were kept at the desired high temperature for around 30 minutes to make the thermal load stable enough. The elastic modulus and 0.2% yield strength were computed from the regression analysis of the stress-strain data on the elastic region.

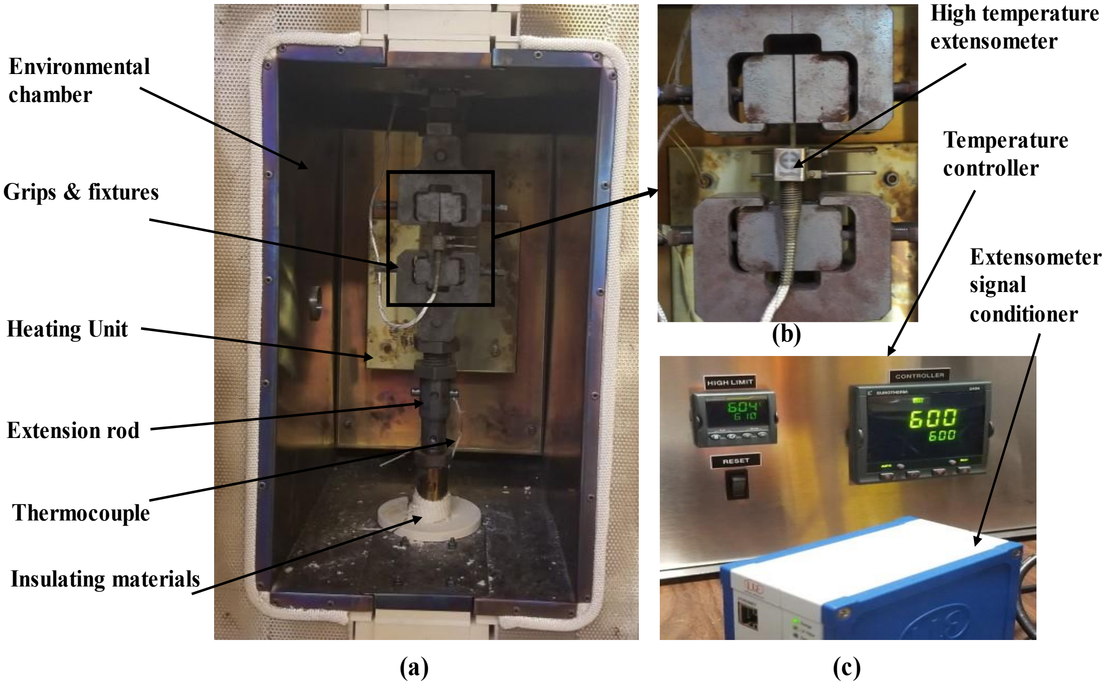

Figure 5 The experimental setup of the MTS high temperature electromechanical universal test system, (a) specimen setup inside the insulated high-temperature chamber with fixtures and grips, (b) high-temperature axial extensometer attached with the specimen, and (c) temperature controller (maximum limit of 620°C) with extensometer signal controller.

4.2.1.2 Design of High-Temperature Grips and Fixtures

The grips and fixtures of the tensile tester were designed in SolidWorks considering various design criteria of the high-temperature applications. One of the design considerations is overloading of the grips, which can damage the load cell, and the machine frame should be avoided. Specimen slippage due to low clamping forces was taken care of by using serrated jaws. Breaking of specimens at the faces of grips should be avoided. The SolidWorks design and mechanical drawings of the U-shape vise grips and fixtures assembly are presented in **Figure 6** and **Figure 7**, respectively. H13 tool steel was selected as the material for the grips and fixtures, as it has excellent thermo-mechanical properties in high-temperature environments. H13 tool steel is a handy chromium-molybdenum hot work steel used in many hot work and cold work tooling applications because of its superior resistance to thermal fatigue cracking [96]. The chromium content of H-13 resists softening when at a high temperature [97]. It also has high toughness, good stability in heat treatment, better hardenability, and better wear resistance. It has a thermal expansion coefficient of 13.5 ×10E-6 (mm/mm/°C) at (21-538)°C and a modulus of elasticity of 158.6 GPa at 538°C temperature [98]. The designed grips and fixtures were cut and shaped using the Wire electrical discharge machining (EDM) process. Then it was polished for surface smoothness. Finally, the heat treatment steps that were conducted for hardening of the machined parts in the following order: Preheating → Austenitizing → Quenching → Tempering → Annealing.

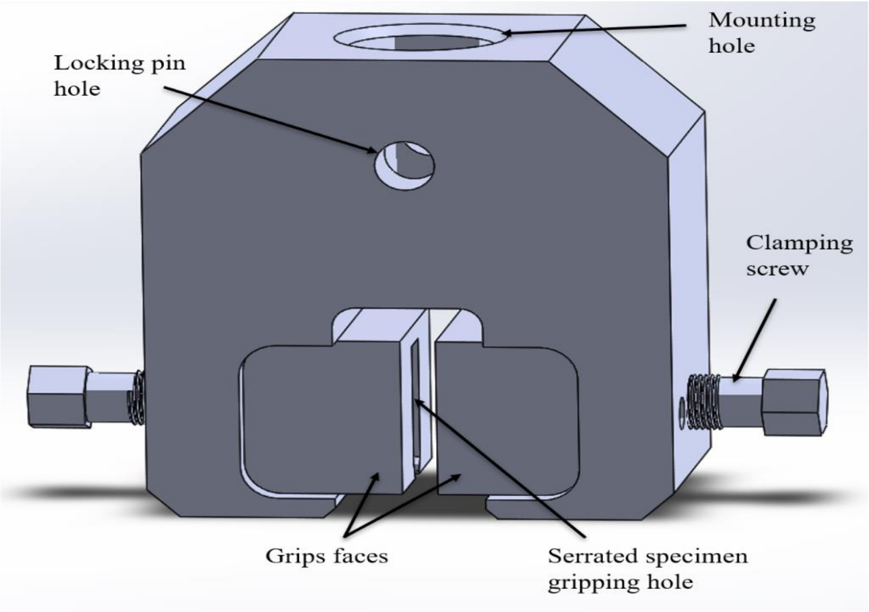

Figure 6 SolidWorks design of a U-shape vise grips and fixtures assembly with various components.

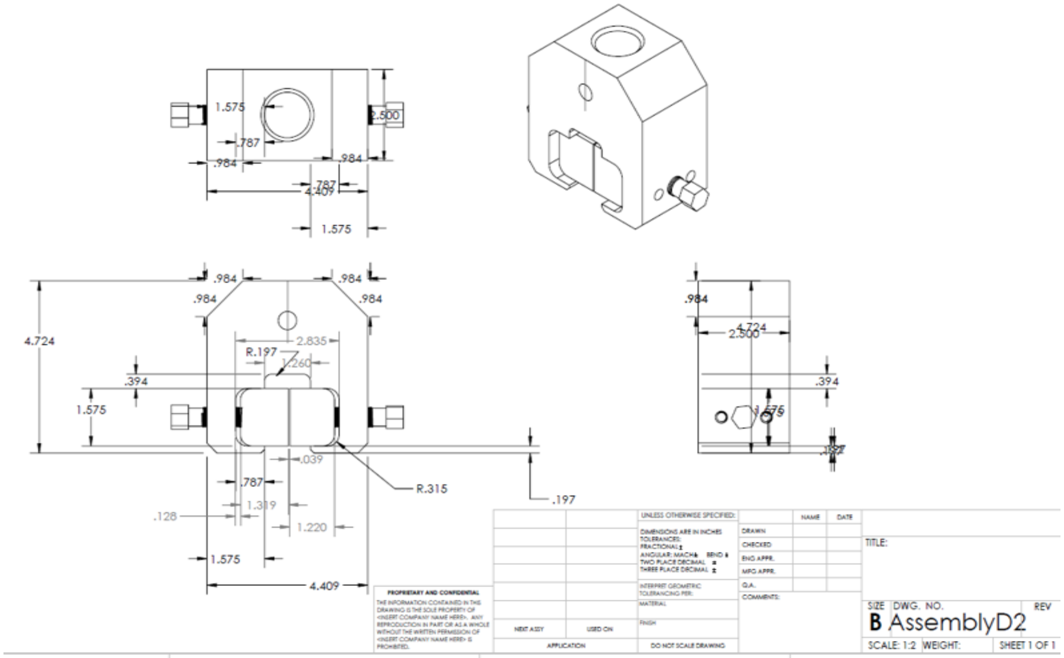

Figure 7 Mechanical drawings of different components of the grips and fixtures assembly.

4.2.1.3 Fracture Surface Microscopy

The fractured surfaces of the tensile-tested samples were analyzed using two different microscopes to determine the fracture pattern and the possible root causes and activation mechanisms of failure under different applied temperatures and loads. A digital stereo zoom microscope modeled as AmScope SM-3TZ-54S-5M was used to analyze the mode and type of the fractures. This microscope has an objective zoom power of 0.7x-4.5x and uses a 44-bulb LED ring light as a light source. Similar default camera specifications, with an objective zoom power of 4x, were used for fracture surface observation of all three samples. Since the broken samples were observed immediately after the test, no further sample preparation step was necessary for this case. Again, for inherent sample defects and failure activation mechanism analysis, a scanning electron microscope named Hitachi S-4700 FESEM was used. This instrument has a magnification capability of up to 500kX with a resolution down to 2nm and a beam accelerating voltage range of 0.5-30kV. In this analysis, 15kV acceleration voltage was used. The sample was prepared by cutting them into 5 mm lengths from the fractured sample using a Leco metallurgy abrasive saw in conjunction with a cooling liquid. The small pieces of specimens were then rinsed into isopropyl alcohol (IPA) liquid to remove all the foreign particles that could stick to them during the cutting process. The results of this analysis have been described in section 4.2.3.

4.2.2 Results and Discussion

4.2.2.1 Anisotropic Behavior

The EBM Ti-6Al-4V parts show substantial mechanical anisotropic behavior at room temperature, as examined by L. Ladani et al. [29]. In their analysis, they have found that flat-built samples have greater yield strength, tensile strength, and elastic modulus properties than the top-built and side-built samples, while top-built samples have the lowest values of these properties. On the contrary, the elasticity is superior on the top-built samples than the samples of the other two build orientations. At room temperature, these samples also showed strain rate sensitivity.

In the current study, the EBM Ti6Al4V parts from three different build orientations have been tested at three different temperatures of 600°C, 400°C, and 200°C to determine the anisotropy at these temperatures. The Ti6Al4V alloy is extremely sensitive to strain rate at high temperatures [99]. So, a constant strain rate of 0.05 mm/mm/min at strain control mode was used throughout the experimentations. A few dummy test specimens were examined at 600°C and at a strain rate of 0.005 mm/mm/min to verify the strain rate sensitivity. It showed significant creep behavior at that low strain rate, and the sample didn't break even at more than 50% elongation. As a result, the above-mentioned higher strain rate was used to avoid creep at high temperatures.

All the representative stress-strain curves obtained from the tensile testing of EBM Ti6Al4V parts with three build orientations and tested at three different high temperatures are presented in **Figure 8**. Here **Figure 8**a, **Figure 8**b, and **Figure 8**c show the curves acquired from the experiments at 600°C, 400°C, and 200°C temperatures, respectively.

From all the stress-strain curves at these three temperatures, it can be noticed that the flat-built sample has superior flow stress to the other two build orientations, while the top build sample has greater ductility. From the stress-strain curves at 200°C and 400°C, it can be noticed that a significant amount of strain hardening occurred in the plastic region. The common mechanism of strain/work hardening is that during the plastic deformation, dislocations move, and new dislocations are created. Besides the movement of the dislocations at different slip planes along with different slip directions, they also interact with each other and with the barriers, thus becoming entangled [100]. This process of strain hardening makes the material harder and stronger. However, at 600°C (**Figure 8**c), interestingly, the work hardening occurs for a very smaller plastic region after the yield strength has been achieved. After that, a substantial amount of softening or hot working behavior could be noticed until the fracture happens. This rapid softening after reaching the peak stress at 600°C can occur due to the recrystallization, grain growth of the materials, and dislocation glides. Because at high temperatures, the atoms and dislocations rearrange and move freely to the low energy region [47],[100]. As the dislocation density decreases and the recrystallization happens, the materials become softer, and the ductility increases as can be seen from the stress vs. strain curves at 600°C.

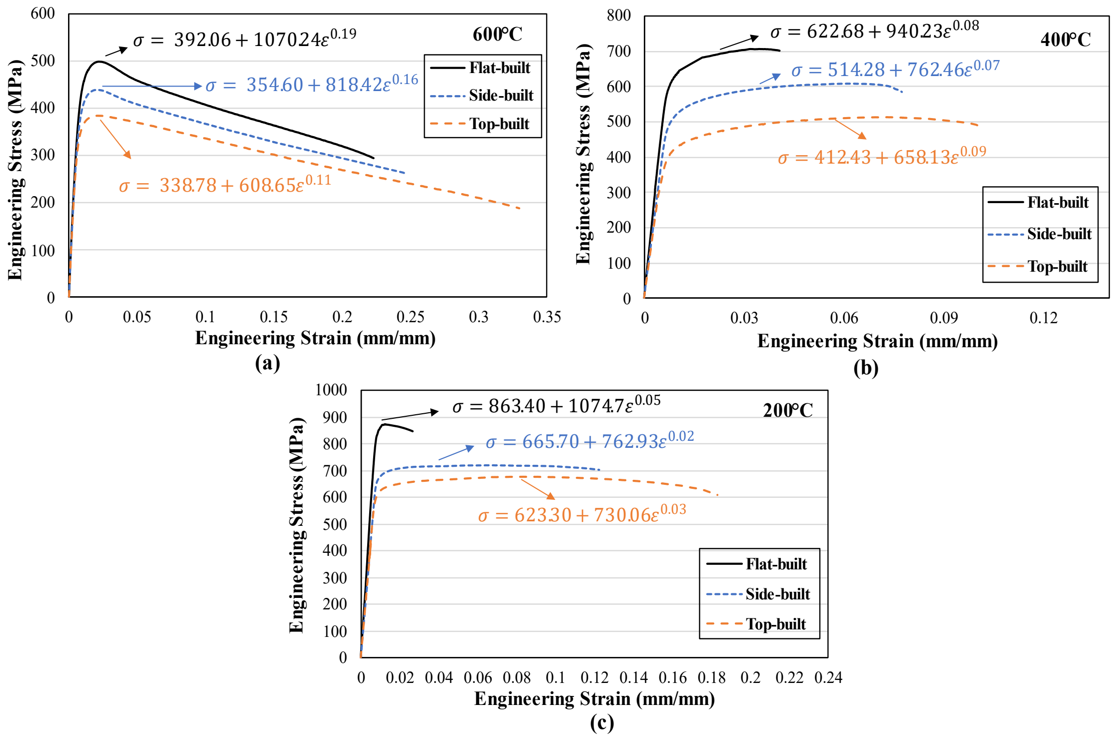

(a) (b) (c)

Figure 8 Engineering stress-strain curves of EBM Ti6Al4V parts with three different orientations tested at (a) 600°C, (b) 400°C, and (c) 200°C temperature

The anisotropic behavior of the EB-PBF Ti6Al4V samples with different orientations can also be observed from the main effect plots of various elastic and plastic properties, as depicted in **Figure 9** & **Figure 10**. At 600 °C, the flat-built sample has a tensile strength of 392 MPa, which is 26.24% higher than the tensile strength of top built sample at the same temperature. Furthermore, the former has a 16.66% higher yield strength and a 14.2 % larger modulus of elasticity than the latter one at this temperature. Whereas the top-built sample has a 47.87% larger percent elongation than the flat-built sample. Similar kinds of anisotropic behaviors can also be observed from the tensile data obtained from the experiments conducted at 400°C and 200°C, as can be seen in **Figure 9** & **Figure 10.** This indicates that there is a significant amount of anisotropy involved in EB-PBF Ti6Al4V samples at high temperatures as well.

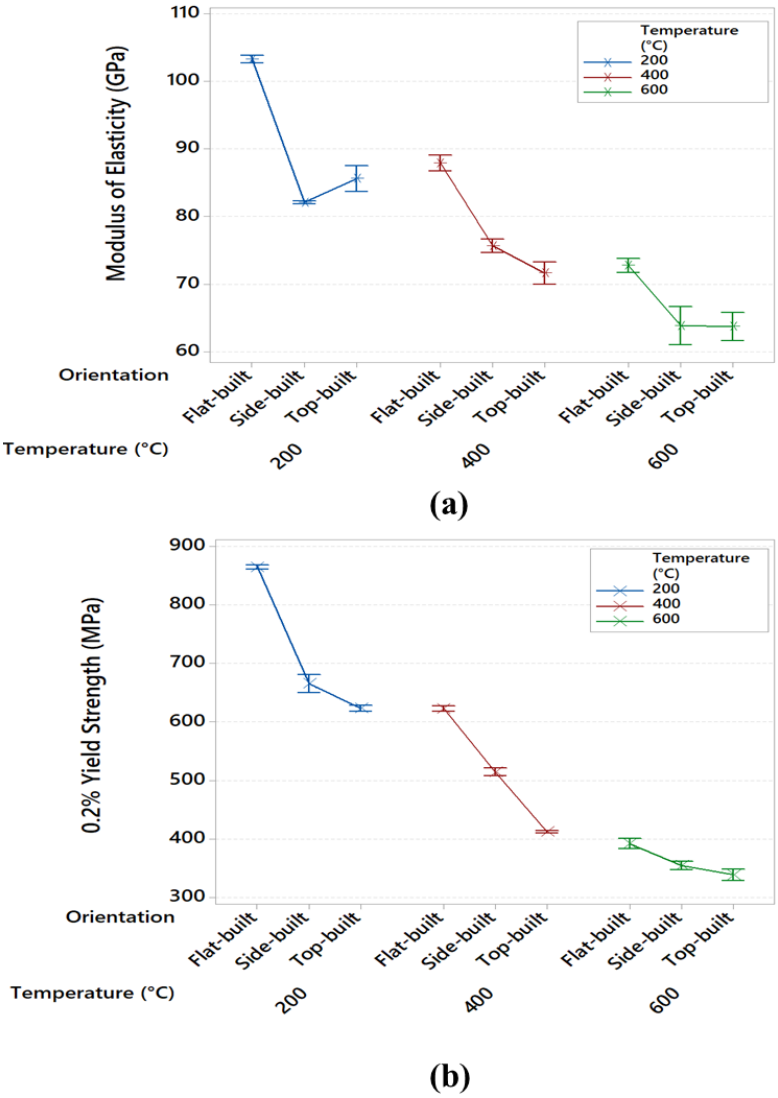

Figure 9 Main effect plots of variation of (a) modulus of elasticity, and (b) yield strength with build orientations of three different EBM Ti6Al4V samples at different high temperatures.

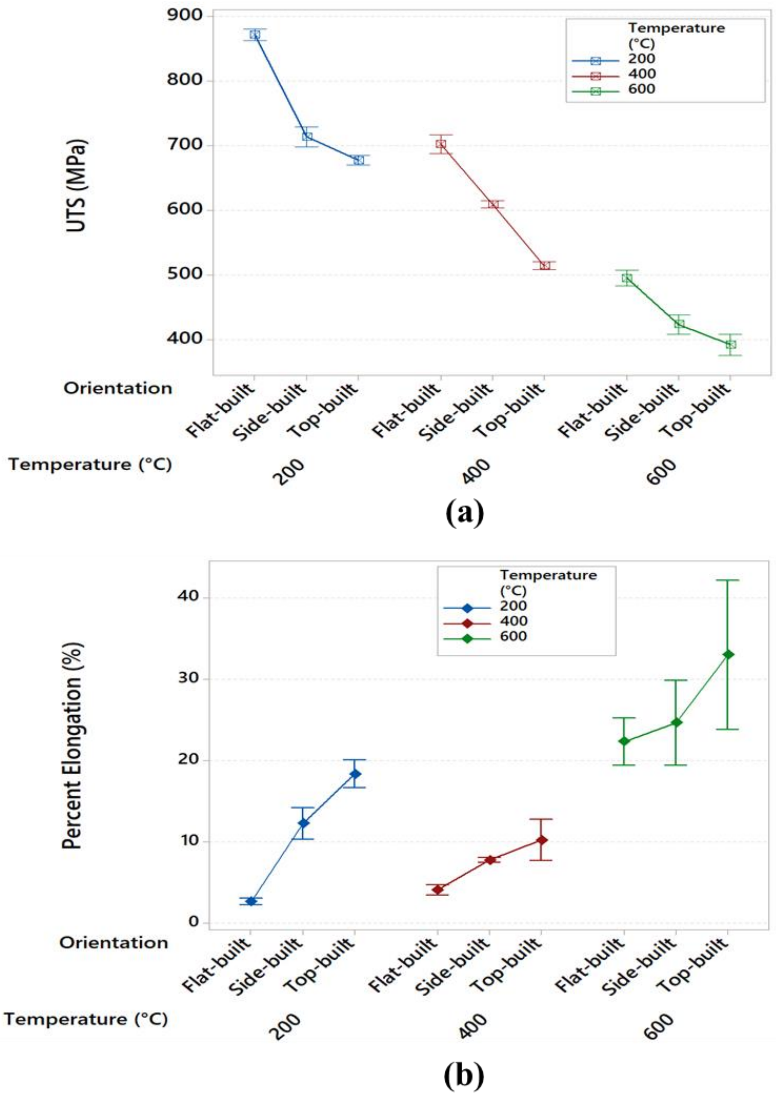

Figure 10 Main effect plots of variation of (a) UTS, and (b) percent elongation with build orientations of three different EBM Ti6Al4V samples at different high temperatures.

This anisotropic behavior could be due to several reasons. The intensity of various defect distribution inside the sample, and variation of microstructure and slip plane directions might be the key factors for anisotropy. Normally, in EB-PBF Ti6Al4V samples prior columnar β grains grow along the build direction [17],[46]. It is hypothesized that these long and thin prior-β grains could be responsible for anisotropic elongation properties. In the top-built sample, the loading direction is parallel to these long grains. As a result, the ductility is high. Whereas in the flat-built sample, the loading direction is perpendicular to it, and thus ductility is low. Conversely, in the top-built sample, there is a larger number of interfaces among the layers, which means that the probability of un-melted powder porosity is also higher. This might be responsible for lower strength in the top-built sample than in the flat-built sample, where the number of layers is low. The various internal and sub-surface defects which are present in EB-PBF Ti6Al4V parts and their variation with build orientation has been analyzed further in section 4.2.3.

Furthermore, the strength coefficient and strain hardening exponent data were extracted from the elastoplastic region of the curves by using Hollomon's power law equation [101] as presented below,

$$\sigma = K\varepsilon^{n} \tag{1}$$

Where K = strength coefficient in MPa, n = strain-hardening exponent, σ is stress, and ε is flow strain. These strain hardening parameters are intrinsic properties and indicative of the flow stress behavior of the materials. As the stress-strain curve varies from flat-built sample to top-built sample, so do the strain hardening parameters, as can be seen on the main effect plots in **Figure 11.** Here the low value of n means that the rate of work hardening is initially high but decreases with the increased strain, as can be noted from the curves at 200°C. The value of n increases with the increase of temperatures where the work hardening is for a longer period, which also means that the material shows higher ductility at higher temperatures. All the elastic and plastic mechanical properties of EB-PBF-built Ti6Al4V parts tested at 600°C, 400°C, and 200°C are presented in

Table 3, **Table 4**, and **Table 5**, respectively.

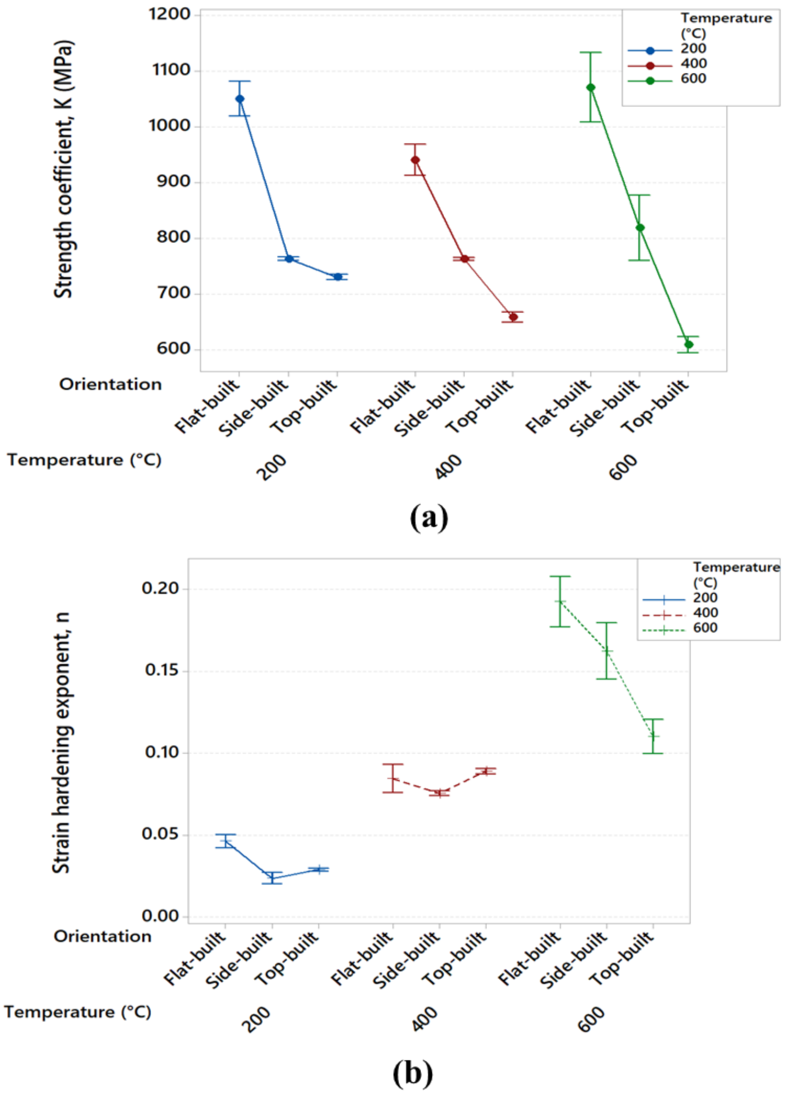

Figure 11 Main effect plot of the variation of (a) strength coefficient (K) and (b) strain hardening exponent (n) with build orientations of three different EBM Ti6Al4V samples at different high temperatures.

Table 3 Mechanical properties of the three different EB-PBF Ti6Al4V samples, tested at 600°C temperature.

Orientation	Specimen no.	E (GPa)	0.2 % Yield strength (MPa)	UTS (MPa)	Elongation (%)	Strength coefficient, K (MPa)	Strain hardening exponent, n
Flat-built	1	72	398	499	25	1083	0.19
	2	71	403	504	25	957	0.16
	3	75	375	483	16	1171	0.21
	Average	73	392	495	22	1070	0.19
	Std. dev	2	15	11	5	107	0.03
Side-built	1	68	358	419	17	702	0.13
	2	65	364	439	22	887	0.17
	3	58	341	412	35	865	0.18
	Average	64	355	424	25	818	0.16

	Std. dev	5	12	14	9	101	0.03
Top-built	1	68	35	410	32	583	0.09
	2	62	325	383	17	634	0.13
	3	62	334	384	49	608	0.11
	Average	64	339	392	33	609	0.11
	Std. dev	4	17	15	16	26	0.02

Table 4 Mechanical properties of the three different EB-PBF Ti6Al4V samples, tested at 400°C temperature.

Sample	Test no.	E	YS	UTS	Elongation	K	n
Flat-built	1	86	612	687	3	978	0.10
	2	87	628	712	5	885	0.07
	3	90	628	707	4	957	0.09
	Average	88	623	702	4	940	0.08
	Std. dev	2	9	13	1	49	0.02
Side-built	1	77	503	604	7	759	0.07
	2	75	526	614	8	768	0.07
	3	74	514	609	8	760	0.07

	Average	76	514	609	8	762	0.07
	Std. dev	2	11	5	0.5	5	0.002
Top-built	1	74	409	508	15	642	0.09
	2	69	411	515	8	660	0.09
	3	72	417	520	7	672	0.09
	Average	72	412	514	10	658	0.09
	Std. dev	3	4	6	4	15	0.003

Table 5 Mechanical properties of the three different EB-PBF Ti6Al4V samples, tested at 200°C temperature.

Sample	Test no.	E	YS	UTS	Elongation	K	n
Flat-built	1	103	863	874	2	1075	0.05
	2	102	871	862	3	1086	0.05
	3	104	860	876	2	987	0.04
	Average	103	865	871	3	1049	0.05
	Std. dev	1	6	8	0.75	54	0.007
Side-built	1	82	686	724	15	767	0.02
	2	82	676	719	13	765	0.02
	3	82	635	697	8	757	0.03
	Average	82	666	713	12	763	0.02
	Std. dev	0.39	27	14	3	5	0.006

Top-built	1	86	633	683	16	735	0.03
	2	82	621	678	22	735	0.03
	3	89	615	669	17	721	0.03
	Average	86	623	677	18	730	0.03
	Std. dev	3	9	7	3	8	0.002

4.2.2.2 Temperature Dependency

The change in all the mechanical properties of EBM Ti6Al4V parts with the temperature for all three orientations is presented in **Figure 12** and **Figure 13**. The ultimate tensile strength (UTS) decreases almost linearly with the increasing temperature for all three orientations (**Figure 12**). On the contrary, the percent elongation changes at a slow rate from 200°C to 400°C temperature. Though for flat-built samples, it increases, for top and side-built samples, it surprisingly decreases slightly at this temperature range. But again, percent elongation increases at a much faster rate for all three orientations, as the temperature is increased from 400°C to 600°C. The room temperature ductility of the EB-PBF built sample was found to be very low as compared to the cast and wrought sample. It could vary significantly between (2.3 to 25)% due to the presence of various inbuilt defects, the change of composition, and porosity distribution disparity [102]. The ductility values at 200 °C should be close to the room temperature values and should be lower than the ductility values of 400°C temperature. But surprisingly, a non-monotonous trend was observed at 200°C temperature. These behaviors can result from various reasons like the variability of samples with respect to the inherent pore size, location in the base plate and microstructure, an error that occurred from the operator or instrument calibration, and so forth.

However, the deformation between 200°C and 400°C temperature is dominated by work hardening; hence elongation rate is slow. At 600°C, the work hardening becomes weaker, and instead, various softening mechanisms like dislocation glide, grain boundary slip, and dynamic recrystallization get activated [103]. Therefore, the improved plastic deformation and reduced flow stress curves can be observed at 600°C for all the Ti6Al4V samples. Moreover, the variance of the percent elongation values among the samples of orientation also increases significantly with increasing temperatures, as can be noticed from the error bars in **Figure 12**. At 600°C temperature, the standard deviation is very high as compared to the other two temperatures. The variation of type and distribution of defects could possibly dictate the rates of softening mechanisms, thus eventually causing a large divergence of plastic deformations among different samples of orientation at high temperatures. Again, both the 0.2% yield strength and modulus of elasticity decrease with the increasing temperature in all three geometrical orientations, as shown in **Figure 13,** due to the same reason as stated above.

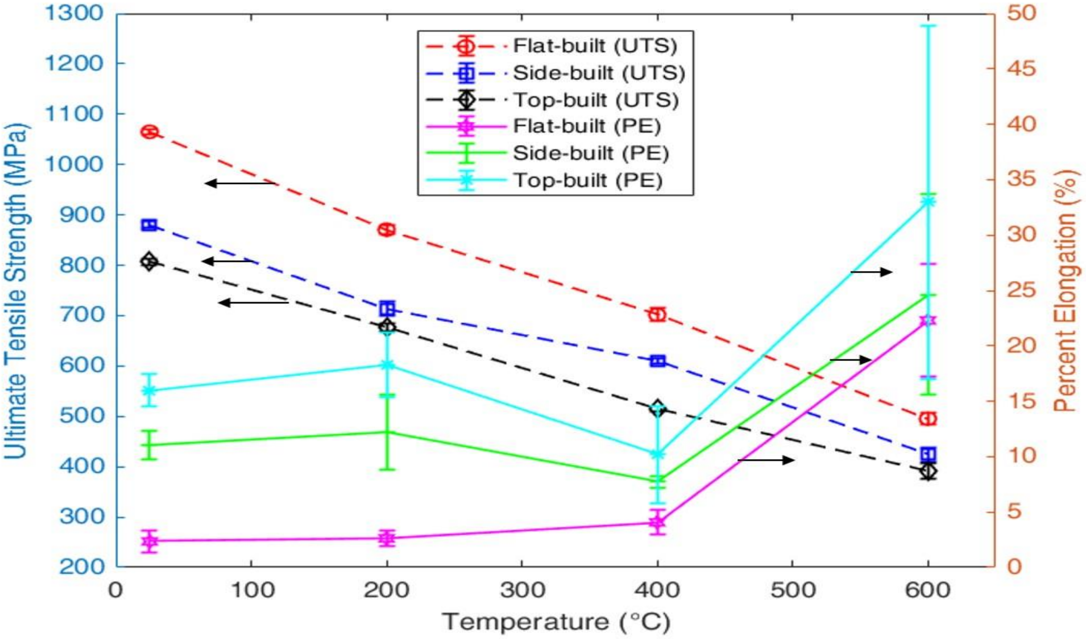

Figure 12 Variation of the ultimate tensile strength (UTS) (left) and percent elongation (%) (right) of EBM Ti6Al4V parts with temperatures for all three build orientations.

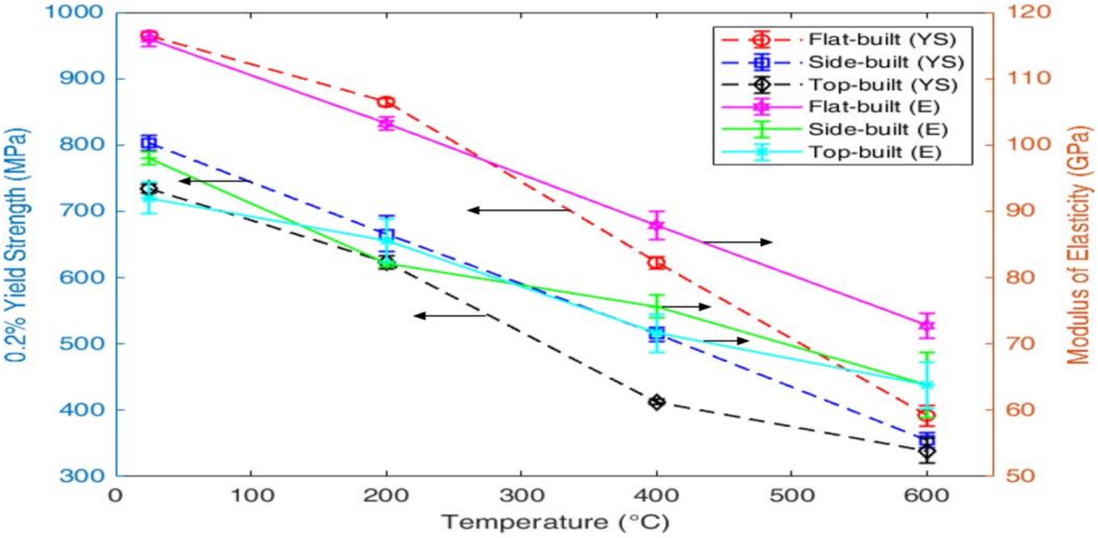

Figure 13 Variation of 0.2% yield strength (YS) (left) and modulus of elasticity (E) (right) of EBM Ti6Al4V parts with temperatures for all three build orientations.

Furthermore, from regression analysis on the curves of **Figure 12**, the material model of EB-PBF Ti6Al4V parts at 8.33×10^{-4} s^{-1} strain rate can be developed correlating the ultimate tensile strength, σ_{UTS} (MPa), testing temperature (°C) for the samples with three different orientations. The extracted material models of the variation of tensile strength with temperature for flat-built, side-built, and top-built samples have been provided in **Equations 2**, **3**, and **4,** respectively.

$$\sigma_{UTS/xy} = -0.004T^2 - 0.5975T + 1011 \qquad 2$$

$$\sigma_{UTS/xz} = -0.001T^2 + 0.0875T + 736 \qquad 3$$

$$\sigma_{UTS/zy} = 0.0005T^2 - 1.1225T + 881 \qquad 4$$

Therefore, from the above analysis, it can be observed that the mechanical properties of EB-PBF Ti6Al4V samples are highly temperature-dependent. With increasing temperature, the ductility of the EBM Ti6Al4V part gets enhanced substantially at the expense of its strength of it. Hence appropriate consideration and measures should be taken before employing EBM parts in any high-temperature applications.

The high-temperature mechanical properties of both the EB-PBF built and conventionally built Ti6Al4V samples have been provided in

Table 6 for comparison purposes. The mechanical properties of conventional Ti6Al4V parts have been analyzed by J. H. Zhu et al. [27], J. Kim et al. [23] and S.H Wang et al. [52] at various temperatures and strain rates. Since the properties of Ti6Al4V parts are considerably sensitive to the test temperature and strain rate, these two variables need to be as close as possible for comparing the behaviors of EB-PBF materials with the conventional ones. The temperature and strain rate used by J. H. Zhu et al. during testing the Ti6Al4V parts produced by CHIP (the combination of cold and hot isostatic pressing) were very similar to the test conditions used in this current study. It can be observed that the EB-PBF flat-built sample has yield strength, UTS, and percent elongation higher than the CHIP sample by 2.6%, 6.9%, and 41% respectively. Whereas, though both the side-built and top-built samples have lower yield strength and UTS values, they have higher percent elongation than the CIP sample.

Table 6 The comparison of high-temperature mechanical properties of Ti6Al4V parts produced by EB-PBF additive manufacturing and conventional manufacturing processes.

Manufacturing Process		Temperature (°C)	Strain Rate (s^{-1})	0.2% Yield Strength (MPa)	UTS (MPa)	Elongation (%)	Reference
EB-PBF	Flat-built	600	8.3×10^{-4}	392	495	22	Current Study
	Side-built			354	423	24	
	Top-built			338	392	32	
CHIP		538	6.7×10^{-4}	382	463	15.6	[48]
Conventional		500	8.3×10^{-3}	436	467	31.2	[23]
Cold rolled		450	6.6×10^{-4}	505	592	28	[52]
EB-PBF (Ti6Al4V ELI)		600	1.5×10^{-3}	340	390	13	[83]

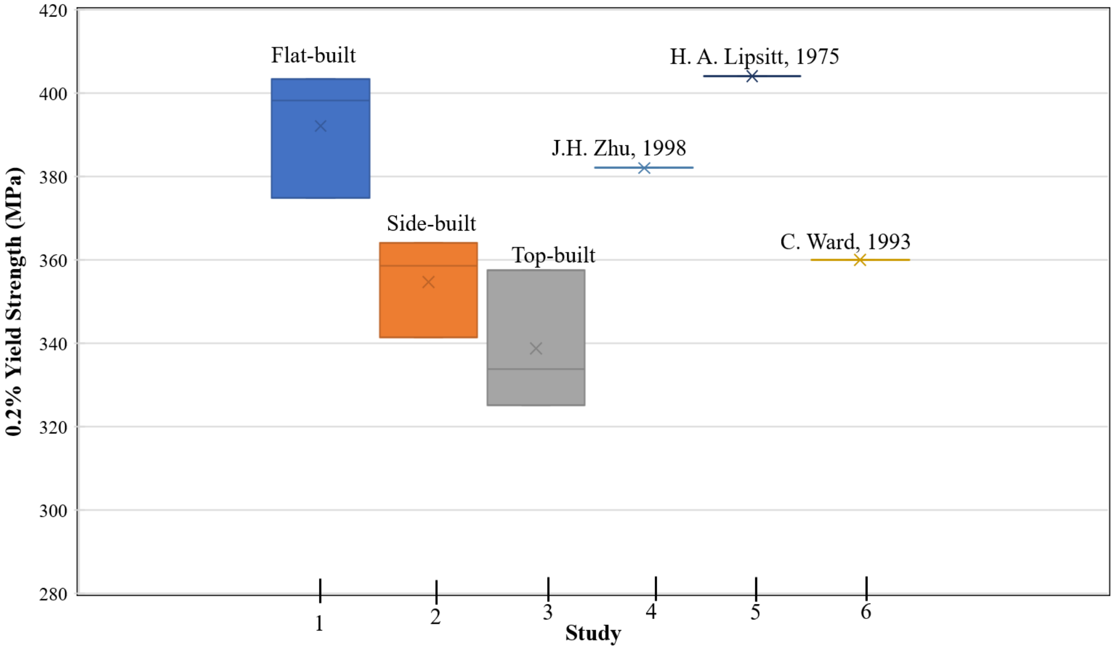

Figure 14 The comparison of 0.2% Yield Strength of different titanium alloys with current measurements at around 600°C temperature.

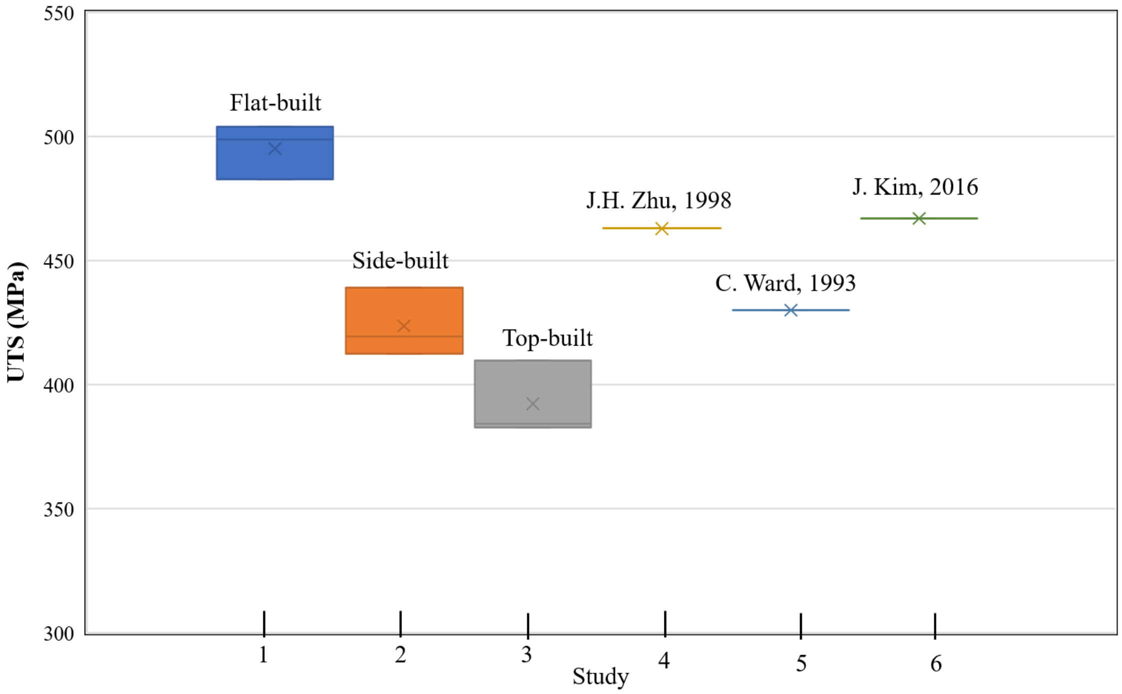

Figure 15 The comparison of the ultimate tensile strength (UTS) of different titanium alloys with current measurements at around 600°C temperature.

Similarly, although J. Kim et al. and S.H Wang et al. have found higher strength values than all three EB-PBF built orientations and a little bit lower ductility than the top-built sample using a different set of test conditions, it can be hypothesized that those values will be very close to each other at similar test conditions. Thus, from the above discussion, it can be realized that EB-PBF Ti6Al4V parts resulted in pretty similar high-temperature mechanical properties as compared to traditionally produced parts, as also can be observed in the **Figure 14** and **Figure 15**. In some cases, the EB-PBF parts even displayed better ductility than conventional parts. Besides, the mechanical properties of as-built EB-PBF Ti6Al4V ELI alloy, built-in XZY orientation, obtained by Aliprandi et al. [83] using a test temperature of 600°C and strain rate of 1.5×10^{-3} s^{-1}, have been added in the table. This comparison shows that the side-built Ti6Al4V ELI alloy has similar strength but lower ductility than the top-built Ti6Al4V sample, both produced by the EB-PBF process.

4.2.3 Fractography Analysis

The fracture pattern of the EB-PBF Ti6Al4V specimens under tensile loading at different temperatures is presented in **Figure 16**. At 600°C, the flat-built and side-built samples display ductile cup-and-cone fracture, whereas the top-built sample shows ductile shear fractures at an angle of 45° from the loading direction, as shown in **Figure 16**a. Also, a similar kind of ductile shear fracture pattern is observed for top-built samples tested at two other temperatures (400°C and 200°C) as well as can be seen in **Figure 16**b. Further analysis of the fracture surfaces of the various samples reveals crucial information regarding the fracture pattern. **Figure 17** shows the optical microscopy images of the fracture surfaces of different EBM Ti6Al4V samples tested at 600 °C. The flat-built and side-built samples exhibit a cleavage mode of fracture where the tensile stress acts normal to the crystallographic cleavage plane. Here the fracture surface also appears as a bright and granular fracture, as can be seen in **Figure 17**a and **Figure 17**b. In the fracture surfaces of all the samples, the presence of various defects like unmelted powders, pores, and keyholes was noticed when seen under a microscope. These defects could be the possible crack initiation and propagation sites under applied stress since the propagating cracks nucleate from the pile-up of glide dislocations at various defects [101]. The long columnar grains perpendicular to the loading direction and parallel to the build direction could also be observed from the fracture surfaces of both the flat-built and side-built samples. These two samples might also undergo intergranular fracture, where the crack propagates along the grain boundaries. The side-built sample shows the river pattern on the fracture surface as can be seen in **Figure 17**b. From this figure, an un-melted sub-surface powder particle zone could be noticed. Under the applied loading, the crack possibly initiated from this partially melted zone and propagated, creating a river pattern as indicated by the arrows.

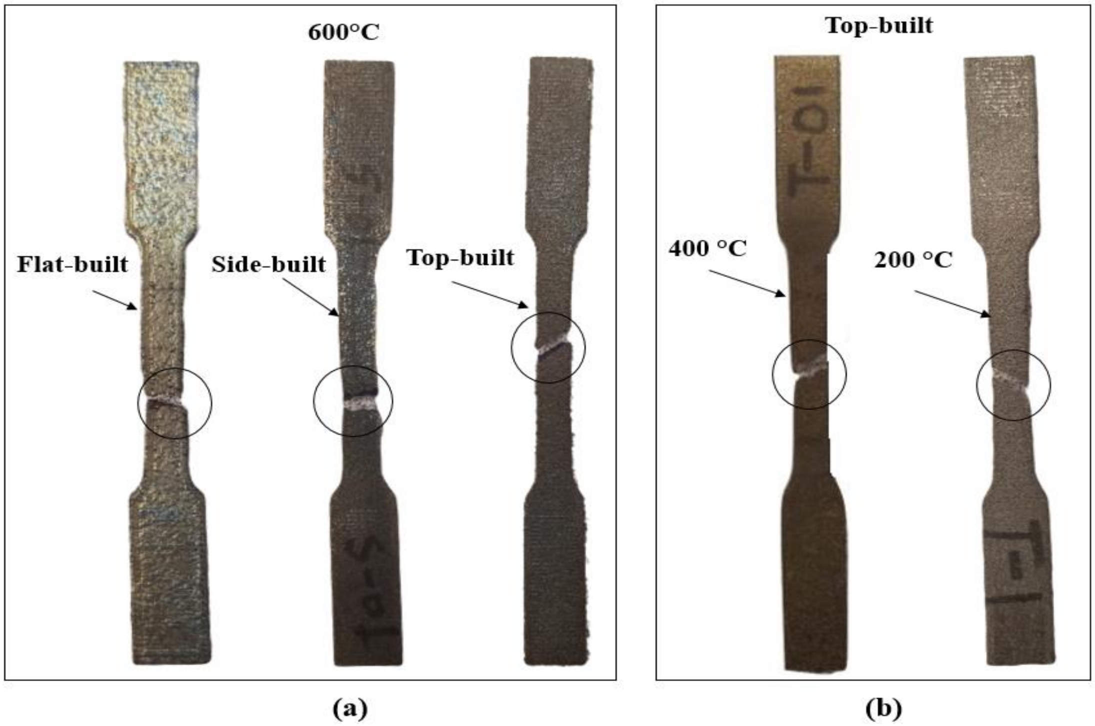

Figure 16 Fracture pattern of EBM Ti6Al4V parts under tensile loading, (a) at 600°C for samples with three different orientations, (b) for a top-built sample at two other temperatures.

However, the top-built samples tested at all three temperatures show a shear fracture which might be due to the extensive slip on the active slip plane caused by shear stresses. Here, the fracture surface appears highly fibrous and reddish in the middle and purple on the sides in color, as can be seen in **Figure 17**c. The fracture surface indicates a significant amount of plastic deformation before fracture. The fracture surface also appears as equiaxed since the applied tensile load was parallel to the long columnar grain. Hence, the fracture here could be trans-granular, where the crack propagates across the grain. The possible crack initiation sites could be the un-melted powders and/or pores situated between the successive layers.

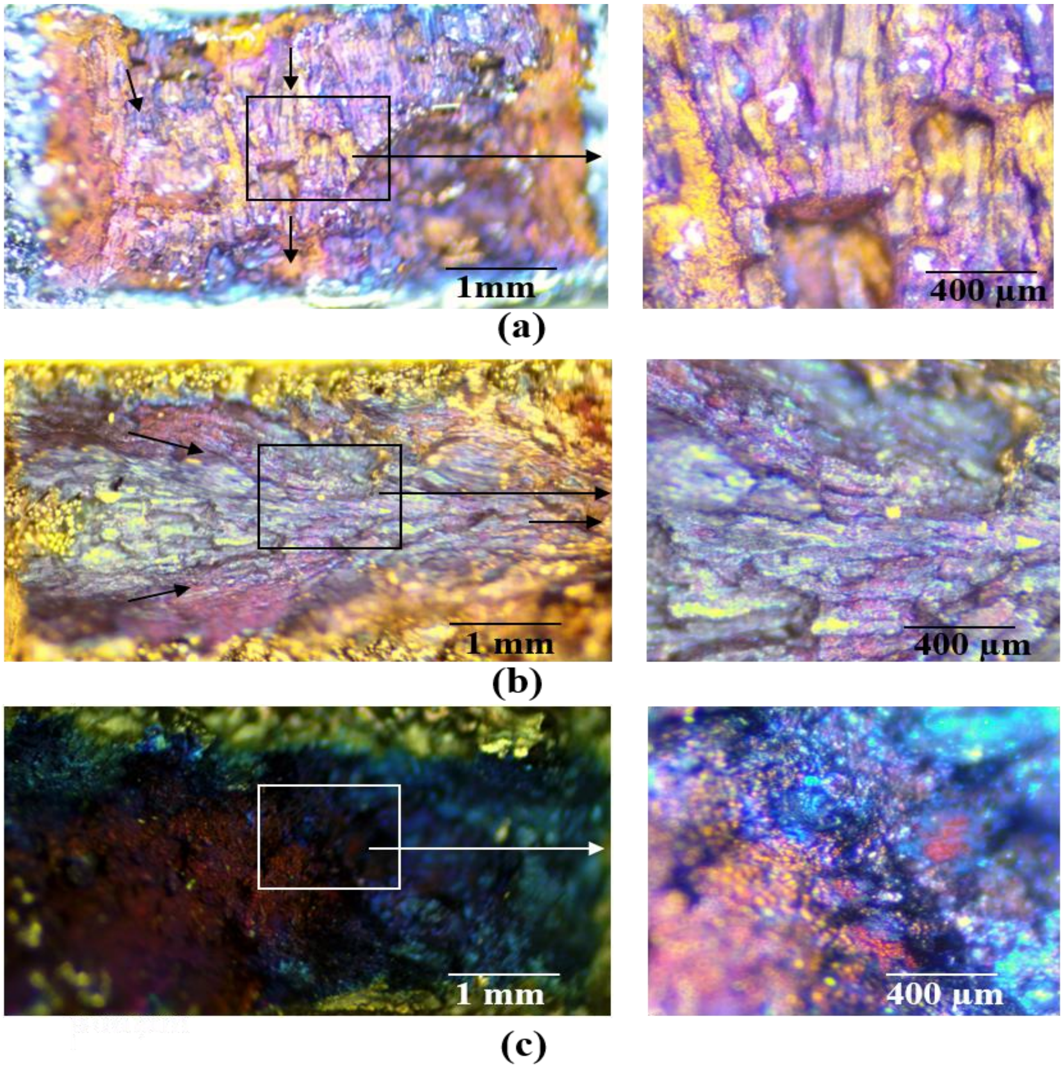

Figure 17 Optical microscopy images taken from fracture surfaces of EBM Ti6Al4V parts tested at 600 °C temperature, (a) Flat-built, (b) Side-built, and (c) Top-built sample.

Interestingly, the smoothness and color of the fracture surface change with the testing temperature, as can be seen for the fracture surface of the top-built sample presented in **Figure 18**. The fracture surface obtained from the experiment conducted at 200°C **(Figure 18**a) is smoother than the surface at 600°C (**Figure 18**b). This indicates that the tensile fracture at high temperature undergoes significant plastic deformation as opposed to the tensile fracture at low temperature. The fracture surface taken from the low-temperature test is colorless, while at high temperature, the color of the fracture surface becomes a mix of gold, blue and purple. This color change could be due to the formation of oxide layers at this high temperature [52]. However, at 600°C temperature, the thickness of the Titanium oxide layer is not significant enough to influence the tensile properties of Ti6Al4V alloy [24]. As a result, the ductility has not been compromised by oxidation in this analysis. Though excessive oxidation could occur at a temperature higher than 600°C and which could lead to brittle fracture.

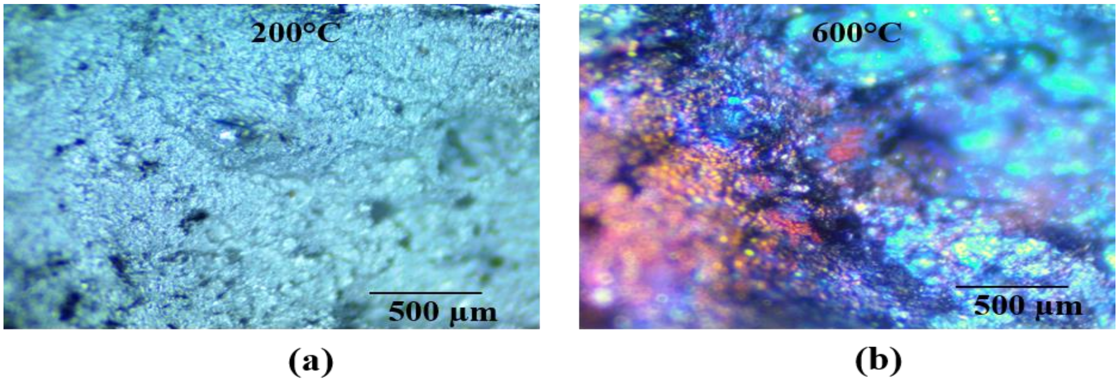

(a) (b)

Figure 18 Optical microscopy images taken from fracture surfaces of the top-built sample tested at (a) 200°C and (b) 600°C.

When examined under filed emission scanning electron microscope (FESEM), the fracture surfaces exhibit additional details about fracture patterns, and various defects present inside the as-built EBM Ti6Al4V parts, as shown in **Figure 19** and **Figure 20**. Most of the propagating cracks initiate from the surface or sub-surface defects of partially melted or un-melted powder zones (**Figure 19**g) and then propagate along the build direction. The white arrows in **Figure 19**a & **Figure 19**b show the crack propagating directions for flat-built and side-built samples. Various internal defects like pores, keyholes, and un-melted powder particles, as can be seen in **Figure 19**e, **Figure 19**f, **Figure 19**h, **Figure 19**i, and **Figure 20,** accelerate the crack propagation and thus degrade the mechanical properties. At all three temperatures, the flat-built samples display a smoother fracture surface than the other two orientations, while the top-built samples have the roughest fracture surface because of longer plastic deformation. With the increasing temperature, fracture surfaces become rougher for any orientation as well.

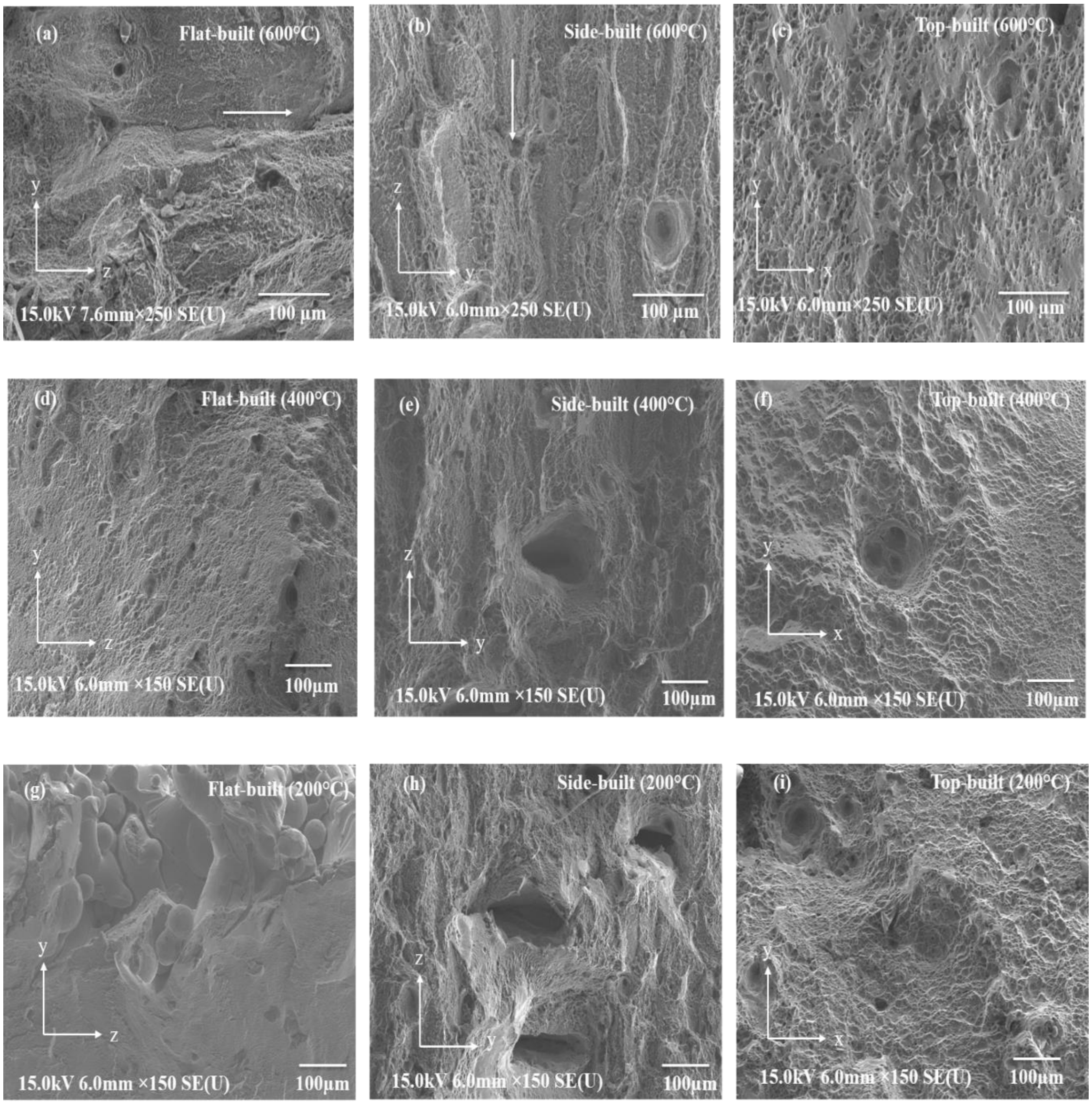

Figure 19 Secondary Electron Microscopy (SEM) images with coordinate systems of the fracture surfaces (taken at mid-cross section) of as-built EBM Ti6Al4V flat-built, side-built, and top-built samples tested at three different (600°C, 400°C, and 200°C) temperatures.

For example, the fracture surface of the top-built sample tested at 200°C (**Figure 19**i) has a β phase along the grain boundaries. In EBM build parts, the columnar β grain grows along the build direction surrounding the α phase. And the slip system was found to be active parallel to the α platelets [17,45]. Hence this β phase inhibits the dislocation motions. These dislocations pile up around the β phase, causing work hardening at this temperature resulting in low plastic deformation. For the fracture surface tested at 400°C (**Figure 19**f), the dimples get inflated because of the increase of atom movements with increasing temperature. The top-built sample tested at 600°C undergoes a decrease in dislocation density and grain boundary slip, which causes the plasticity of this sample to increase further with metal softening [104]. These dislocation mobility processes, during high-temperature plastic deformation, have a propensity to neutralize the work hardening effect. As a result, significant softening behavior was observed at the high-temperature deformation curve presented beforehand. The fracture surface of the top-built sample tested at 600°C (**Figure 19**c) possibly indicates dislocation motion when compared with the fracture surface tested at 400°C (**Figure 19**f). The 600°C surface has a deeper and larger number of inflated dimples than the low-temperature counterpart.

Moreover, high-temperature deformation of Ti6Al4V alloy mainly undergoes softening behaviors due to the decrease of dislocation density, grain boundary slip, and dislocation glide and climb [105]. These softening mechanisms depend on various factors, such as temperature, strain rate, and degree of strain. The DRV type softening mechanism has a propensity to neutralize the work hardening effect. On the other hand, under the DRX type softening mechanism, the flow stress reaches a peak value very rapidly due to strain hardening, then drops slowly until the failure. During the hot deformation of Ti6Al4V alloy in the temperature range larger than the β-transus (995 °C) temperature, where the phase transformation from α+β phase to β phase occurs, the DRV type softening mechanism is observed to be the dominant process [105],[56]. During DRV, the concentration dislocation density at the grain boundaries decreases substantially, enabling a higher degree of cross slip, climb, and dislocation unpinning. While in the temperature range of the α+β phase field, which is between 850-950 °C, both the DRV and DRX softening mechanisms are found to be activated, leading to grain refinements [53],[106]. In the α phase-field temperature (below 800 °C) DRV mechanism become very slow and rarely observed. The hot deformation in this temperature region is dominated by work hardening (WH) and DRX. The onset temperature for dynamic crystallization was found to be 500 °C, where flow softening starts to begin due to the accumulation of energy after a certain critical strain is achieved [60]. Although no phase transformation occurs during hot deformation at 600 °C temperature, both the α and β phases might undergo refinement, elongation, and rotation resulting in microstructural evolution. Besides, a significant amount of grain refinement due to recrystallization leads to a sharp increase in grain size. Moreover, the columnar β grains get elongation along the loading direction, while some of the harder α phases might get partially dissolute into the softer β phase, increasing the ductility of the sample [107]. Various other softening or microstructure evolution mechanisms that could be present at 600 °C temperature are platelet local shear deformation, partial dissolution, and macroscopic shearing/bending along dynamic recrystallization [59].

4.2.4 Effect of Various Defects on Anisotropic Behaviors

The shape, orientation, and location of defects change with the build orientation as can be seen in **Figure 20.** For instance, **Figure 20**a & **Figure 20**b show various defects between the successive layers of the flat-built and side-built samples respectively. The observed voids are perpendicular to the build direction (z-axis) and elongated along the y-axis (parallel to the powder layers) as expected. While **Figure 20**c exposes a significant amount of unmelted powder zone defects just beneath the surface and near the build table for the side-built sample. Furthermore, partially melted sub-surface and surface defects of the top-built sample can be observed in **Figure 20**d. The observed variation of the internal defects and the consequent change in porosity values in different orientations are some of the significant reasons for the anisotropic behavior of LPBF and EB-PBF Ti6Al4V parts. The pores inside the samples could be created due to various reasons like unequal distribution of energy input at a different location inside the build chamber, entrapped gas porosity, and porosity of the powder particle itself [39][108]. The intensity of the cathode current could vary depending on the distance between the scanning location and electron beam source and the location of the sample on the build table. Due to the variation in the arrangement of the three different samples on the build table, they would likely face distinct energy input during the melting process at different locations. These could eventually bring about the phenomena of over-melting (keyhole defects) or under-melting (un-melted powder) of the samples with different orientations. Moreover, the amount of entrapped gas porosity could also change among the three samples with different orientations depending on the relative flow direction of the inert gas inside the chamber.

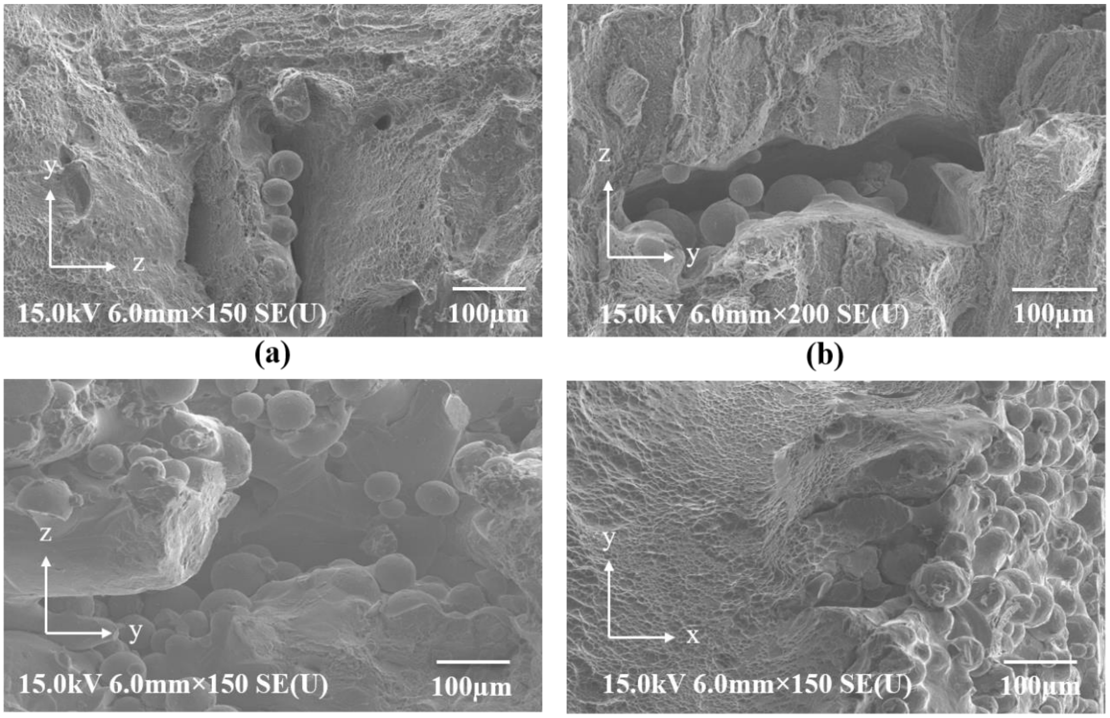

(a) (b) (c) (d)

Figure 20 Various defects were observed on SEM images of the fracture surfaces of different as-built EBM Ti6Al4V samples, (a) flat-built (400°C) at mid-cross section, (b) side-built (600°C) at mid-cross section, (c) side-built (400°C) near sub-surface, and (d) top-built (400°C) near-surface, tested at different temperatures.

The flat-built sample showed a porosity of 0.17 %. Whereas both the side-built and top-built samples have shown a pretty similar porosity value of around 0.05%. The high porosity value of the flat-built sample, as compared to the other two orientations, is mostly because of the insufficient melting of powder particles along a long region of this sample. However, in the flat-built sample, the majority of the defects were entrapped gas porosity and a very tiny amount of unmelted powder particles. But both the side-built and top-built samples had a similar kind of defect distribution inside them. In these two samples, porosity and another kind of internal defects were distributed very homogeneously. There were no significant un-melted or partially melted powder particle regions in these two samples as opposed to the flat-built sample. Though the flat-built sample has a poor porosity value, at the same time, it displayed superior mechanical properties compared to the other two orientational samples. Further details of the inherent porosity and defect analysis of EBM-built Ti6Al4V samples will be discussed in **section 4.6**.

Besides, the surface roughness of all three as-built Ti6Al4V samples has also been measured using a stylus profilometer named Ambios XP-200 before tensile testing. It was found that this external defect hardly varies with the build orientations. The average surface roughness (Ra) values of the flat-built, side-built, and top-built samples were measured and found to be 20 µm, 21 µm, and 25 µm, respectively. Further details of the surface profile measurements will be discussed in section 4.3. Hence, it indicates that the porosity and surface roughness do not have any significant effect on the anisotropic behavior of EB-PBF Ti6Al4V parts. Therefore, the microstructural variation, due to the change of cooling rates and thermal gradient in different build orientations, might be the substantial reason for the anisotropic behavior of EBM Ti6Al4V samples.

4.3 Microstructural Evolution Before and After High-Temperature Tensile Testing of EB-PBF AM Ti6AL4V parts

4.3.1 Crystallographic Sample Preparation

The details of the EBM processing parameters can be found elsewhere [95] and also in section 4.1. Samples printed in three different orientations are named flat-built, side-built, and top-built samples, as shown in **Figure 21**. The flat-built and side-built samples have experienced tensile loading parallel to the printed layers, whereas the top-built sample was loaded perpendicular to the stacked layers. Test coupons for structural analysis were collected from the XZ planes from all three samples to make a direct comparison between them and their effects on the resulted mechanical properties (**Figure 21**). Furthermore, another batch of test coupons was collected from the XY plane of the flat-built sample to observe the microstructural variations on two different planes of the same sample (**Figure 21**).

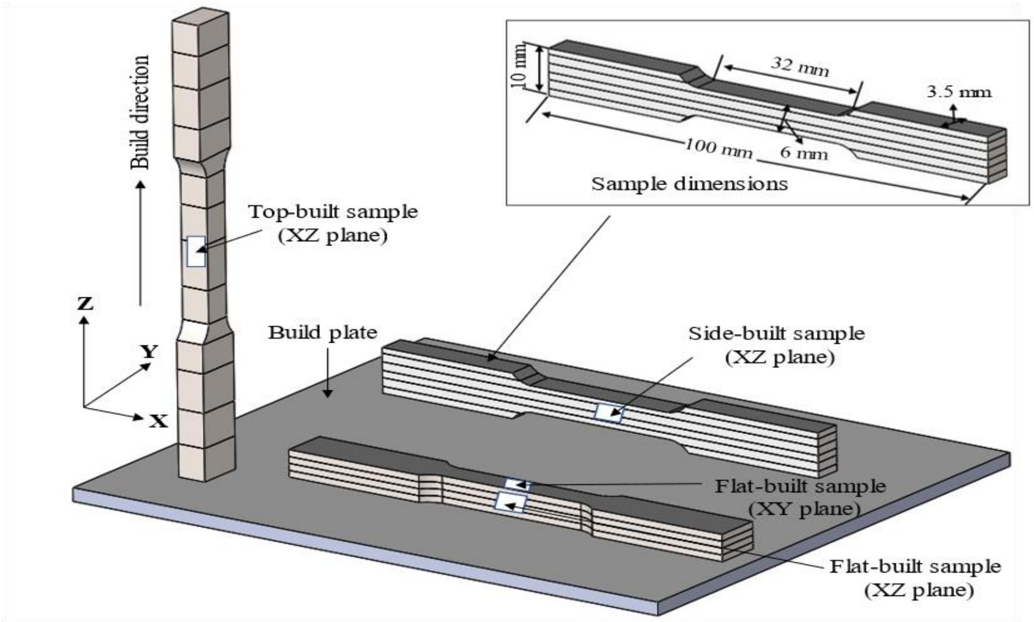

Figure 21 Crystallographic test coupons extracted and prepared from the three types of samples (i.e., flat-built, side-built, and top-built) for microstructural evaluation are marked with white boxes.

The crystallographic samples were prepared using a standard polishing process. The test coupons were polished gradually to the finer silicon carbide (SiC) grit sizes. The second stage of polishing was performed on low-napped synthetic rayon polishing cloth using 1 µm, 0.25 µm, and 0.1 µm diamond suspensions sequentially. Eventually, vibratory polishing was performed using 0.05 µm colloidal silica to get rid of the residual stresses and to obtain a mirror surface finish. The samples were cleaned properly using soap solution and acetone between the steps to prevent the carriage of coarser particles to the next level. During the finer polishing steps, it is very difficult to remove the scratches from the previous steps. Therefore, before moving to the next step, all samples were cleaned using ultrasound sonication in acetone solution. Finally, after the vibratory polishing, all samples were further cleaned in an ultrasound sonicator using acetone, methanol, and isopropyl alcohol (IPA), respectively, before conducting an EBSD analysis on them. At each orientation, a total of 15 samples were printed for various mechanical and microstructural analyses. The surface roughness, internal porosity, hardness, and tensile properties were measured on the three different samples to examine how they vary with the orientations. Tensile tests were also performed at different high temperatures as well to observe how the mechanical properties change with the temperature. The various measurements and their outcomes are discussed in previous sections and later sections. Eventually, microstructural analysis was performed on the samples before and after the tensile test at high temperatures to understand various deformation mechanisms activated during elevated-temperature tensile loading.

4.3.2 Mechanical Properties of EBM Built Sample

At each orientation, a total of 15 samples were printed for various mechanical, surface roughness, porosity, and microstructural analyses. The mechanical properties of the as-built EBM Ti6Al4V sample built in three different orientations were measured to examine their anisotropic behavior. The tensile test was conducted using an MTS Criterion® Electromechanical Universal Test System modeled as MTS C45 (MTS Systems Corp, Eden Prairie, MNcity, USA), on strain control mode and with a strain rate of 6.67 × 10−4 s−1. The load cell used was called MTS LPS.504, having a force capacity of 50 kN. The extension data was collected using an Epsilon® axial extensometer (Epsilon Technology

Corp., Jackson, WY, USA) with a gauge length of 10 mm and modeled as 7642-010M-075M. Tensile tests were also performed at different high temperatures up to 600 °C to observe how the mechanical properties change with the temperature. The temperature inside the environmental chamber was controlled using Eurotherm® 2404 temperature controller (Eurotherm by Schneider Electricmanufacturer, Worthing, United Kingdom). All the obtained mechanical properties at different temperatures are presented in the following **Table 7**. Some more details of the measurement techniques could be found elsewhere [95,109].

Table 7 Mechanical properties of the as-built EBM Ti6Al4V specimens built in three orientations with the build table

Sample Orientations	Temperature (°C)	Modulus of Elasticity, E (GPa)	0.2% Yield Strength (MPa)	Ultimate Tensile Strength (MPa)	Percent Elongation (%)
Flat-built	RT	116	965	1065	4.02
	200	103	865	871	2.62
	400	88	623	702	4.07
	600	73	392	495	22.30
Side-built	RT	94	803	881	10.05
	200	82	666	713	12.23
	400	76	514	609	7.73

	600	64	355	424	24.60
Top-built	RT	92	724	807	12.06
	200	86	623	677	18.31
	400	72	412	514	10.18
	600	64	339	392	24.60

The flat-built sample displayed superior mechanical behavior to the other two build orientations in the case for all tensile properties except percent elongation. The former has an excellent modulus of elasticity, strength, and hardness values which are comparable to the conventional wrought Ti6Al4V alloys [84,85]. On the contrary, it has a very poor percent elongation. This low value of the percent elongation might be due to its high porosity and detrimental internal defects because of the insufficient melting of the powder particles. Though both the side-built and top-built samples have outstanding percent elongation values, their other properties are either similar or considerably lower than their traditional wrought counterpart. The anisotropic mechanical behavior of the as-built EBM Ti6Al4V parts could be apparent from the above table. The flat-built sample has 23.4% and 26% higher modulus of elasticity than the side-built and top-built samples, respectively. The latter two have a very similar modulus of elasticity. The former has excellent 0.2% yield strength, which is 20% and 33% greater than the latter two samples, respectively. Again, the flat-built sample has exceedingly well ultimate tensile strength, which is almost 21% and 32% larger than the other two later orientations, respectively.

In this analysis, the EBM Ti6Al4V parts from three different build orientations have been tested at three different high temperatures, which are 600°C, 400°C, and 200°C, and compared with the room temperature (RT) properties. The high-temperature deformation mechanisms are studied further through microstructural analysis of the samples after the tensile testing. All the samples showed considerable temperature dependency of the various mechanical properties. With the increasing temperature, a significant increment of the ductility could be observed at the expense of the elastic modulus and strength properties in all three different orientations. At 600 °C temperature, a significant decrease in flow stress and consequent softening behavior was observed at all three different orientations. It is hypothesized that this apparent softening behavior was due to various mechanisms activated at high enough temperatures, such as the increased mobility of the inherent dislocations, which caused the dislocation density to be decreased, grain growth and coarsening, and grain boundary slip [95]. The potential underlying mechanisms will be examined thoroughly with the help of EBSD analysis in this current study. Moreover, some samples from all orientations have excessively high porosity values because of the elongated lack of fusion defects. Those defects contributed to premature failure under tensile loading. Consequently, some samples displayed relatively poor strength properties and percent elongation as compared to the specimens with minimum internal defects. As a result, the percent elongation properties are found to be inconsistent and highly nonlinear in nature in some cases, as displayed in **Table 7**.

4.3.3 Working Principle of EBSD

Electron backscatter diffraction (EBSD) is a scanning electron microscopy (SEM) based diffraction technique where the diffraction patterns (Kikuchi bands) are collected from the bulk sample captured on SEM [110]. When the source electron beam interacts with the specimen, backscattered electrons are generated beneath the surface of the specimen. Those backscattered electrons, spreading in different directions, further interact with various crystal planes of the materials. The backscatter electrons diffracted from different crystal planes of the specimens follow Bragg law ($n\lambda = 2dsin\theta$) and thus provides crucial information about the microstructural features of the materials. Here, n is an integer, λ is the wavelength of the electrons, d is the spacing of the diffracting crystal plane, and θ is the incidence angle of the electrons on the diffracting plane [111].

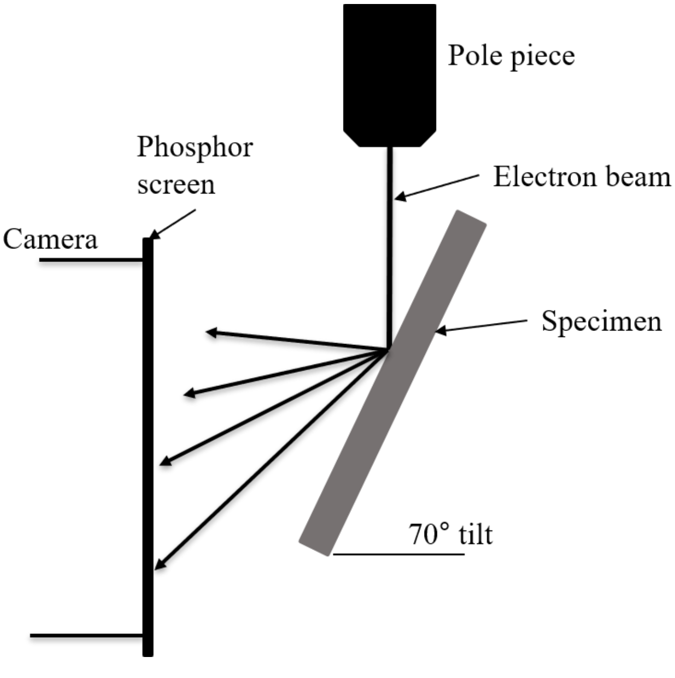

Figure 22 Schematic diagram and working principle of EBSD

The working principle of the EBSD technique is very straightforward (**Figure 22**). The focused electron beam from the SEM source is applied to the crystalline sample which is tilted 70 degrees. The generated backscattered electrons are then directed to a fluorescent phosphor screen which is seen using a charge-coupled device (CCD) video camera. The main feature of the EBSD pattern is the Kikuchi bands which are the projection of crystal planes to the phosphor screen. Kikuchi bands can be indexed with the help of Miller indices of the corresponding diffracting crystal planes. The diffracting crystal orientations can be obtained from the position of the Kikuchi bands. The width of the Kikuchi bands is also a very important parameter and provides information regarding the d-spacing of the diffraction plane. The width is inversely proportional to the d spacing[112].

The EBSD is a very powerful technique that provides various quantitative metallographic information about the sample, including the crystal orientation, grain and sub-grain size and shapes, texture, misorientation angles, and phase distribution. It also provides different visual maps of the grain orientation and phase distribution. To obtain a good quality EBSD pattern, several parameters are very important and need to be considered carefully. Most importantly, the surface quality of the materials needs to be excellent and mirror-polished. Therefore, mechanical grinding and polishing of the specimens need to be done with great importance and care. Titanium is a hard and difficult material to polish, and extra caution is needed while handling this material. Speed of the data acquisition, background removal, high probe current, high accelerating voltage, optimum working distance, and special resolution are some of the other important parameters which dictate the quality of the diffracting patterns [110,111,113].

4.3.4 EBSD Instrument Used for This Analysis

The electron backscatter diffraction (EBSD) analysis was conducted on the as-built samples to observe their crystallographic textures, grain orientations, grain sizes, and grain boundary misorientation angles. The EBSD scans were accomplished using a ZEISS FIB-SEM (Carl Zeiss AG, Oberkochen, Germany) instrument equipped with an EDAX®|AMETEK® EBSD detector (EDAX-AMETEK Inc. Mahwah, NJ, USA). The source electron was emitted at the sample at 20 kV at high current mode using an aperture size of 120 µm. The focused electron beam from the SEM source was applied to the crystalline sample, which was tilted 70 degrees. The generated backscattered electrons were then directed towards the detector for capturing the EBSD Kikuchi bands. Both the 500× and 3000× magnifications were used for capturing EBSD images at two different scales. The scan area for 500× magnification was 175 µm × 175 µm with a step size of 0.1 µm. The scan area for 3000× magnification was 30 µm × 30 µm with a step size of 0.06 µm. The total dwell time for each of the scans lasted for around 3–4 h. Furthermore, the OIM Analysis v8 software (EDAX-AMETEK Inc., Mahwah, NJ, USA) was used for analyzing the scanned images and obtaining various grain maps and information.

4.3.5 Effect of Microstructure on Anisotropic Behavior via EBSD Analysis

4.3.5.1 Anisotropic Mechanical Behavior

The representative engineering stress-strain curves of the three types of EBM Ti6Al4V samples are presented in **Figure 23**. The flat-built sample displays superior mechanical behavior for all tensile properties except percent elongation. The flat-built sample also has an excellent modulus of elasticity, strength, and hardness values which are comparable to the conventionally wrought Ti6Al4V alloys [84,85]. On the contrary, it has a very poor percent elongation. Although both the side-built and top-built samples have outstanding percent elongation values, their other properties are considerably lower than their traditionally wrought counterpart. Therefore, the anisotropic mechanical behavior of the as-built EBM Ti6Al4V parts is clearly apparent from the presented stress-strain curves. The flat-built sample has a 3.3% and 23.3% higher modulus of elasticity than the side-built and top-built samples, respectively. Both the flat-built and side-built samples have very similar moduli of elasticity. The flat-built samples have an excellent 0.2% yield strength, which is 4.2% and 35.2% greater than the side-built and top-built samples, respectively. Again, the flat-built sample has a high ultimate tensile strength, which is 9.4% and 31.1% larger than the latter two orientations, respectively. The Vickers hardness values display a similar trend as the strength properties. The Vickers hardness values of the flat-built, side-built, and top-built samples are 345 ± 7, 318 ± 6, and 294 ± 8 HV (kgf/mm2), respectively. The flat-built sample has a 17.34% larger Vickers hardness value than the top-built one. The flat-built sample, being very close to and sharing a higher cross-sectional area with the build table, has a lower thermal gradient than the other two orientational samples.

Therefore, the flat-built sample receives more time to convert a higher amount of the primary soft beta phases to the harder alpha phases. This low percentage of softer beta phases in flat-built samples makes them harder and less ductile than the side-built and top-built samples, respectively, as can be observed from both the tensile test and micro-hardness test results.

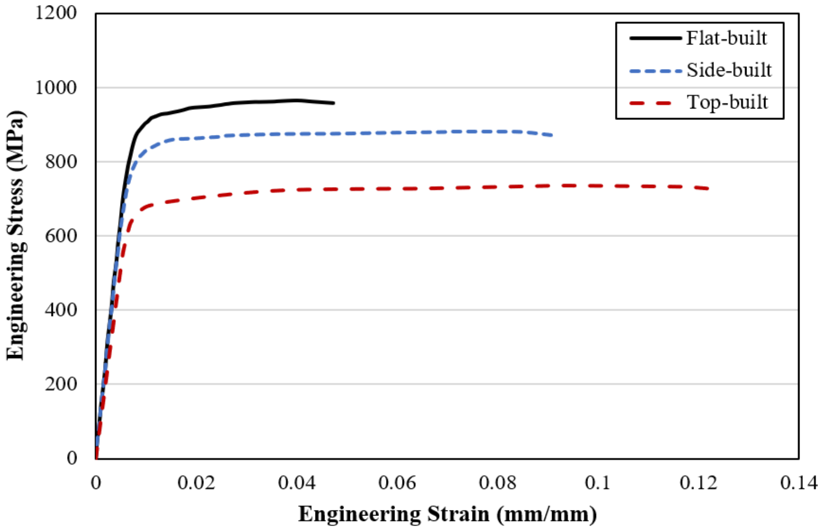

Figure 23 Engineering stress-strain curves of EBM Ti6Al4V parts from three different orientations (flat-built, side-built, and top-built) showing anisotropic flow stress properties

4.3.5.2 Microstructural EBSD Analysis Before Tensile Testing

A microstructural analysis on EBM Ti6Al4V samples built in three different orientations was conducted using EBSD, as discussed below. Initially, the two surfaces, located on the planes which are parallel and perpendicular to the build direction of the flat-built sample, were analyzed to observe their microstructural changes, as presented in **Figure 24**. The inverse pole figure (IPF) of the parallel XZ plane (**Figure 24**a) shows grains distributed in the preferred orientation with α platelets and α colonies. On the contrary, the IPF of the XY plane, which is perpendicular to the build direction (**Figure 24**b), displays equiaxed and randomly orientated grains. The alpha pole figure of harmonic texture (**Figure 24**c & **Figure 24**d) shows more α variants, with various grain colors on the XY plane and with a maximum texture intensity of 7.386, as compared to the XZ plane, which has a maximum texture intensity of the 8.989. On both planes, the grain orientations of the α phases are in three preferred orientations of <0 0 0 1>, <1 1 2¯0>, and <1 1 2¯1>, whereas the beta pole figure of harmonic texture (**Figure 24**e & **Figure 24**f) indicates more beta variants on the XY plane with a maximum texture intensity of 2.598, as opposed to the XZ plane where the maximum texture intensity is 2.348.

Furthermore, the XY plane also contains a greater fraction of the beta phases than the XZ plane (**Figure 24**g & **Figure 24**h). The former plane has 21% beta phases while the latter plane has only 5%. The higher fraction of the beta phases on the XY plane compared to the XZ plane could be due to several reasons. For instance, during the building process, the layers further away from the build table have higher temperature gradients and higher cooling rates than the layers closer to the build table. The bottom layers face a greater number of subsequent melting and solidification steps than the top layers that are further away from the build table. Therefore, the location of the XY plane, being distant from the build table, causes phases on them to get less time to transform from prior beta phases to alpha phases, and thus the XY plane possesses a higher percentage of beta phases than the XZ plane. Again, the columnar grain growth along the building direction of the XZ plane, which is parallel to the building direction, has elongated α platelets, which form several α colonies with similar preferred grain orientations possessing similar grain colors. The columnar grain growth stratifications can be observed in **Figure 24**a, as opposed to the randomly distributed grains with different grain colors on the plane perpendicular to the build direction (**Figure 24**b).

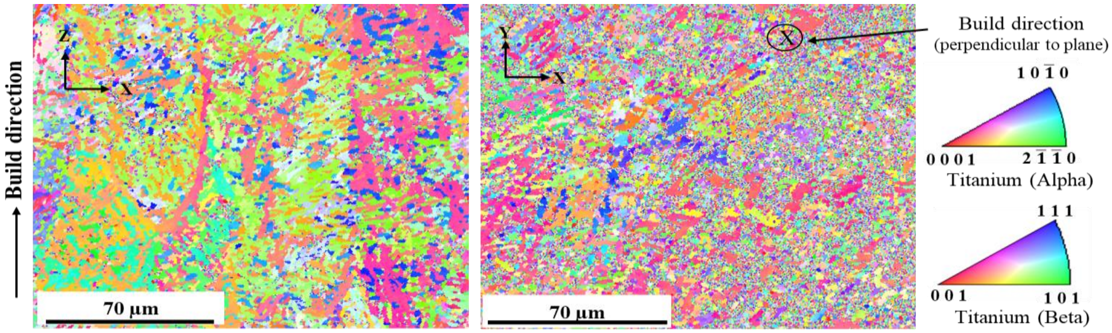

(a) IPF map of flat-built (XZ plane) **(b)** IPF map of flat-built (XY plane)

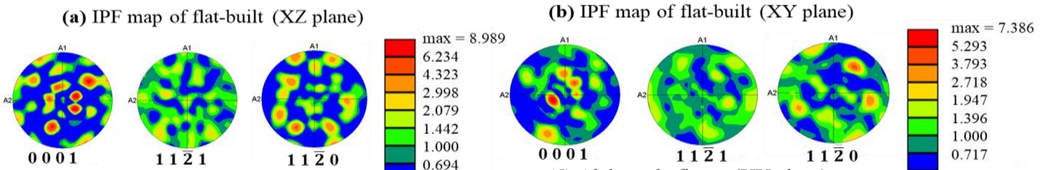

(c) Alpha pole figure (XZ plane) **(d)** Alpha pole figure (XY plane)

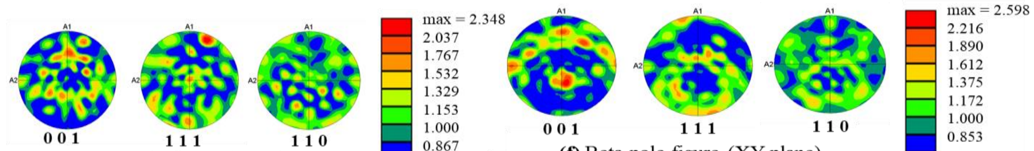

(e) Beta pole figure (XZ plane) **(f)** Beta pole figure (XY plane)

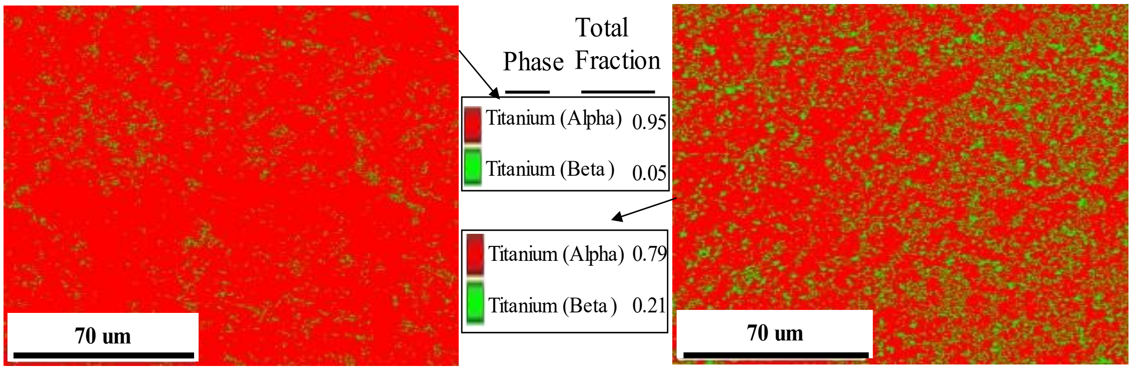

(g) Phase map of XZ plane

(h) Phase map of XY plane

Figure 24 Inverse pole figure (IPF) of the flat-built sample: (a) XZ plane showing grains distributed with preferred orientations; (b) XY plane showing randomly oriented equiaxed grains, along with alpha pole figure of the harmonic texture of (c) XZ plane and (d) XY plane; beta pole figure of the harmonic texture of (e) XZ plane and (f) XY plane, and phase maps (g,h) of the two planes.

The inverse pole figures of the XZ plane of flat-built, side-built, and top-built samples (**Figure 25**) again confirm the columnar grain growth along the build direction. This columnar grain can typically be several millimeters long, and its orientation and growth direction are dictated by the largest temperature gradient towards the build plate during the rapid cooling process [40,42,43]. The IPF maps further show that the grains in the microstructure consist mainly of α colony, α basketweave, and prior β phases, which are distributed among the alpha phases and can be seen in **Figure 25**a–c. The α colonies are made of the α platelets which have parallel grain orientation and belong to the same grain category of the Burger relationship. In the basket weave, the alpha grain classification has α platelets with different α categories and with different preferred grain orientations, as distinguished by various grain colors. From the fractography analysis in **section 4.2.3**, it was observed that the top-built sample undergoes ductile shear fractures at an angle of 45° from the loading direction, and the flat-built and side-built samples undergo ductile cup-and-cone fractures. The reason behind these types of fractures can be observed from the IPF maps of the three samples, as shown in **Figure 25**. The fracture propagates along the shear plane of the sample. In the top-built sample, the shear plane is at an angle of 45° with the loading direction, whereas the shear planes in both the flat-built and side-built samples, are almost perpendicular to the loading direction, resulting in the displayed cup-and-cone fractures.

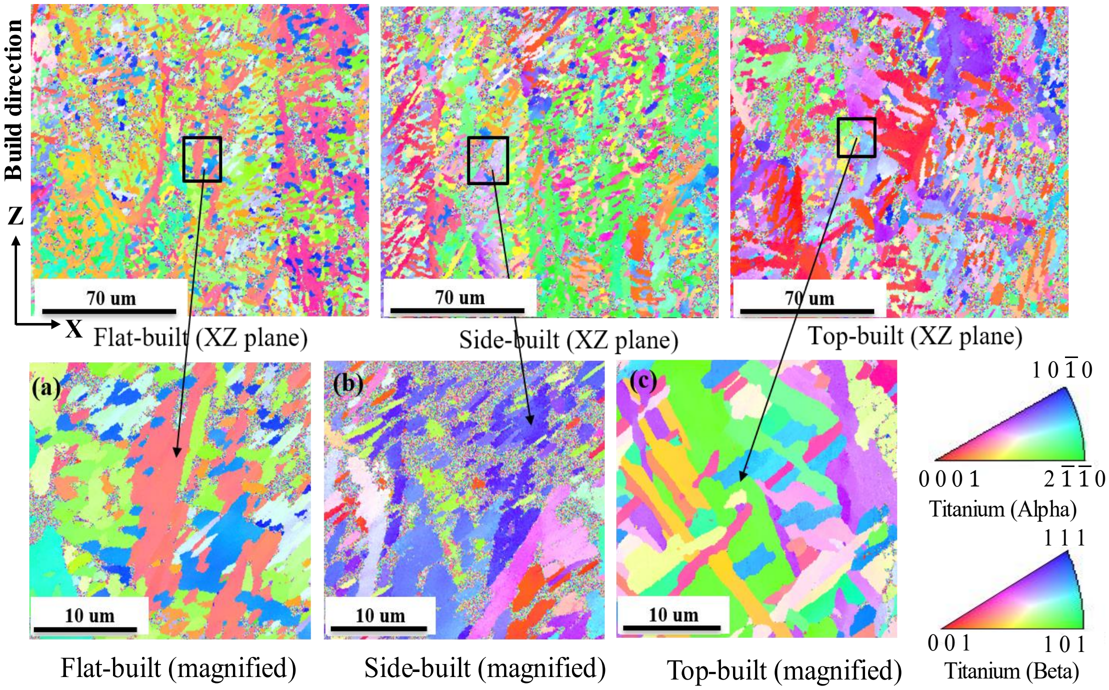

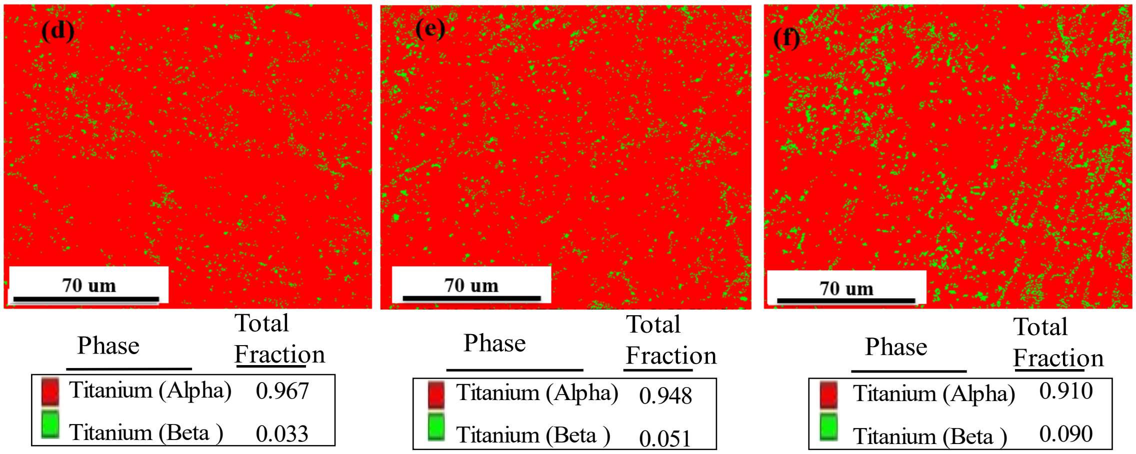

Figure 25 Various EBSD maps of the three Ti6Al4V samples. The top three inverse pole figure (IPF) maps show different preferred grain orientations on the three samples. IPF maps at higher magnification display (a) elongated grain boundary, (b) alpha colonies, and (c) alpha basket weave platelets, while phase maps (d–f) show prior beta phases in between the alpha grain boundaries of flat-built, side-built, and top-built samples, respectively.

Furthermore, the variation in the microstructure formation and preferred grain orientations in the three samples with three build orientations can also be observed in **Figure 25**. The flat-built, side-built, and top-built samples display significant distinctive grains in different preferred orientations, as is also highlighted by phase color maps along with IPF maps. The organization of grains in different preferred orientations is dictated by the higher thermal gradient direction during the solidification and cooling of the molten powder layers [41][42]. Both the flat-built and side-built samples have alpha grains preferably orientated in the <1 1 2¯1> and <1 1 2¯0> directions, while the preferred orientation in the top-built samples is more inclined towards the <0 0 0 1> direction, along with a significant number of grains orientated in the <1 0 1¯0> direction. The top-built sample has slightly thicker and larger α platelets than both the flat-built and side-built samples. These variations in preferred orientation and grain sizes could be mainly due to the variation of the geometry of the three samples and subsequent changes in the thermal gradient and cooling rates [41]. Since the side-built sample shares a smaller cross-sectional area with the build plate than the flat-built sample, the former has a lower cooling rate in the building direction than the latter one. Besides, the side-built sample might transport some more heat to the sounding powders because of its narrower shape than the flat-built one. This phenomenon could contribute to the larger α platelets in the side-built sample as compared to the flat-built one. Thus, the side-built sample has a wider grain diameter size distribution than the flat-built sample.

In contrast, the top-built sample, being orientated vertically along the build direction, shares a very small cross-section with the build table. It is located further away from the build table. Consequently, it has very high cooling rates in the surrounding powder environment along with the build direction, as opposed to the flat-built and side-built samples. Therefore, the top-built sample displays slightly thicker α platelets as elongated to-wards the X direction. The IPF maps taken at high magnification, as shown in Figure 20a–c, also indicate that the top-built sample has slightly larger grains, with a considerably different preferred grain orientation than the other two samples. They also reveal the elongated grain boundary, alpha colonies, and alpha basket weave platelets in various EBM-built Ti6Al4V samples. The phase maps in **Figure 25**d–f also indicate that all three samples consist mainly of α phases, with a very small fraction of β phases in between the grain boundaries. The size of the β grains is also very small compared to the α laths. The β laths are normally in the range of 50–60 nm and are typically very difficult to detect. The flat-built samples are found to have around 3.3% β phases and 96.7% α phases on the scanned area. The β phase percentages have increased to 5.1% and 9.0% for the side-built sample and top-built samples, respectively. The higher percentage of the β phase, which is comparatively softer than the α phase [53,56,114], made the top-built sample more ductile as compared with the other two samples.

Most of the grains are concentrated toward the 2 microns size in the XY plane of flat-built samples, with an average grain size of 2.8 microns (**Figure 26**). On the contrary, the XZ plane of the flat-built samples has grains well distributed around an average size of 4.1 microns. The grain boundary misorientation angles are also higher in the XY plane than in the XZ plane. The former has an average angle of 30.7 degrees, whereas the latter plane has 25.7 degrees (**Figure 27**). For the side-built samples, the grains are coarser than flat-built samples and distributed between 1–13 microns, with an average size of 5.3 µm. In contrast, the flat-built sample has a comparatively finer grain size distribution between 1–10 microns, with an average size of 4.1 µm. The top-built sample being orientated in the Z direction and possessing a very small cross-section in the XY plane (plane perpendicular to the build direction) thus displays a higher number of elongated grains in the X-direction. The distance from the build plate also plays a significant role in this regard. The top-built sample is taken from the middle of the sample, which has a significantly larger distance from the build plate. This sample has a lower thermal gradient in the build (Z) direction as opposed to the other two orientations. The overall slow cooling rate in the longitudinal direction for this sample produces very coarse grains with very different preferred grain orientations from the other two samples. The grain sizes for the top-built sample could be as large as 20 microns with an average of 6.6 µm, as can be seen in Figure 9.

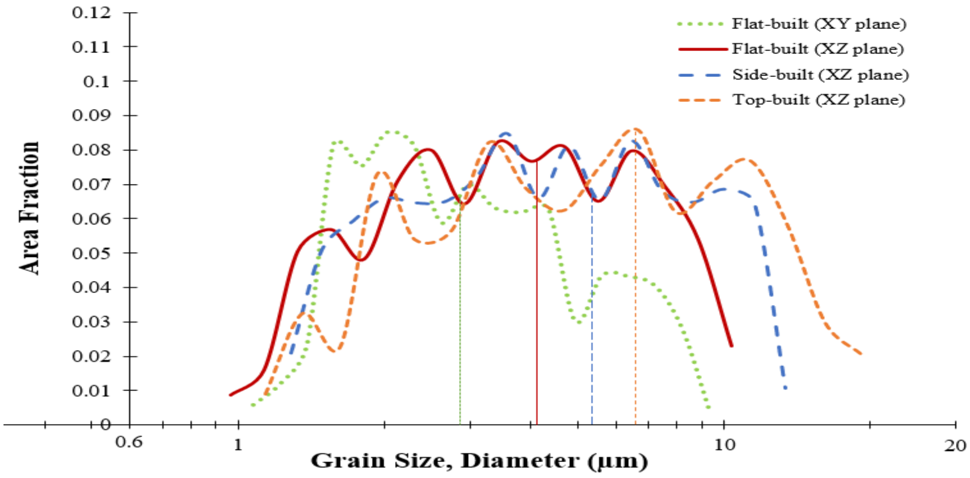

Figure 26 Grain size (diameter) distribution curves including average grain sizes of the flat-built, side-built, and top-built samples.

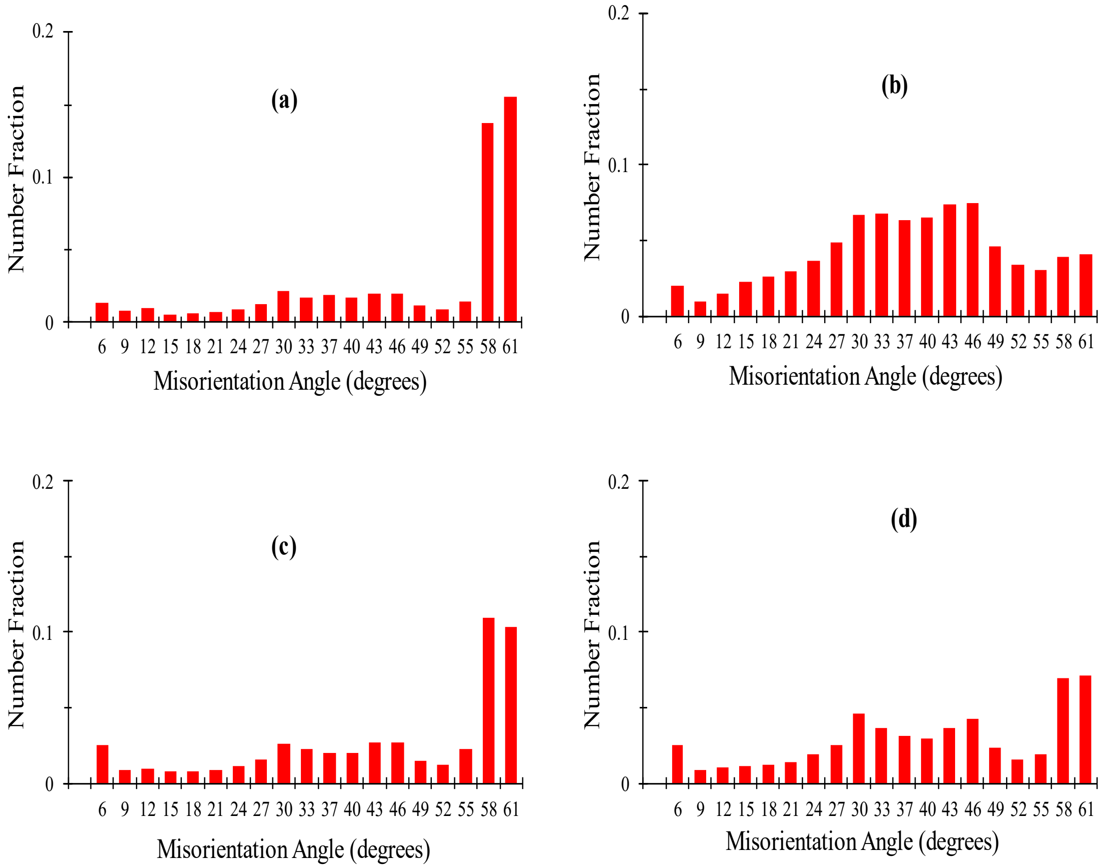

Figure 27 Misorientation angle distributions of (a) flat-built (XZ plane), (b) flat-built (XY plane), (c) side-built (XZ plane), and (d) top-built (XZ plane).

The variation in grain size and preferred orientation of the grains contributed mainly to the anisotropic mechanical behavior of the EBM-built samples. The flat-built sample displays the highest strength, modulus of elasticity, and hardness among the three orientations as a result of having the finest grain size. Conversely, the top-built samples have the lowest values of the above-mentioned properties because of their coarser grains due to slower cooling compared to the other two samples. On the contrary, the top-built sample has superior ductility to the other two samples, partly because it has a higher percentage of prior β phases (**Figure 25**) and also due to its larger grain sizes. The flat-built (XZ plane) sample has an average misorientation angle of 25.7 degrees, while the side-built (XZ plane) and top-built (XZ plane) samples have average misorientation angles of 23.2 degrees and 22.9 degrees, respectively (**Figure 27**). The higher average misorientation angle contributes to the higher dislocation defects and, eventually, higher strength and lower ductility [111]. Therefore, in the flat-built samples, the grain boundary strengthening mechanism, where the high volumetric density of the grain boundaries inhibits the dislocation movements and thus strengthens the materials [115], is stronger than the other two samples. As the average misorientation angles decrease, so do the dislocation defects, which eventually increase the ductility while losing some strength. For that reason, the top-built sample potentially exhibits the lowest strength and highest percent elongation as compared to the other two samples.

The presence of a higher fraction of β phases with a strong <001> texture direction can also be seen from the beta pole figure in **Figure 28**, and can potentially contribute to the greater ductility of the top-built sample [41,116,117]. However, the flat-built sample has the lowest maximum intensity of the beta phases, resulting in very poor ductility as opposed to the side-built and top-built samples. Similarly, the harmonic texture of the α pole figure (**Figure 28**) shows the texture intensities of the various types of α phases with different preferred grain orientations, as generated from the parent β phases [42,43]. The maximum texture intensity of the α phases is the lowest (8.99) in the flat-built sample, indicating that it has more distinct types of α phases, possessing different preferred grain orientations resulting from the primary β phases during the β→α transformation, follow-ing the Burgers relationship. The higher number of different α variants gives it more strength and hardness than the other two samples. In contrast, the maximum texture intensity of the α phases is 11.65 and 14.94 for side-built and top-built samples, respectively. The highest maximum texture intensity in top-built samples indicates a smaller number of distinct α phases, as opposed to the other two orientational samples. Consequently, the top-built sample is the weakest in terms of strength and hardness among the three samples. Therefore, the dissimilarity in microstructural grain sizes, preferred grain orientation, grain boundary misorientation angles, and harmonic texture in different EBM-built Ti6Al4V samples heavily contributed to the anisotropic mechanical behavior among the samples built in different orientations with respect to the build table.

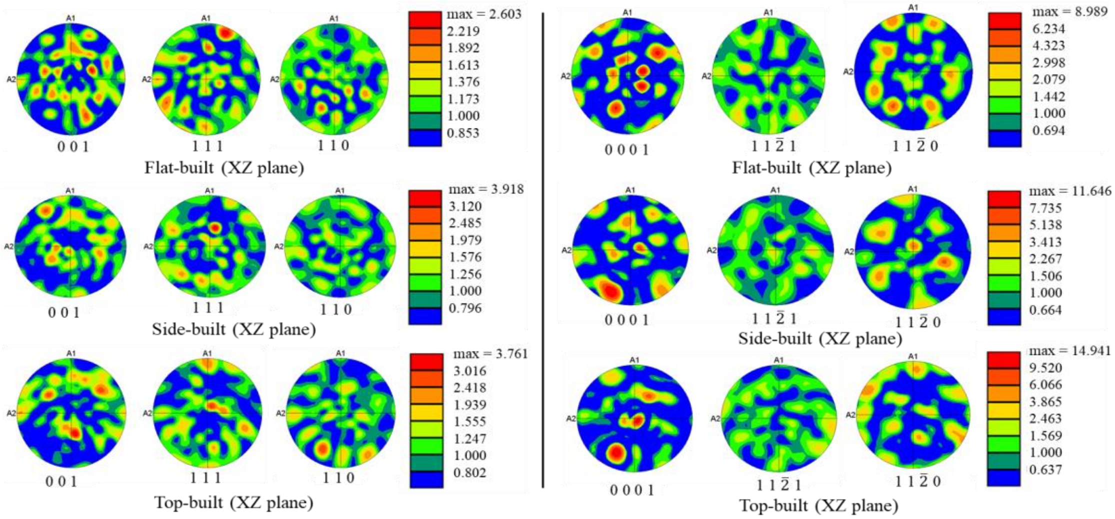

(a) Beta pole figure (harmonic texture) **(b)** Alpha pole figure (harmonic texture)

Figure 28 Harmonic texture of the three samples on XZ plane, showing maximum texture intensity (a) beta pole figure and (b) alpha pole figure

4.3.6 Evolution of Microstructure After High-Temperature Tensile Testing

4.3.6.1 High-Temperature Mechanical Softening Behaviors

The flat-built sample displayed superior mechanical behavior at both room temperature and different high temperatures than the other two build orientations in the case for all tensile properties except percent elongation. The flat-built sample showed excellent modulus of elasticity, strength, and hardness values which are comparable to the conventional wrought Ti6Al4V alloys [84,85]. On the contrary, it has a very poor percent elongation. Though both the side-built and top-built samples have outstanding percent elongation values, their other properties are either similar or considerably lower than their traditional wrought counterpart. The representative engineering stress vs. strain curves from the tensile testing of the samples from all three build orientations and different temperatures are shown in **Figure 29**. The observed anisotropic behaviors among different samples built in different orientations were found to be caused by grain growth variation [95,118]. Columnar grain growth in top build samples resulted in a much higher ductility. Higher strength in flat build samples could potentially be attributed to less number of layers, which reduces the potential for defects [95,109].

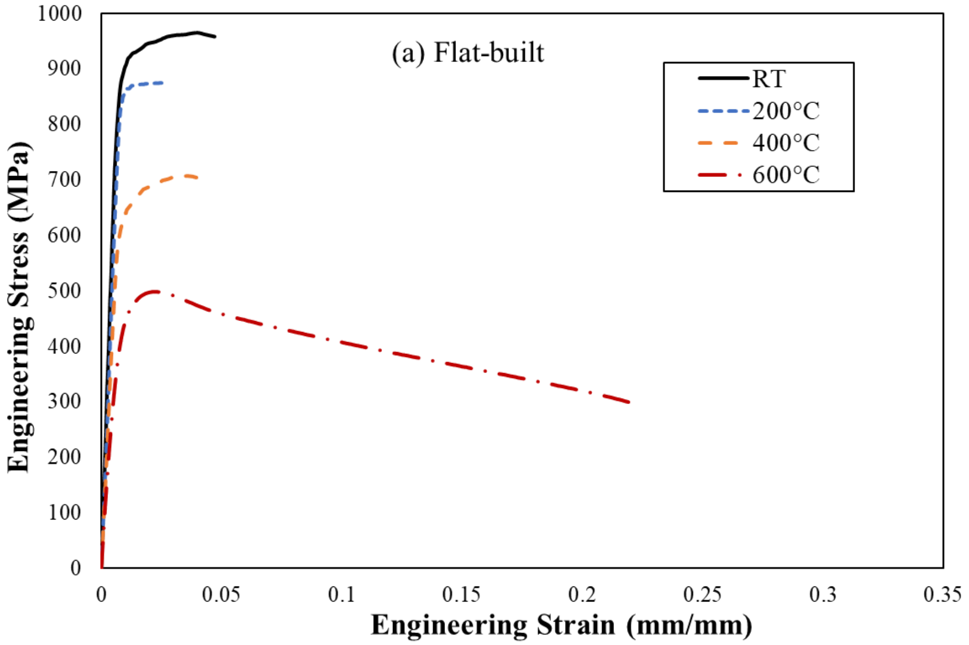
(a) Flat-built
RT
200°C
400°C
600°C
Engineering Stress (MPa)
Engineering Strain (mm/mm)
0
100
200
300
400
500
600
700
800
900
1000
0
0.05
0.1
0.15
0.2
0.25
0.3
0.35

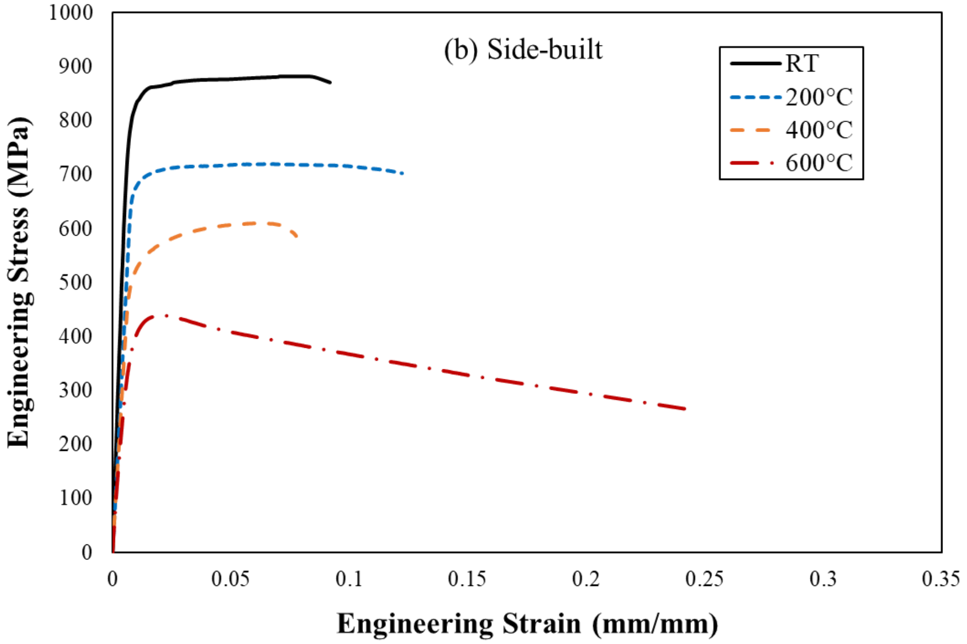
(b) Side-built
RT
200°C
400°C
600°C
Engineering Stress (MPa)
Engineering Strain (mm/mm)
0
100
200
300
400
500
600
700
800
900
1000
0
0.05
0.1
0.15
0.2
0.25
0.3
0.35

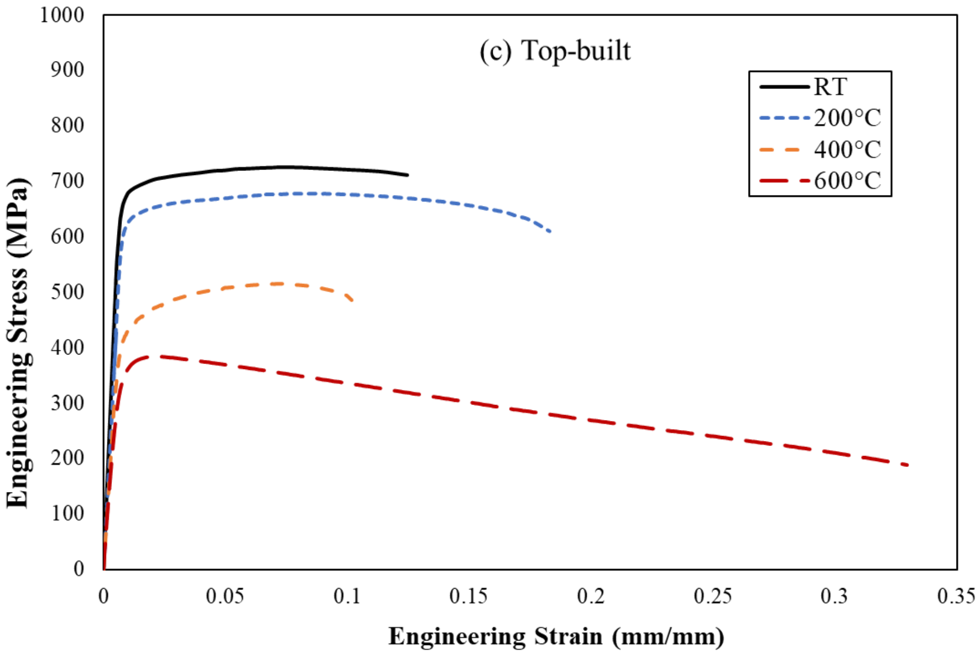

Figure 29 Engineering stress-strain curves of EBM Ti6Al4V (a) flat-built, (b) side-built, and (c) top-built samples, tested at room temperature(RT), 200°C, 400°C, and 600°C temperatures and exhibiting softening behaviors at 600°C temperature.

The variation of mechanical behaviors of EB-PBF built Ti6Al4V parts at various high temperatures has been analyzed further to understand different mechanisms which get activated at the microstructural level and affect the microstructural properties under various applied thermomechanical loading conditions. The mechanical properties of EB-PBF built Ti6Al4V parts change significantly with the increasing testing temperatures, for example, as shown in **Figure 29** for the case of all three types of samples. All the samples showed considerable temperature dependency, as can be observed from the representative engineering stress-strain curves of the top-built samples. With the increasing temperature, a significant increment of the ductility could be observed at the expense of the elastic modulus and strength properties. At 600 °C temperature, a significant decrease of flow stress and consequent softening behavior was observed at all three different orientations. It is hypothesized that this apparent softening behavior was due to various mechanisms such as the increased mobility of the inherent dislocations, which caused the dislocation density to be decreased, grain growth and coarsening, and grain boundary slip [95].

However, there was significant strain/work hardening of the EBM-built Ti6Al4V parts observed from the plastic region of the stress and strain curves obtained at room temperature, 200°C, and 400°C temperatures. The mobility of the inherent dislocations and the creation of new dislocations are normally the main reasons for the various strain hardening mechanisms that are activated during plastic deformation. Dislocation entanglements and their interaction with the barriers are the most dominant strain hardening mechanisms in the majority of the metals[100]. On the contrary, the EBM-built Ti6Al4V samples have started displaying significant softening or hot working behaviors at 600°C. Various mechanisms such as grain growth [54], change of phases, grain boundary slip, dislocation glides [105], dynamic recrystallization (DRX) [53,54], and globularization [56,61,62], coarsening, elongation, and rotation of alpha phase [60,108] are generally found to be responsible for softening of titanium alloy depending on the temperature and manufacturing processes. The phase transformation and DRX mechanisms are more prominent at α+β phase-field temperature (between 850-950 °C). Whereas both dynamic recovery (DRV) and DRX could be observed at temperatures larger than the β-transus (995 °C). In the α phase-field temperature (below 800 °C), the most pronounced softening mechanisms could be grain coarsening, elongation, and rotation, along with dislocation glide and climb.

4.3.6.2 Evolution of Microstructure with Temperature

In this analysis, various temperature-induced deformation mechanisms of EBM Ti6Al4V parts built in three different build orientations are investigated further through microstructural analysis of the samples after the tensile testing at 600°C, 400°C, and 200°C. The potential underlying mechanisms were examined thoroughly with the help of EBSD analysis. The change of microstructure and evolution of preferred grain orientation, texture, and sizes are analyzed using EBSD imaging to understand potential softening mechanisms activated during the high temperature (up to 600°C) deformation of EBM-built Ti6Al4V parts. The EBSD inverse pole figure (IPF) maps of the top-built samples after tensile testing at 200°C, 400°C, and 600°C temperatures are presented in **Figure 30**. For the top-built sample tested at 200°C, there have been significant changes in mechanical strength properties when compared with the mechanical properties of the samples tested at room temperatures. The increased dislocation mobility due to increased temperatures could be the potential reason for lower mechanical properties obtained at 200°C as compared to the room temperature properties.

The mechanical strength properties further decreased when tested at an elevated 400°C temperature. At 400 °C, there is no apparent change in the preferred grain orientations (**Figure 30**b) when compared with the IPF map of the sample tested at 200°C. For both the samples, the preferred grain orientations are <0 0 0 1> and $< 1\ 1\ \bar{2}\ 0>$ with some grains orientated at < 1 1 $\bar{2}$ 1> also. However, some amount of grain growth could be observed in the sample tested at 600°C temperature, as presented in **Figure 30**a. The average grain size increment with the increasing temperatures has been discussed further in the later discussion. Again at 600°C, most of the α grains have preferred orientations as <0 0 0 1>, < 1 1 $\bar{2}$ 0> and < 1 1 $\bar{2}$ 1>. However, the grains looked stretched out and elongated after going through the tensile testing at 600°C because of the applied thermomechanical loading. This could potentially indicate the dislocation glides and grain boundary slip. Thus, the grain growth, accelerated dislocation motion, and grain boundary slip because of the combined thermomechanical loading could be the potential softening mechanisms activated at this high temperature and thus making the material softer with lower strength and higher ductility. The unique grain color maps (**Figure 31**) of the three top-built samples tested at three different temperatures also validate the similar phenomenon described above. Substantial grain coarsening and possible grain boundary slip could be noticed from the grain color map of the top-built sample tested at 600°C temperature (**Figure 31**a).

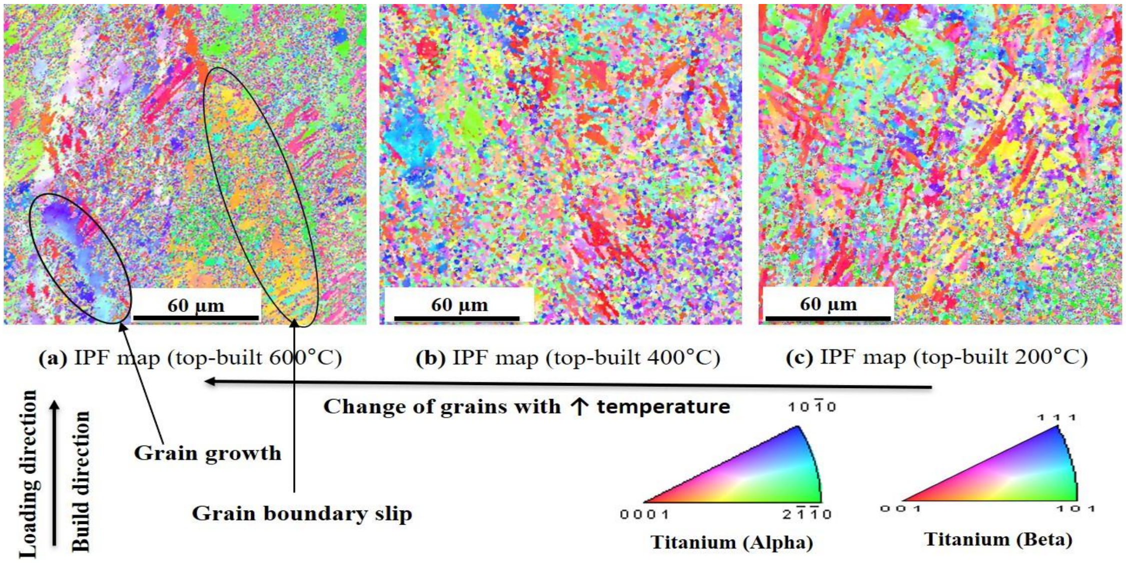

Figure 30 EBSD IPF maps of top-built samples after tensile testing at (a) 600°C, (b) 400°C, and (c) 200°C temperatures, exhibiting possible grain growth, distortion, and grain boundary slip as potential softening mechanisms.

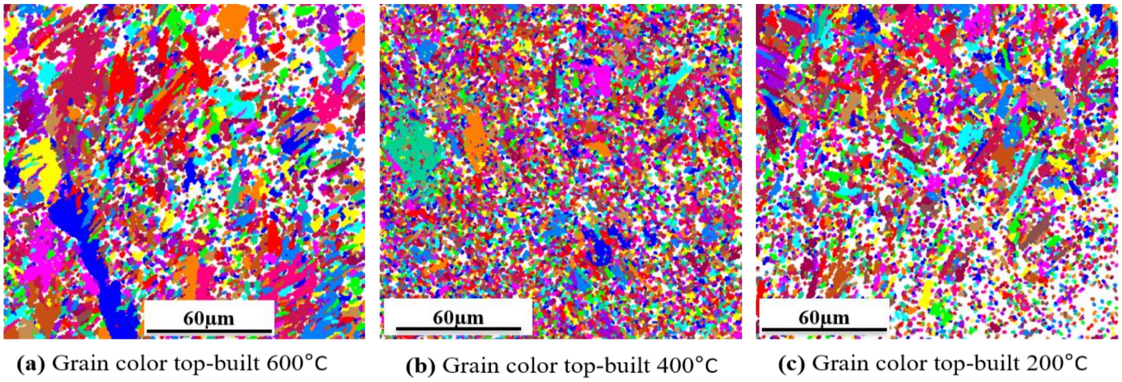

Figure 31 Unique grain color maps of top-built samples after tensile testing at (a) 600°C, (b) 400°C, and (c) 200°C temperature, further showing the change of grains with different testing temperatures as potential softening mechanisms.

The variation of grain sizes with the increasing temperatures can be further observed from the grain size distribution curves of the three top-built samples tested at three temperatures, as presented in **Figure 32**. The top-built sample tested at 200°C has an almost similar grain size distribution curve as the sample before undergoing any deformation loading. The average grain size of this sample is around 6.6 µm. A slight increase in the maximum grain size from 20 µm to 22 µm can be found mainly due to the elongation of the sample during tensile loading. The sample tested at 400°C displayed a further increase in the grain size distribution with a maximum grain of 23 µm and an average grain size of 7.1 µm. Whereas, the top-built sample tested at 600°C showed a significant shift of the grain distribution curve to the right, reaching a maximum grain size of 32 µm and an average grain size of 8.8 µm. These further indicate the grain growth and coarsening as viable softening mechanisms activated at this elevated temperature.

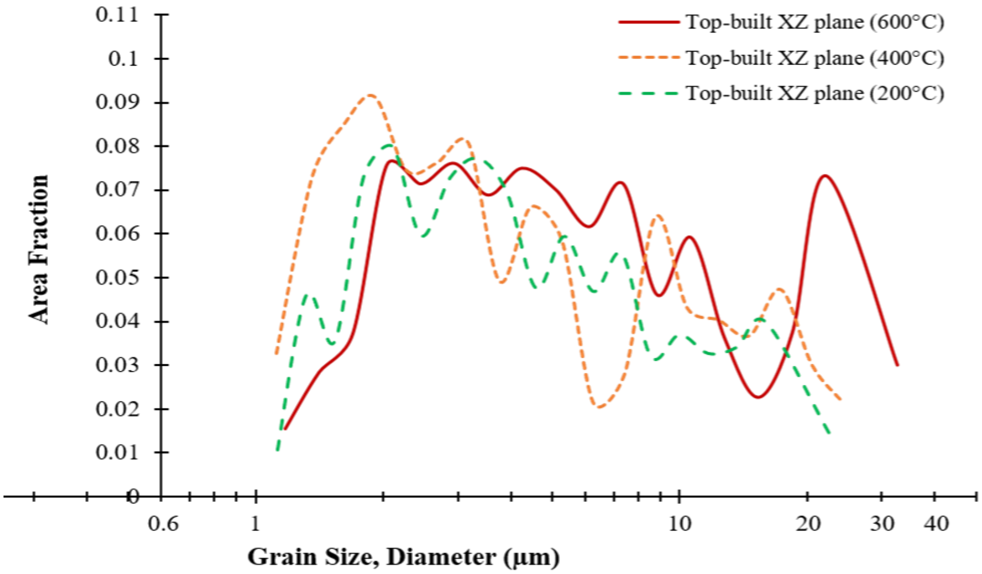

Figure 32 Grain size distributions of top-built samples at XZ plane after tensile testing at 200°C, 400°C, and 600°C temperature, respectively, showing the evolution of grain sizes and grain growth with an increment of testing temperatures.

The misorientation angle distributions of the top-built samples after tensile loading at 200°C, 400°C, and 600°C are compared and presented in **Figure 33**. The average of misorientation angles decreases from 22 degrees to 20.5 degrees and 19 degrees with increasing temperatures from 200°C to 400°C and 600°C, respectively. The number fractions of both low angle grain boundaries (LAGBs, <15°) and high angle grain boundaries (HAGBs, >15°) decreases with increasing temperatures, except at angles higher than 55°. This variation of misorientation angle also indicates the potential grain boundary slip and increased dislocation motion, affecting the mechanical properties of the Ti6Al4V parts with increasing temperature [119,120].

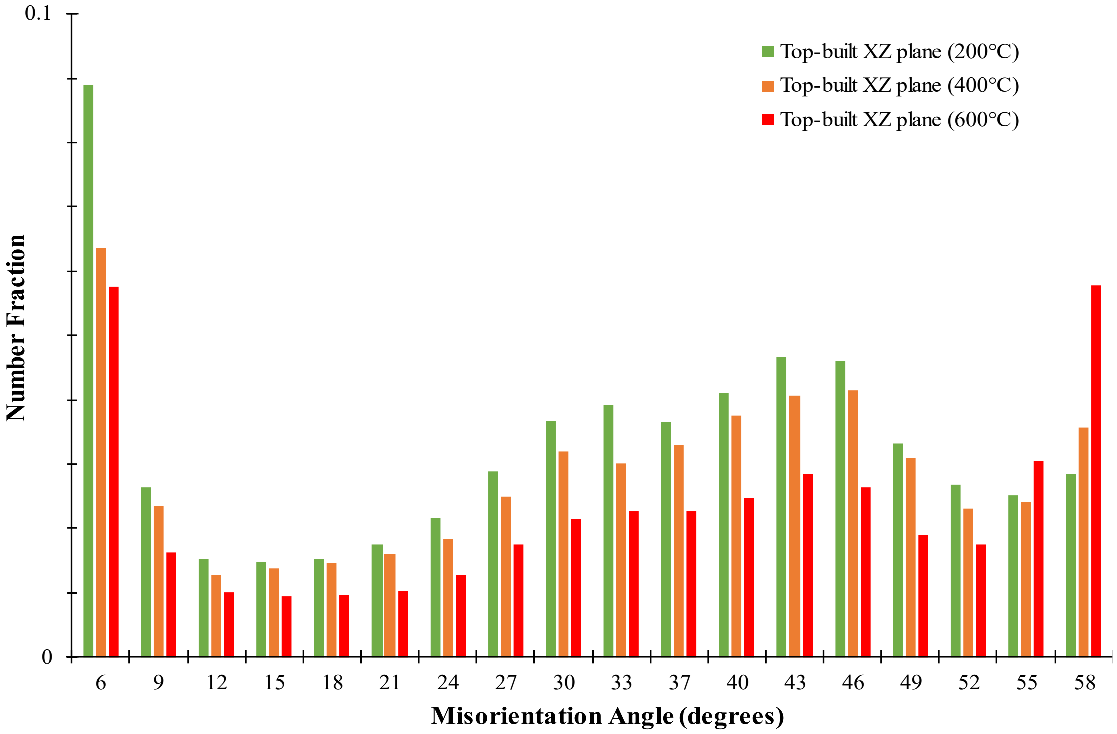

Figure 33 Misorientation angle distributions of top-built samples at XZ plane after tensile testing at 200°C, 400°C, and 600°C temperatures, respectively, showing a decrease of the fraction of LAGBS and fraction of HAGBs with increasing temperature.

The evolution of the texture of the grains of the top-built Ti6Al4V samples after tensile testing at 200°C, 400°C, and 600°C are presented via both alpha and beta pole figures as presented in **Figure 34**. The maximum intensity of harmonic texture of the beta pole figures decreases from 6.27 to 2.79 with increasing temperatures from 200°C to 600°C. Whereas the maximum intensity of the harmonic texture of the alpha pole figures increases from 7.04 to 12.32 with increasing temperature from 200°C to 600°C. This also possibly indicates the change of grain sizes and grain boundary distortion with the applied thermomechanical loading [119]. The intensities of the different preferred grain orientations which are <0001>, < 1 1 $\bar{2}$ 0> and < 1 1 $\bar{2}$ 1> changed considerably following the tensile testing at different temperatures, as visible from the α pole figure harmonic texture maps in **Figure 34**a. Therefore, the grain boundary distortion could be another softening mechanism activated during high-temperature deformation.

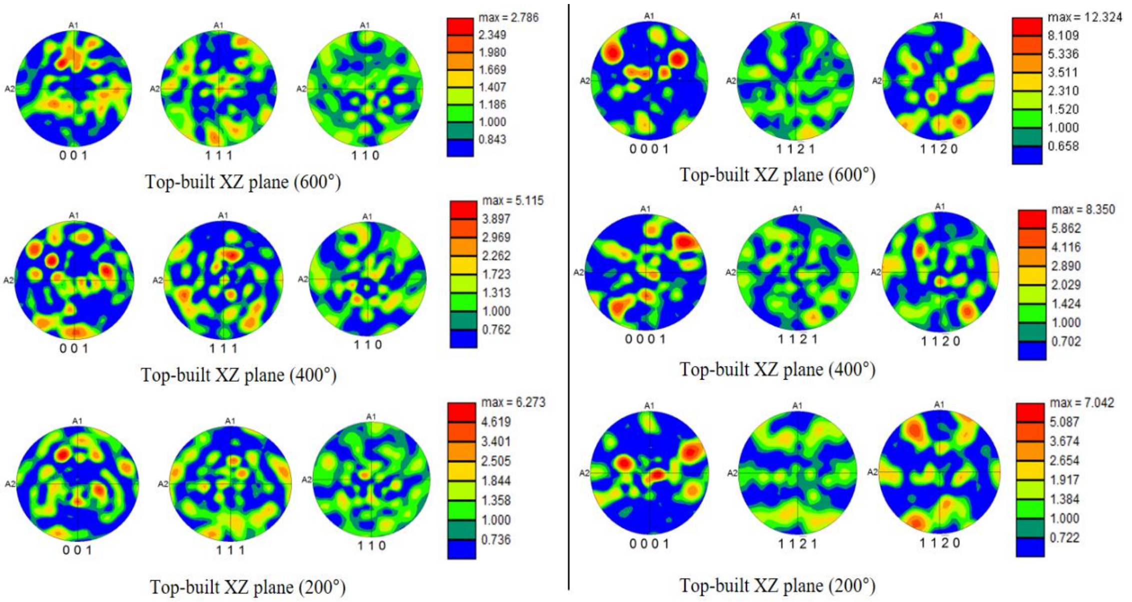

(a) Beta pole figure (harmonic texture) **(b)** Alpha pole figure (harmonic texture)

Figure 34 Harmonic texture of (a) beta pole figure and (b) alpha pole figure of the top-built samples on XZ plane, after tensile testing at 600°C, 400°C, and 200°C temperature, respectively. The maximum texture intensity of beta is decreasing, and alpha increases with increasing temperature.

Similarly, the side-built EBM Ti6Al4V samples also exhibit the evolution of the grain size, texture, and phases with the increment of tensile testing temperature. The EBSD IPF maps of the three side-built samples after tensile testing at 200°C, 400°C, and 600°C temperature, as presented in **Figure 35**, clearly show the change of microstructural features with increasing temperature. The grain growth and distortion of the alpha grain boundary could be observed as the temperature increases from 200°C to 600°C. On the contrary, the change of size and orientation of beta grains are very difficult to be noticed since they are extremely small in size as compared to the alpha grains and located at the grain boundaries of the alpha phases [40]. Therefore, elongated and larger alpha grains could be noticed for the side-built Ti6Al4V sample after deformation at 600°C (**Figure 35**a), indicating potential softening mechanisms. Again, the orientation of the alpha grains does not exhibit much change from the preferred ones of $<0\ 0\ 0\ 1>$, $<1\ 1\ \bar{2}\ 0>$ and $<1\ 1\ \bar{2}\ 1>$ orientations after going through the thermomechanical loading at 200°C, 400°C, and 600°C temperatures, respectively. Again, the distribution of grain sizes of the side-built samples tested at the three temperatures is presented in **Figure 35**d. The grain size distribution curves of the samples tested at 200°C and 400°C have a slight difference. The former has a maximum grain size of 14 µm and an average grain size of 5.3 µm. At 400°C, the side-built Ti6Al4V sample has a maximum grain size of 16 µm and an average grain size of 6.2 µm. While the side-built sample tested at 600°C has a noticeable difference in grain distribution curve when compared with the curves of the former two samples. The sample, after going through deformation at 600°C, acquire elongated and coarser grains as large as 21 µm in diameter and with an average size of around 7.8 µm. The fraction of alpha and beta phases of any of these samples didn’t change much after tensile testing at these three different temperatures. The microstructures of the EBM-built Ti6Al4V samples are observed to consist of more than 90% of alpha phase and less than 10% of beta phase at the alpha grain boundaries. There was no significant α→β phase transformation found to have occurred since the highest deformation temperature of 600°C was well below the α+β phase-field temperature of 850-950 °C.

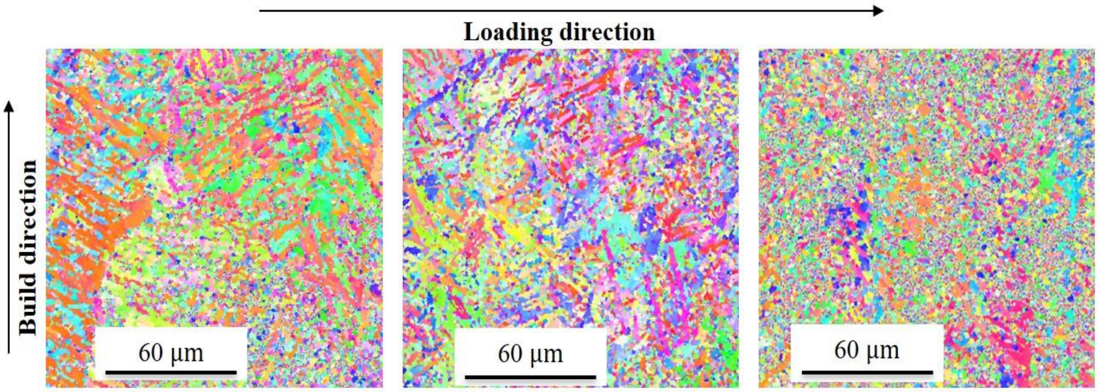

(a) IPF map (side-built 600°C) **(b)** IPF map (side-built 400°C) **(c)** IPF map (side-built 200°C)

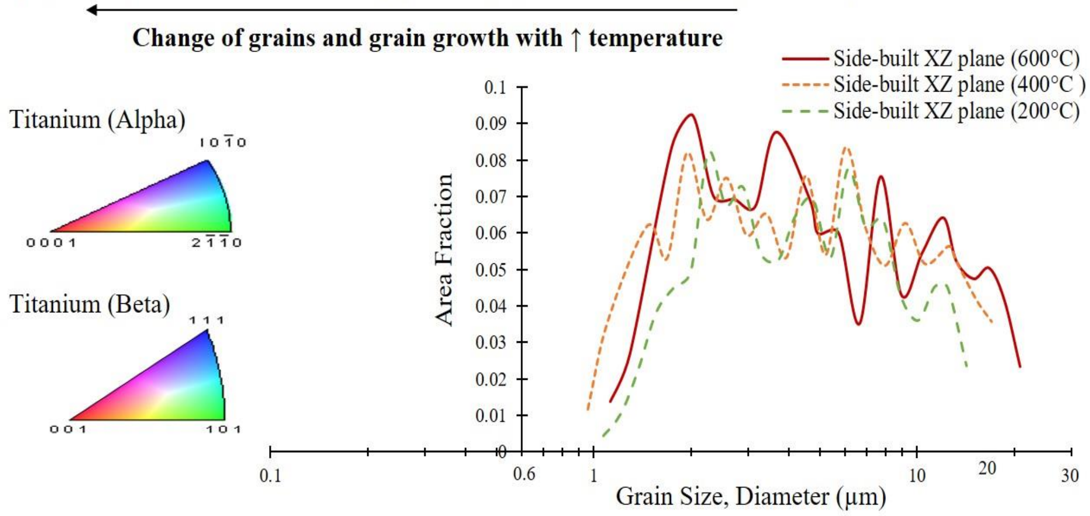

(d) Grain size distributions

Figure 35 EBSD IPF maps of the side-built samples after tensile testing at (a) 600°C, (b) 400°C, and (c) 200°C temperatures, exhibiting a change of grains, grain growth, distortion, and grain boundary slip as potential softening mechanisms. (d) grain size distribution graphs show the evolution of grain sizes and grain growth with an increment of testing temperatures.

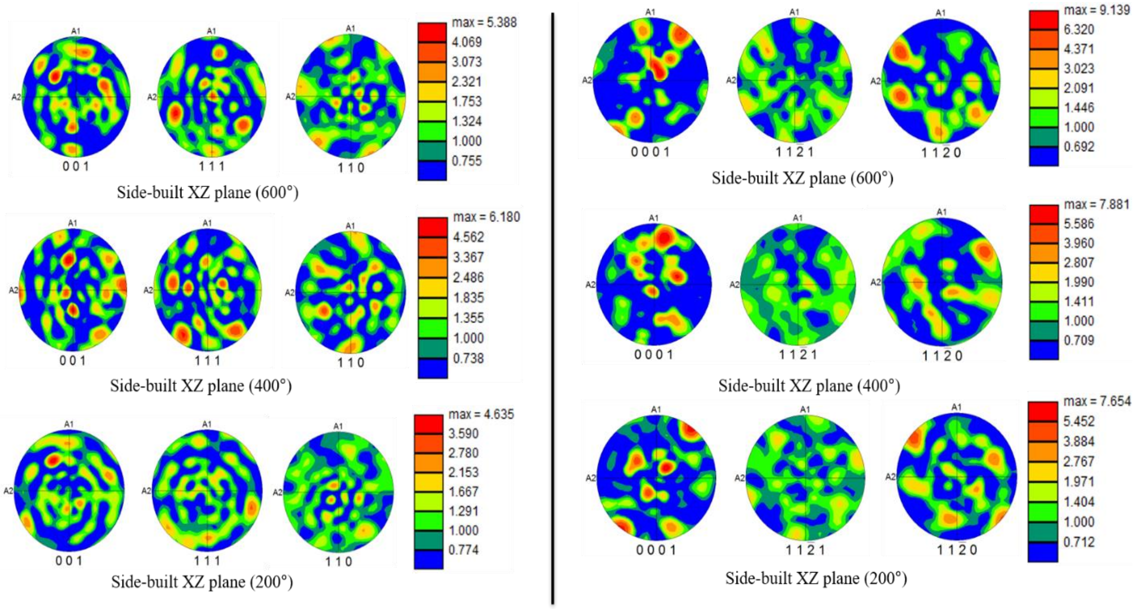

(a) Beta pole figure (harmonic texture)

(b) Alpha pole figure (harmonic texture)

Figure 36 Harmonic texture of (a) beta pole figure and (b) alpha pole figure of the side-built samples on XZ plane, after tensile testing at 600°C, 400°C, and 200°C temperature, respectively. The maximum texture intensity of beta decreased from 400°C to 600°C, and the maximum intensity of alpha increased with increasing temperature.

However, the intensity of the grain texture changes with the testing condition, as can be seen from the alpha and beta pole figures in **Figure 36**. The maximum intensity of the alpha pole figure increases with increasing temperature, and in the case of the beta pole figure, it increases from 200°C to 400°C and again decreases at 600°C temperature. Besides, the overall aspect ratio of the α lath also changes with the testing temperature. Similarly, the flat-built sample should undergo similar softening mechanisms as observed in the side-built and top-built samples at elevated temperatures. To avoid overemphasis, the flat-built samples were not analyzed further. Therefore, grain coarsening, elongation, grain boundary slip, and temperature-induced accelerated dislocation motions are the possible softening mechanisms activated at 600°C, making the flow stress properties, and mechanical strength properties of the EBM-built samples lower as compared to their room temperature relevant mechanical properties.

4.4 Surface Profile Measurement of As-Built Ti6Al4V Components, Produced Using EB-PBF AM Technology

4.4.1 Experimental Procedures

The surface topography of the as-built Ti-6Al-4V parts fabricated using EBM technology with three different build orientations has been analyzed for potential anisotropy in surface roughness. With advances made in different areas of surface topography, a variety of surface characterization technologies such as contact stylus, coherence scanning interferometry, atomic force microscopy (AFM), optical microscopy, scanning electron microscopy (SEM), and x-ray computed tomography are available for measuring surface texture of additively manufactured metal parts [121]. Among these, the stylus profilometer and coherence scanning interferometry or 3D optical profilometer are widely used for measuring various surface defects [122–125]. In this analysis, the surface texture and roughness of different surfaces, which are parallel to the loading direction, were measured using a stylus profiler from each of the samples built in different orientations. Significant variations in surface finishes and roughness parameters were found on these samples with different build orientations. Surfaces perpendicular and parallel to the build direction have also been examined using a digital optical microscope to see how they differ from each other. Furthermore, fracture surfaces obtained from the tensile test were analyzed using field emission secondary electron microscopy (FESEM) to observe the crack initiation and propagation sites.

4.4.1.1 Surface Profile Measurements

All the surface measurements were taken parallel to the loading direction to get all the surface roughness defects perpendicular to the loading direction. Because surface roughness defects parallel to the loading direction might not have any significant effect as compared to defects perpendicular to the loading direction as potential fatigue crack initiation and propagation site. Surface profile measurements were taken from multiple locations of the surface areas to calculate the average values of various surface parameters. For all the samples, surfaces, both parallel and perpendicular to the build direction, have been analyzed to determine the roughest surface among them for each orientation. Furthermore, the three most rough surfaces from the three samples have been analyzed further to determine the roughness anisotropy with print orientation and to predict the fatigue strength.

The surface profiles of the EBM Ti6Al4V samples were measured using a profilometer named Ambios XP-200 stylus profiler, as shown in **Figure 37**. This stylus profilometer had a stylus tip radius of 2.5 µm, scan length range of 50 mm, and vertical measurement range of 800 µm [126]. The scan length of 5 mm and a scan speed of 0.03 mm/sec were used to get the surface profile of the sample using this profiler. Measurements were taken parallel to the loading direction to capture the surface defects perpendicular to it since these defects are most likely to open under cyclic loading and contribute to the fatigue crack initiation and propagation. Further details can be found elsewhere [109].

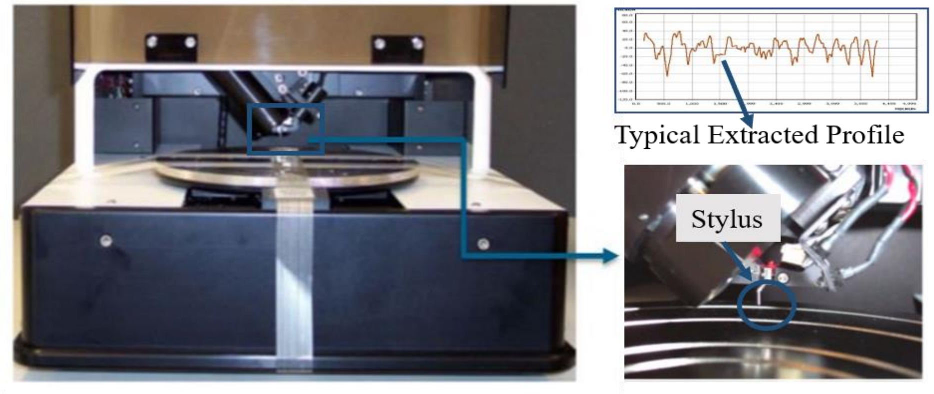

Figure 37 Surface profile measurement tool named Ambios XP-200 stylus profiler.

Furthermore, various surface parameters were calculated from the surface profile extracted using this instrument. Some of these parameters are average roughness (R_a), root mean square roughness (R_q), peak height (R_p), valley height (R_v), and total height ($R_t = R_p + R_v$) of the profile, as shown in **Figure 38**. The average roughness, R_a can be calculated by using the equation as shown below [127],

$$R_a = \frac{1}{L}\int_0^L |r(x)|dx \qquad 5$$

Here, L is the evaluation length, and r(x) is the profile height from the mean line. Again, the root mean square roughness (R_q) is defined as follows,

$$R_q = \sqrt{\frac{1}{L}\int_0^L \{r(x)\}^2 dx} \qquad 6$$

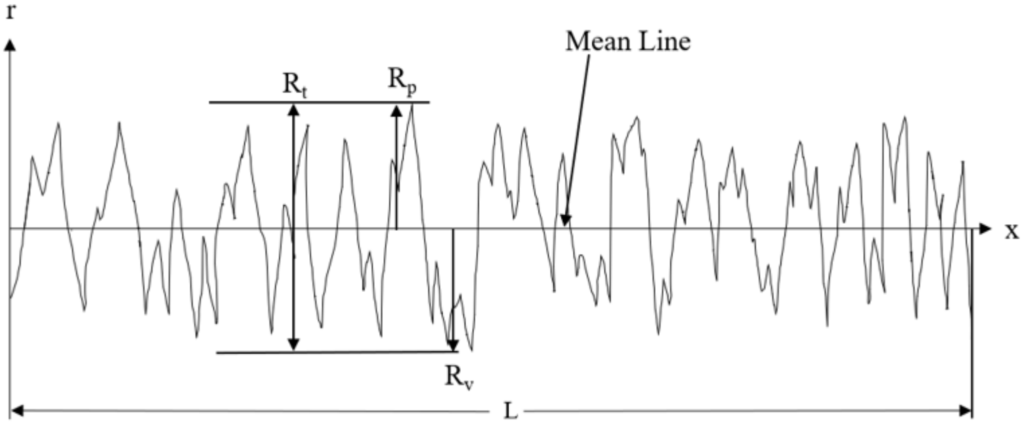

Figure 38 Definition of various surface roughness parameters.

4.4.1.2 Variation of Surface Profile and Roughness

From the surface measurements of EBM Ti6Al4V parts, it was observed that for the top-built sample, all four surfaces parallel to the loading direction are equally rough because in these surfaces, the layers are stacked in the same manner. On the contrary, for flat-built and side-built samples, all four surfaces are not equally rough. Two of the four parallel surfaces are comparatively smoother than the other two. The surfaces parallel to the build direction are rougher as compared to the surfaces perpendicular to the build direction. The comparison of the surface profiles, along with surface roughness parameters measured from them, of the two surfaces of the flat-built sample is presented in **Figure 39**. Here, the surface parallel to the building direction has superior values for all the examined parameters than the surface perpendicular to the building direction. For example, the average roughness, R_a value for the parallel surface, is 2.6 times larger than the perpendicular surface. The standard deviations of all the parameters are also greater on the former surface. The reason behind these higher irregularities of parallel surface is the presence of multiple layers on it, as opposed to a single layer on the perpendicular surface. Consequently, one of the parallel surfaces from each orientation was selected for further analysis because fatigue cracks are most likely to initiate from these rougher surfaces under dynamic loading.

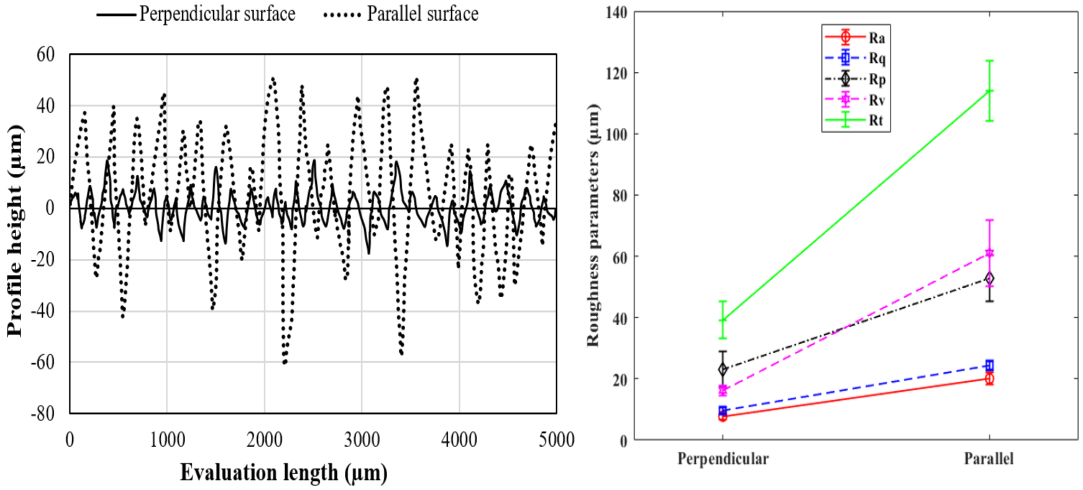

(a) (b)

Figure 39 Comparison of (a) surface profiles and (b) various surface roughness parameters obtained from these profiles of the two surfaces (perpendicular and parallel to the build direction) of the flat-built sample measured along the loading direction.

The variation in surface measurement data of EBM Ti6Al4V parts, taken using the stylus profiler from the roughest surface of the three samples, with build orientation, is presented in **Figure 40**. While the side-built sample has slightly higher average roughness (R_a) and root mean square roughness (R_q) values than the flat-built sample, these values are significantly higher in the top-built sample as compared to both of them (**Figure 40**a). For instance, the R_a and R_q values are around 25 % and 27 % larger, respectively, in the top-built sample than in the flat-built sample. All the other roughness parameters, which are peak height (R_p), valley height (R_v), and total height (R_t), also display a similar trend with build orientation. Though the flat-built and side-build samples have similar values for all these three parameters, the top-built sample has considerably greater values than the other two (**Figure 40**b). It can also be noticed that among R_p and R_v, the latter has a stepper gradient between side-built and top-built samples. Consequently, the gradient of R_t is also steep between them since it is simply the summation of the peak and valley heights. The larger valley height could potentially lead to lower fatigue life for the top-built sample.

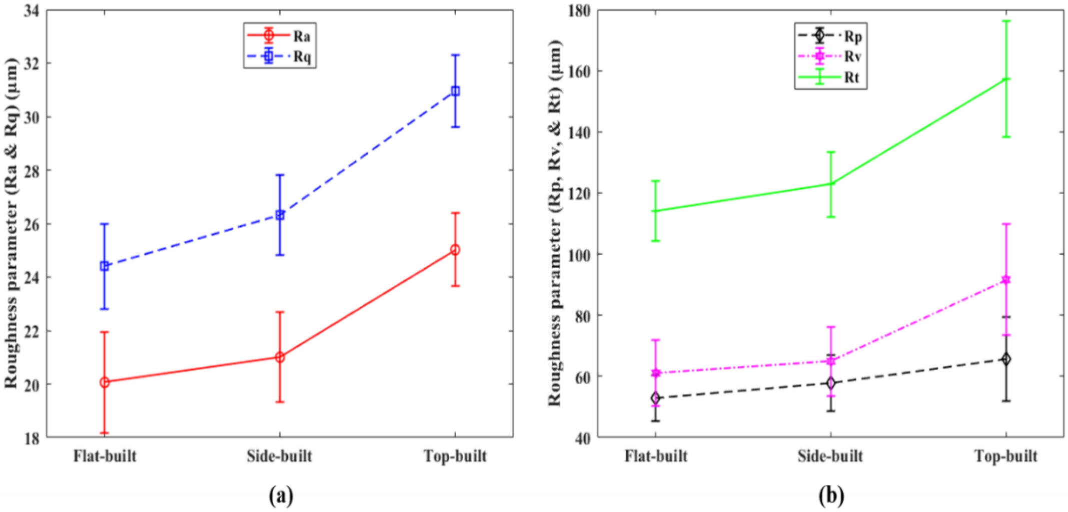

Figure 40 The variation of surface roughness parameter (a) Ra & Rq, and (b) Rp, Rv, & Rt values with the build orientation obtained from the roughest surfaces of as-built EBM Ti6Al4V samples.

However, a significant amount of variation in the surface roughness parameters, measured on different surfaces of the samples of different build orientations, could be noticed for the EBM process due to the changes in layer deposition directions and layer numbers in different build orientations. The top-built sample has quite a large number of layers stacked together along the longitudinal directions, and measurements are taken across the layers, while for flat-built and side-built samples, the measurements are along with the layers. Hence, the flat-built and side-built samples show almost similar surface irregularities, which are better than the top-built sample. On the contrary, the top-built sample displays the roughest surface among the three orientations. Besides, roughness parameters also vary among different surfaces of a particular orientation. Furthermore, since there is a close correlation between the fatigue properties and the surface defects [128,129], the fatigue performance of flat-built and side-built samples could be better than the top-built sample. Later in this study, the surface profiles, obtained using the stylus profiler, were used to predict the fatigue strengths of EBM Ti6Al4V parts built in three different orientations, using two predictive models as discussed in the following sections.

4.5 Optical and Secondary Electron Microscopy Analysis

A digital microscope named Hirox KH-7700 was used to observe the surfaces perpendicular and parallel to the build direction. The flat-built sample with the top surface perpendicular to the build direction is shown in **Figure 41**a. The red box indicates the place from where the image was taken at ×350 magnification of the lens. The captured image from this surface shows grooves along the width direction, as indicated in **Figure 41**b and **Figure 41**c. These grooves indicate that during this E-beam melting process, the scanning pattern at the top layer could be along the width direction. Conversely, the side-built sample with a top surface parallel to the build direction is presented in **Figure 42**a. An optical microscopy image was taken at ×700 magnification, as presented in **Figure 42**b, revealing round shape melt pools which are responsible for the higher roughness on this surface. 3D image in the wireframe form also verifies that the surface irregularities in this surface are in random round melt pool shape, as shown in **Figure 42**c, as opposed to the groove shape in a surface perpendicular to the build direction. From these optical images, it is also noticeable that the surface perpendicular to the build direction is smoother than the parallel surface.

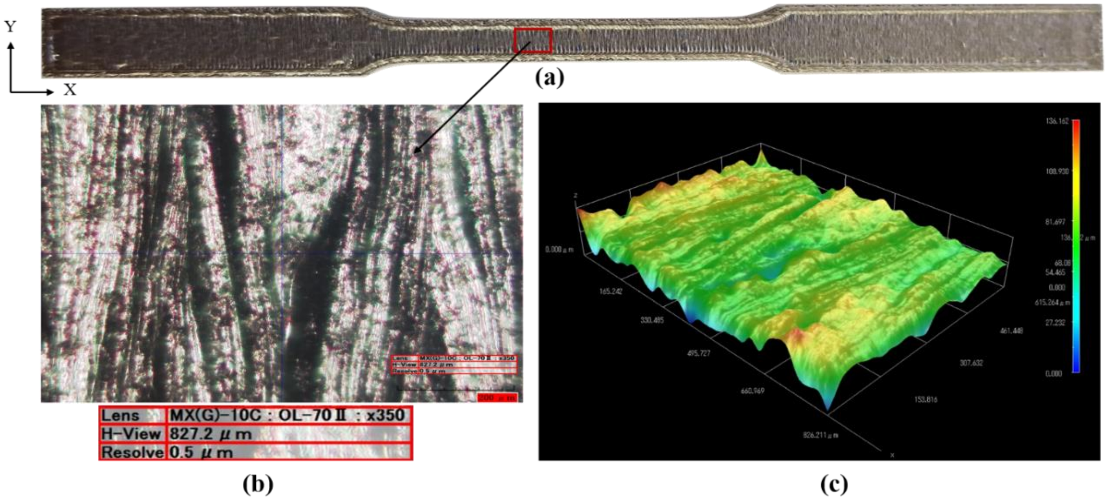

Figure 41 The top surface (perpendicular to the build direction) of the flat-built sample (a), with 2D (b) and 3D (c) optical microscope images.

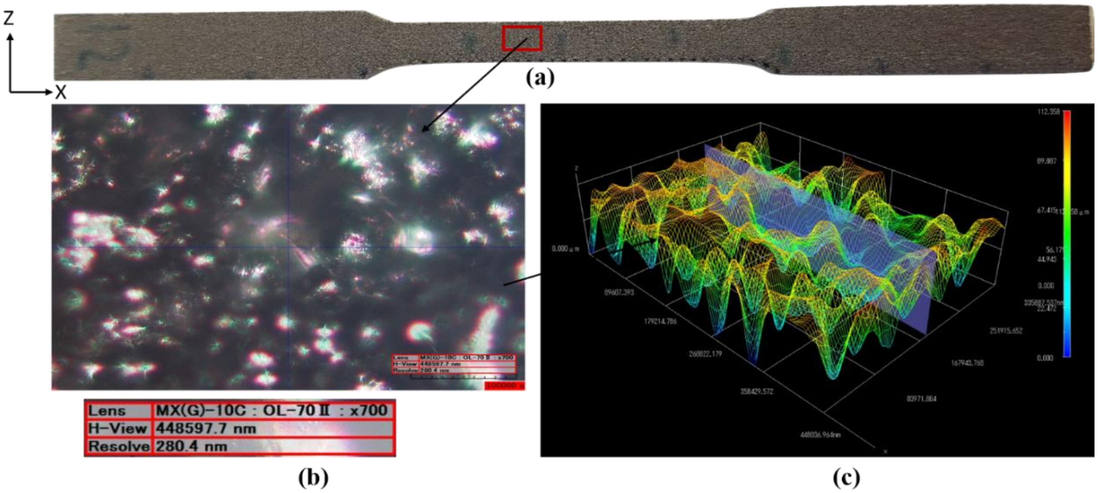

Figure 42 The top surface (parallel to the build direction) of the side-built sample (a), with 2D (b) and 3D (c) optical microscope images.

Furthermore, the fracture surfaces obtained from tensile testing of the as-built Ti-6Al-4V samples from the three build orientations confirm that there are unmelted or partially melted powder particles near the surface or sub-surface areas, as can be seen in **Figure 43**. Generally, these kinds of defects are primarily responsible for fatigue crack initiation and propagation under cyclic loading as well. Since the top-built sample has a large number of layers and most of the heat produced during the melting process transfers along the longitudinal direction, there are a significant amount of unmelted or partially sintered powder particles attached to the four parallel surfaces. As a consequence, it has very rough surfaces, as can be observed in **Figure 43**c. On the contrary, in the flat-built and side-built samples, there is a lower number of layers than in the top-built sample, and the heat transfers across the thickness and width directions, respectively. Therefore, the amount of partially sintered particles should be less in these two orientations than in the former one.

The flat-built sample (**Figure 43**a) has a better surface finish than the top-built sample (**Figure 43**b), whereas the side-built sample has a large amount of unmelted powder particle zone (**Figure 43**c) near the surface. Since the top-built sample has higher surface roughness, as calculated in the previous section, than the other two orientations, its fatigue performance might be lower than the other two.

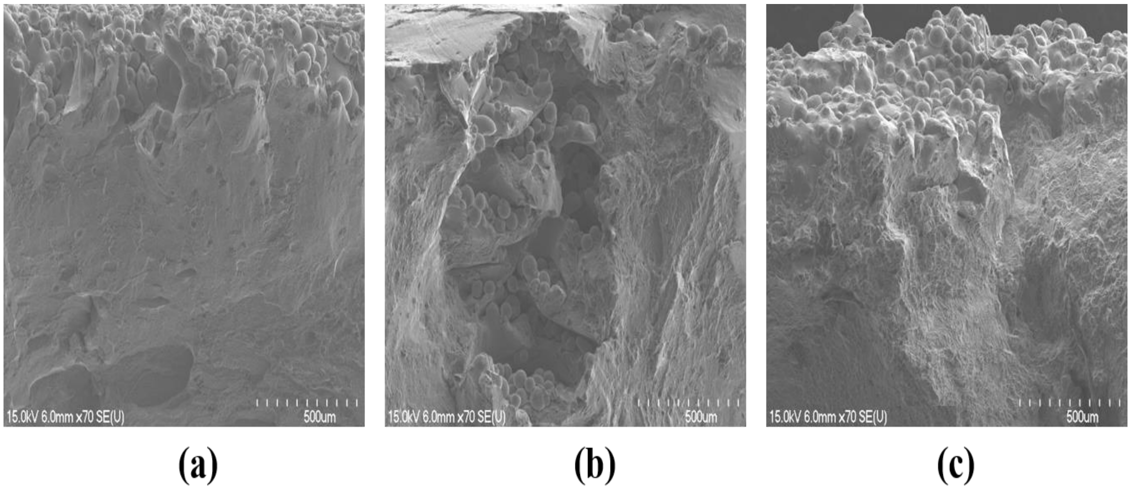

Figure 43 Secondary electron microscopy (SEM) images of the fracture surfaces of (a) flat-built, (b) side-built, and (c) top-built EBM Ti-6Al-4V samples.

4.6 Mechanical Hardness Measurements

The hardness of the specimens was measured using an ACCO WILSON Rockwell hardness tester (Acco-Wilson, Inc., Santa Cruz, CA, USA). A sphero-conical diamond indenter was used for the indentation. The preliminary force that was applied initially was 10 kgf. Finally, a total force of 150 kgf was applied for the hardness measurement. In total, six measurements were taken from the mid-gauge section of each sample. Then, the mean value of all the hardness measurements was calculated to minimize the error pertaining to them. The standard hardness conversion chart, provided by the instrument manufacturer, was used for calculating the Vickers hardness (HV) of all the samples. Furthermore, an MTS Criterion® Electromechanical Universal Test System was used to measure the ultimate tensile strength (UTS) of all the samples. The average value of UTS was calculated from the three measurements at each orientation of the samples. All the measured mechanical properties of all three EBM Ti6Al4V samples are presented in **Table 8**. The flat-built sample showed superior strength and hardness to the other two orientations. Whereas the top-built sample has the lowest strength and hardness values.

These anisotropic behaviors are believed to be due to the microstructural variation resulting from the different thermal histories of the three samples. Since in the top-built sample, the scan length is very short compared to the other two orientations, the cross-section area is also significantly small for this orientation. Therefore, the heat buildup in the top-built sample is quite high, which results in the melting of adjacent points in quick succession, unlike the flat-built and side-built samples. Besides, the cross-section area in contact with the build plate is largest in flat-built, accelerating the escape of heat, followed by side-built, while the top built has the least contact area. The above-mentioned phenomena, in combination, result in microstructural and defect formation variations and the subsequent differences in measured hardness and strength. Further analysis on these anisotropic behaviors of EBM Ti6Al4V samples and their possible reasons could be found elsewhere [130],[45]. The obtained Vickers hardness (HV) values along with surface profile measurement data, were used for the fatigue strength prediction of as-built EBM Ti6Al4V samples, as discussed in the following section.

Table 8 Mechanical properties of EBM built Ti6Al4V specimens built in three orientations.

Specimens	Vickers hardness, HV (kgf/mm^2)	Ultimate tensile strength, UTS (MPa)
Flat-built	345	1065
Side-built	318	881
Top-built	294	807

4.7 Analysis of Porosity and Internal Defects Using 3D X-ray Computed Tomography

4.7.1 3D X-ray Computed Tomography (CT) Principles

X-ray computed tomography (CT) has become a popular tool for nondestructive analysis of the internal structure and defects in three dimensions of different metal components in various industries, including aerospace, automobile, and medical field. It can provide information up to tens of nanometer scales. It uses powerful X-rays which penetrate through an object and create two-dimensional images from different directions. These 2D images are then stacked together using a computed reconstruction algorithm to create a digital 3D greyscale representation of the internal structure and defects of any object. [131].

The reconstructed 3D volume can be visualized in various ways, such as slice by slice, which is also called virtual cross-sectioning, or by rendering the 3D view of the internal features of the object. The datasets collected through this technique can be visualized and analyzed using various software such as VGStudio, Avizo, Max, and other software packages [132].

The intensity and phase of the electromagnetic X-ray wave change when it passes through an object depending on the refractive index of that object. The refractive index, n can be expressed by the following equation,

$$n = 1 - \delta + i\beta \tag{7}$$

Where β provides the attenuation or absorption contrast, and δ provides the phase shift information as the X-rays pass through the object. The attenuation of the X-rays can be found from the linear attenuation coefficient, μ, as given by $4\pi\beta/\lambda$, where λ is the wavelength of the X-ray. [133].

The 3D images are made of numerous cubic volumes, which are called voxels, similarly as the 2D images are made of 2D pixels. The spatial resolution is normally larger than the voxel size, depending on other scanning parameters. Therefore, the voxel size must be sufficiently smaller than the size of the anticipated defects or features to capture them appropriately [134]. Conventional medical or industrial CT possesses sub-millimeter resolutions (voxel sizes ≥100 μm), whereas micro-tomography (micro-CT) has micrometer resolutions (voxel sizes ≥ 0.1 μm) and nano-tomography (nano CT) has nanometer resolutions (voxel sizes ≥ 10 nm). Though a smaller feature size can be recorded by selecting a smaller voxel size, the field of view (FoV) on the detector will be smaller as well, along with the requirement of larger computation reconstruction time and space. Higher effective resolution can be obtained by moving the object away from the detector, thus geometrically magnifying the X-ray image on the detector (**Figure 44**). Thus, the geometric magnification, M, is the ratio between the X-ray source to detector distance and the X-ray source to object distance [134].

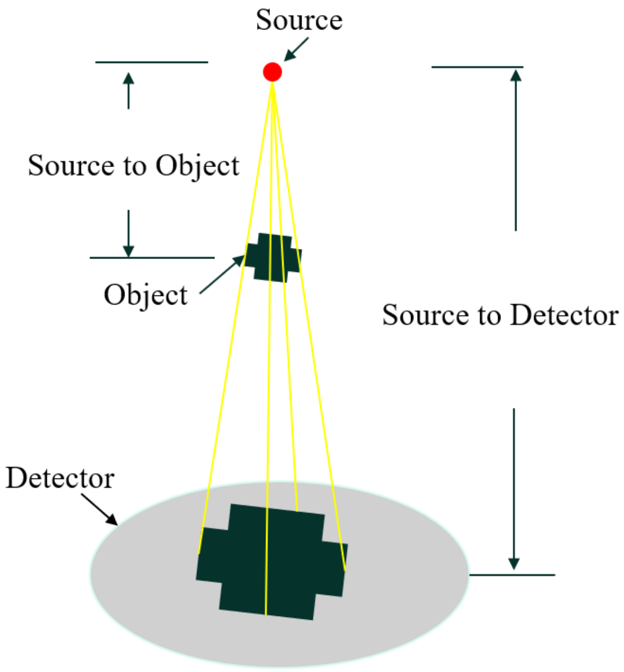

Figure 44 Geometric magnification of X-ray computed tomography (CT) scanning

4.7.2 Experimental Procedures

The porosity and internal defects of the as-built EBM Ti6Al4V samples from the three build orientations have been analyzed using an X-ray computed tomography(CT) modeled as Phoenix S240. The software used for data acquisition and analysis of the samples is Datos ACQ 2.8.2 and Datos REC 2.8.2, respectively. For getting higher resolution, a nanofocus tube was utilized with a tube voltage and current of 160 kV and 250 µA, respectively. Hence, the target power was 40 W. No. of images/ total scan time was 1000/33 min. A voxel size of 10 µm was used for capturing small-scale defects with a diameter of 10 microns or larger. The effect of the internal and external defects on the fatigue performance of the EBM Ti6Al4V parts has been analyzed and can be found elsewhere [109].

4.7.3 Results and Discussion

For the porosity measurements, a scanning volume of 332 mm3 to 393.54 mm3 was selected from the gauge section of the three types of samples. The flat-built sample revealed a very high porosity of 0.17%, whereas both the side-built and top-built samples demonstrated a similar porosity value of around 0.05%. The high porosity and lack-of-fusion (LOF) defects normally result from the insufficient melting of powder particles in between the subsequent layers due to the deviation of the processing parameters from the desired ones caused by changes in either the power source or scanning system operation [67]. The scanning cross-section area being larger in the flat-built sample results in higher chances of accumulating LOF defects than in the other two samples. The various porosity and internal defects data acquired from the 3D X-ray CT analysis of the three EBM Ti64 samples are presented in **Table 9**.

Table 9 Statistics of defect distribution, obtained using X-ray computed tomography (CT) analysis, of as-built EBM Ti6Al4V samples with different orientations.

Sample Orientation	Diameter Range of 95% Defects (mm)	Mean Diameter of Defects (mm)	Volume of Analyzed Material (mm^3)	Defect Volume (mm^3)	Defect Volume Ratio (%)
Flat-built	0.02-0.20	0.07	394.54	0.69	0.17
Side-built	0.02-0.11	0.06	332.00	0.16	0.05
Top-built	0.02-0.11	0.06	332.96	0.16	0.05

In the flat-built sample, the un-melted powder particle regions are found to be distributed along the scanning length in the longitudinal direction, and also extending to the depth of the sample, as can be observed from **Figure 45**a. The growth of this un-melted region was parallel to the build direction. This lack of melting defects is mainly caused by inadequate energy density delivery, as a result of a deviation of the scanning parameters from the desired ones, mainly due to variation either in the power source, scanning system maneuver, or from an intervention coming from other factors such as electromagnetic interference [67,135]. The electron beam scanning direction is along the longitudinal and tensile loading direction, the defects which are distributed along the scanning path and produced by this inadequate energy delivery have hardly any effect on the tensile strength properties, as could be noticed from the earlier mechanical property measurements discussion. **Figure 45**b shows the frequencies of the distributed defects inside the flat-built sample. In this sample, 95% of the defects were observed to be in the diameter range of 20 µm to 150 µm, with a mean defect diameter of around 70 µm. Furthermore, the bulk of the defects, with a significant number of counts, is situated below 120 µm. Most of the defects are en-trapped gas porosity, which is uniform in shape. There are several larger, non-uniform, un-melted, or partially melted region defects, which could be very critical to the performance of the final parts and need to be taken care of through process parameter optimization or other techniques.

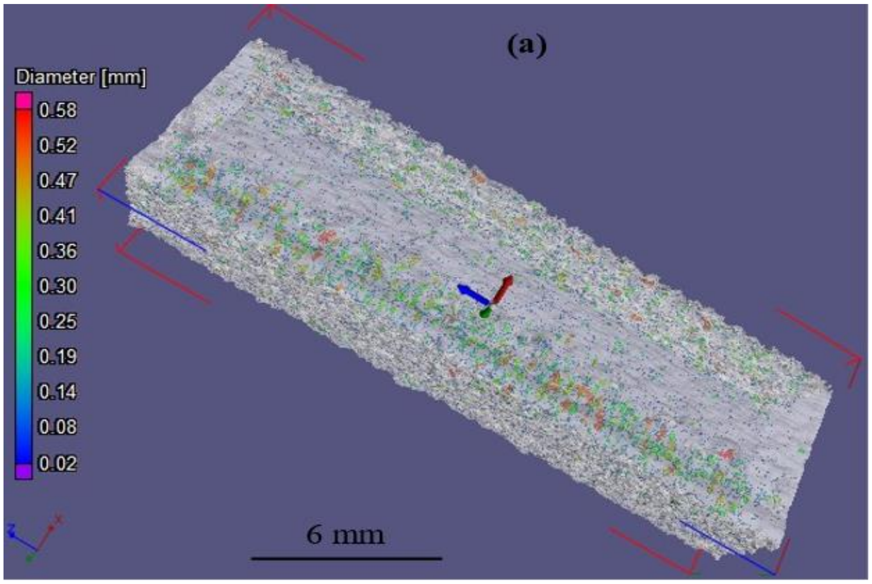

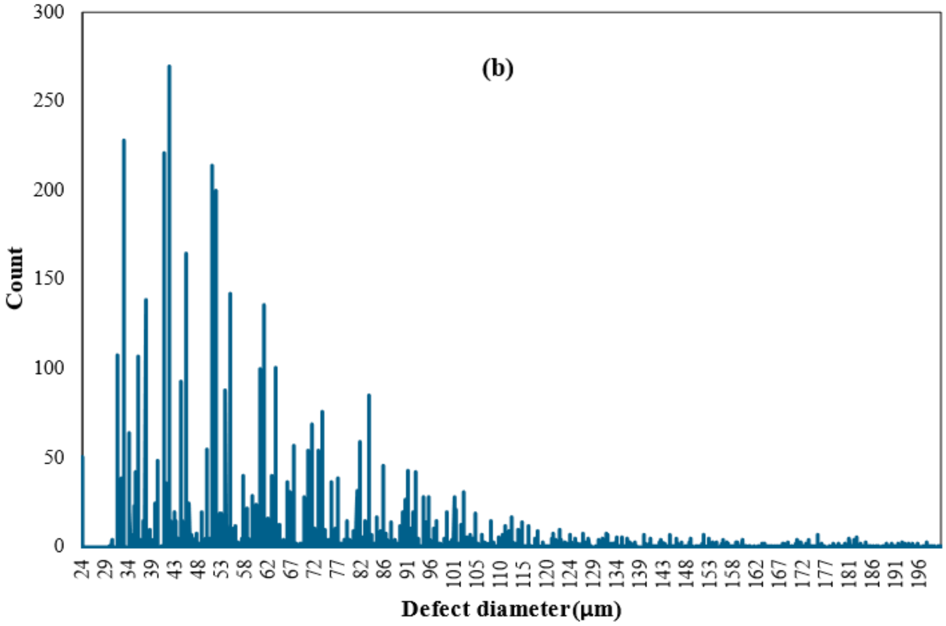

Figure 45 Defect distribution on the flat-built sample, obtained from X-ray CT analysis, (a) 3D defect distribution inside the sample, and (b) frequencies of the distributed defects.

However, **Figure 46** and **Figure 47** show that both the side-built and top-built samples have a similar kind of defect distribution inside them. In these two samples, the severity and intensity of the defects' formation and distribution are much lower compared to the case of the flat-built samples (**Figure 45**). In the side-built and top-built samples, the porosity and other internal defects are distributed very homogeneously, where a majority (95%) of the defects are found to be in the diameter range of 20 µm to 110 µm, with a mean defect diameter of around 60 µm. In the side-built samples, the majority of the defects with a significant number of counts are below the diameter of 80 µm, and this figure is below 70 µm in the top-built sample. Although there are hardly any long un-melted or partially melted powder particle regions in these two samples as opposed to the flat-built sample, there are still some smaller un-melted or partially melted regions that could be detrimental to their fatigue performances.

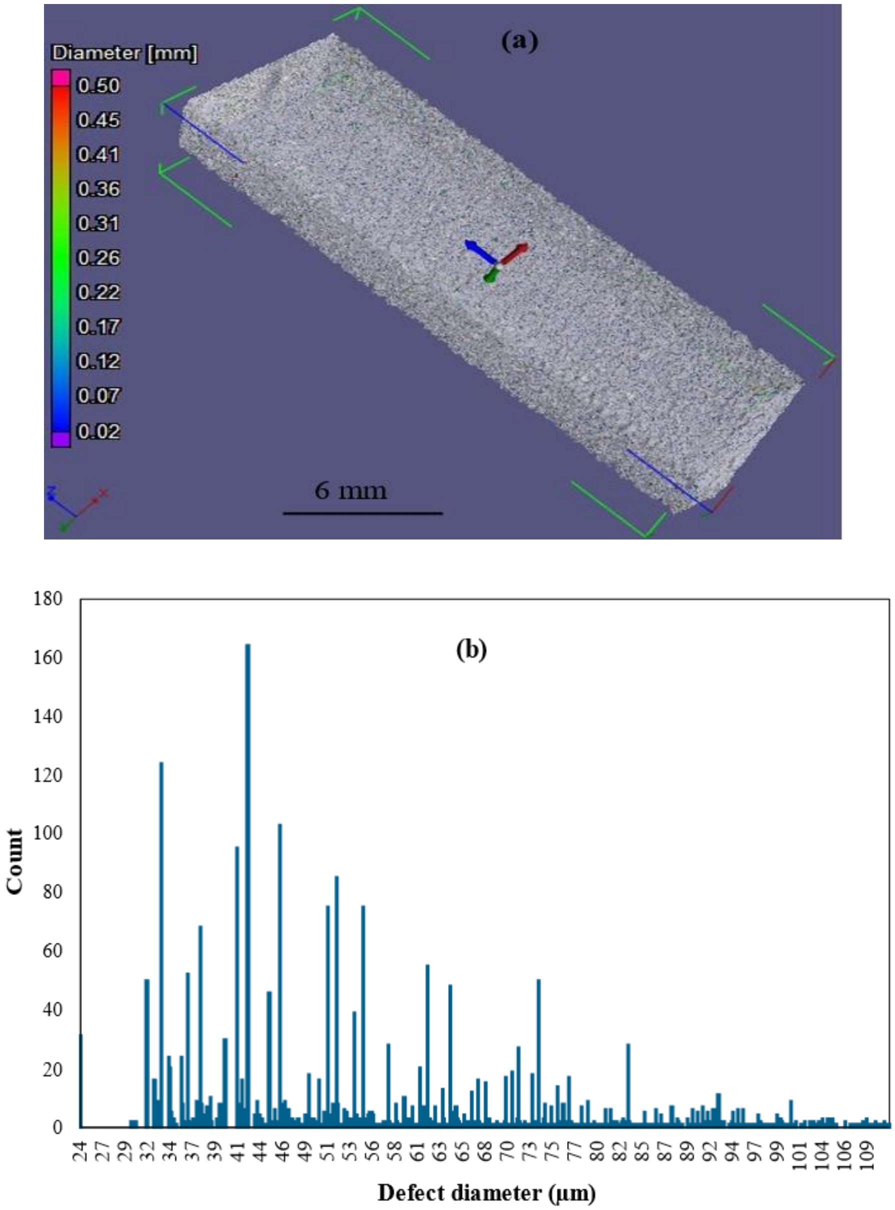

Figure 46 Defect distribution on the side-built sample, obtained from X-ray CT analysis, (a) 3D defect distribution inside the sample, and (b) frequencies of the distributed defects.

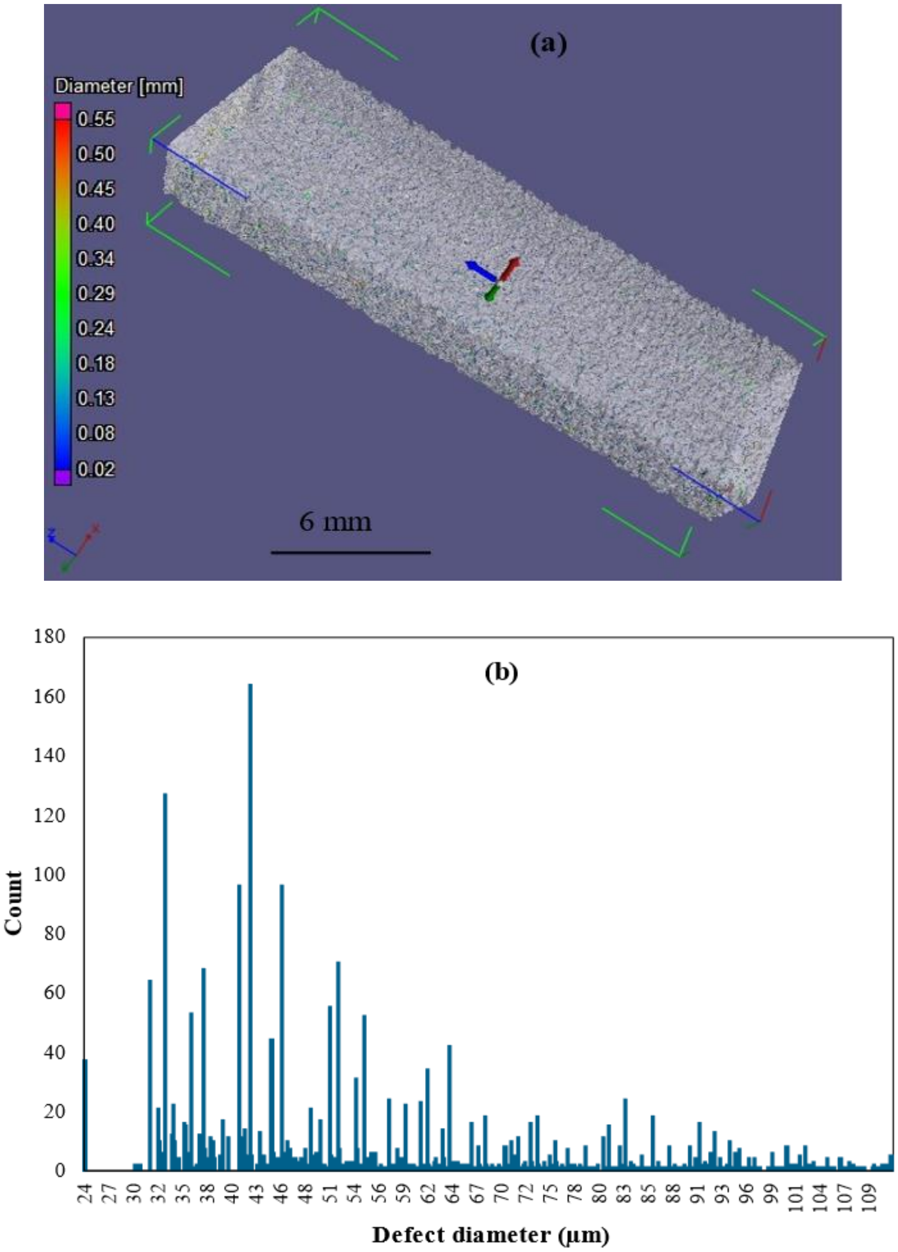

Figure 47 Defect distribution on the top-built sample, obtained from X-ray CT analysis, (a) 3D defect distribution inside the sample, and (b) frequencies of the distributed defects.

Furthermore, the morphology of the defect distribution has been analyzed to observe how it changes with the defect diameter. The morphology of various available defects can be realized by the sphericity parameter (S), which is defined as **Equation 8** [30]. Here, the V and A are the volume and surface area of the defect, respectively. The sphericity (S) ranges between the values of 0 and 1. A smaller S means an irregular or flatter shape defect. The defect has a more spherical or regular shape as the sphericity value grows larger and closer to 1.

$$S = \frac{\pi^{1/3}(6V)^{2/3}}{A} \qquad 8$$

The sphericity of defects inside the flat-built sample spreads between 0.35 and 0.75 and decreases with an increasing defect diameter, which could be as high as 210 μm, as presented in **Figure 48**a. This further confirms that the flat-built sample has a large number of irregular-shaped defects with low defect sphericity and high diameter. The porosity, which generates from the lack-of-fusion (LOF) defect, normally has a very irregular shape and large diameter, as observed in this case [64]. The scattering length of the sphericity becomes narrower with an increasing defect diameter in flat-built samples. However, the sphericity of defects for side-built and top-built samples scatter between 0.42 and 0.73 (**Figure 48**b,c), while most of the defects have sphericity greater than 0.45. The defect diameters are also constrained below 120 μm in these two cases. Therefore, the regularity of the defects in these two samples is much better than in the flat-built sample.

The width of the scatter in sphericity grows larger with an increasing defect diameter in both the side-built and top-built samples, as opposed to the case of a flat-built sample. This further indicates that the severity of the defects in side-built and top-built samples is lower than in the flat-built ones. Furthermore, the comparison of the trendlines of the sphericity distribution with defect diameter among the three samples is presented in **Figure 48**d. All three lines meet at a defect diameter of around 43 µm. The flat-built sample has higher sphericity below this intersection point and lower sphericity beyond that, as compared to the other two samples. Again, the flat-built sample has significantly low sphericity of the defects with a very large diameter, which could make it highly susceptible to faster failure under fatigue critical applications. Although both the side-built and top-built samples have similar trendlines, the latter has slightly lower sphericity in the larger defect region. All of the internal defects have highly irregular morphology, lower sphericity, and larger defect diameters might be very crucial as potential crack initiation and propagation sites under fatigue loading. Therefore, although surface defects are more crucial to the fatigue performance, the internal porosity defects with sharp morphology, as created due to lack of melting, might also adversely affect the performance of the as-built metal AM parts under different quasi-static and cyclic loading, leading to premature failure.

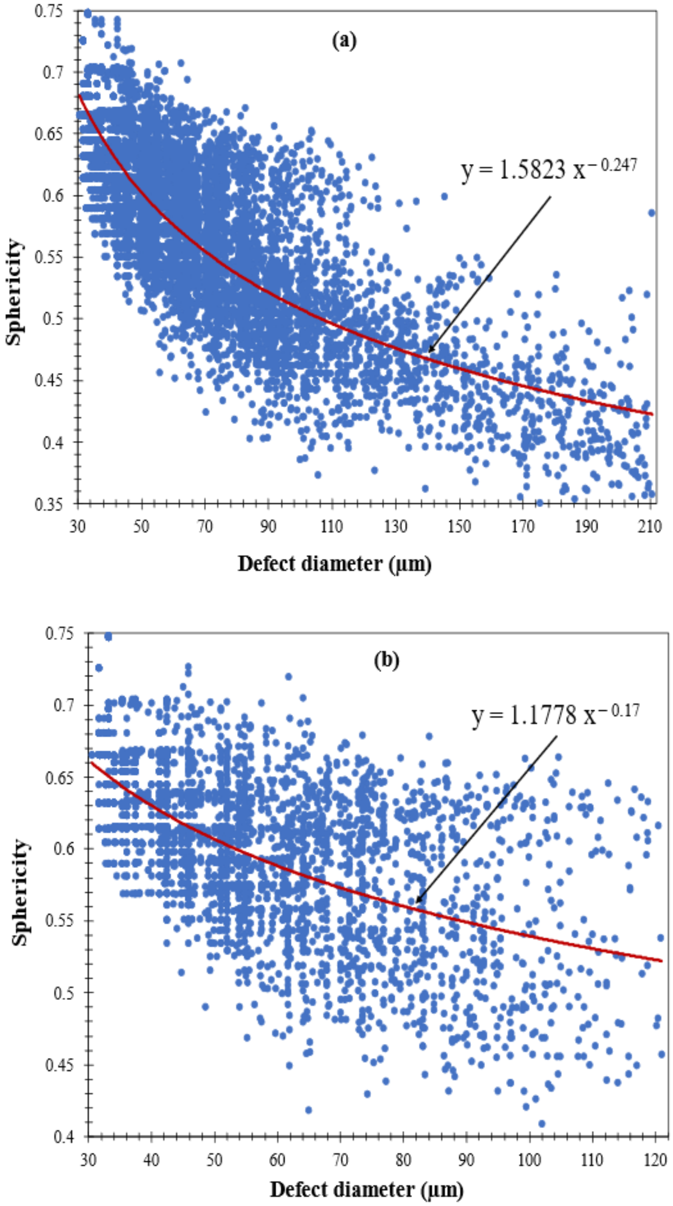
(a)
y = 1.5823 x^−0.247
Sphericity
0.75
0.7
0.65
0.6
0.55
0.5
0.45
0.4
0.35
30
50
70
90
110
130
150
170
190
210
Defect diameter (µm)
(b)
y = 1.1778 x^−0.17
Sphericity
0.75
0.7
0.65
0.6
0.55
0.5
0.45
0.4
30
40
50
60
70
80
90
100
110
120
Defect diameter (µm)

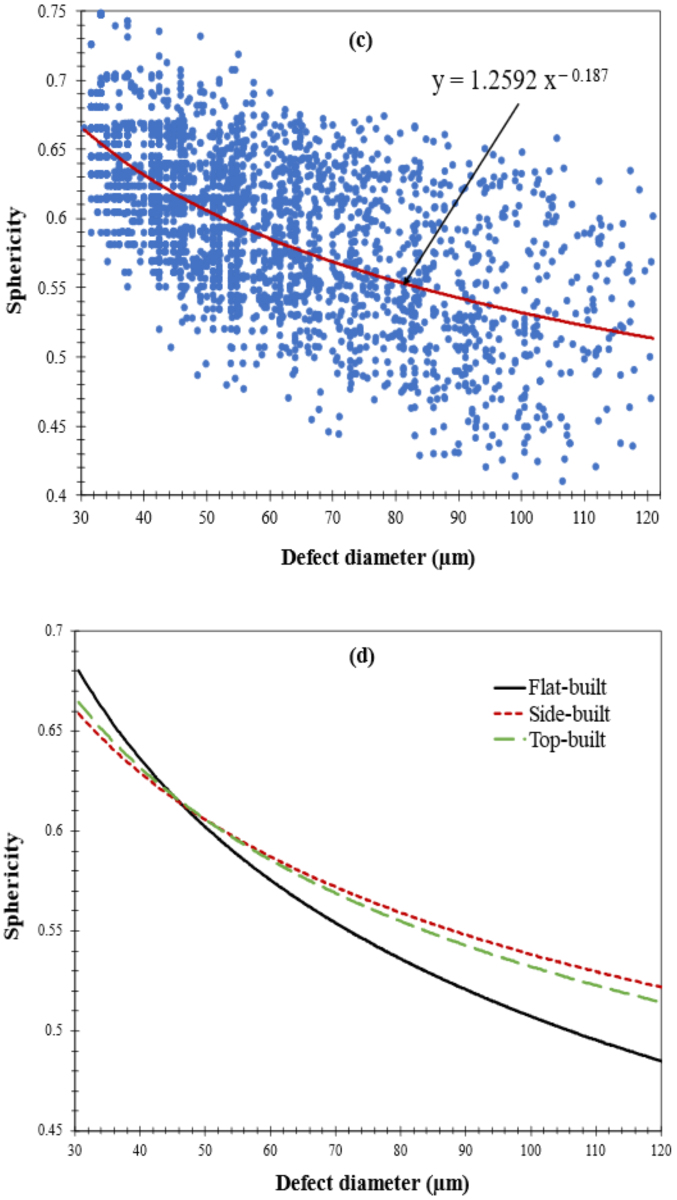

Figure 48 The scatter distribution of sphericity with increasing defect diameters of (a) flat-built, (b) side-built, and (c) top-built samples, along with (d) the comparison of the trendlines of the sphericity distribution among the three samples.

Finally, although the flat-built sample has a very poor porosity value with lower sphericity of defects as opposed to the side-built and top-built samples, it also possesses overall better mechanical properties under tensile loading. Again, the external surface roughness defects demonstrate the opposite trend as internal defects, where the flat-built sample has a better surface finish than the other two samples. Still, the variation of average surface roughness, as calculated from different sides of the samples, is not that significant among the different orientations. Therefore, the effect of porosity and surface roughness on the anisotropic mechanical strength behavior of EB-PBF Ti6Al4V parts might not be that significant. This may also indicate that another underlying reason could be the cause of the significant anisotropy that is observed in the mechanical properties of the different build orientations. Previous studies have shown that the variation in columnar grain growth observed in different build orientations, along with microstructural variation, could be responsible for the anisotropic behaviors [45]. This variation in microstructure occurs due to several different factors, including variation in cooling rates and thermal gradients, and impacts the grain formation and growth during the process.

Some samples from all orientations have excessively high porosity values because of the elongated lack of fusion defects. Those defects contributed to premature failure under tensile loading. Consequently, they displayed very poor strength properties and percent elongation as compared to the specimens with minimum internal defects. Therefore, those measurements were discarded from the analysis. Such a sample (flat-built) with severe porosity defects has been presented in **Figure 49**. Two areas of large un-melted regions along the X direction could be observed, as shown in the top plane. These defects also accumulated across several layers in the build direction, as can be noticed from the front plane of this flat-built sample. In this particular sample, the defect volume ratio was 0.35%, which is two times larger than the average porosity value of a similar sample. Therefore, this type of sample failed pretty faster and showed very low percent elongation than the sample with lesser defects.

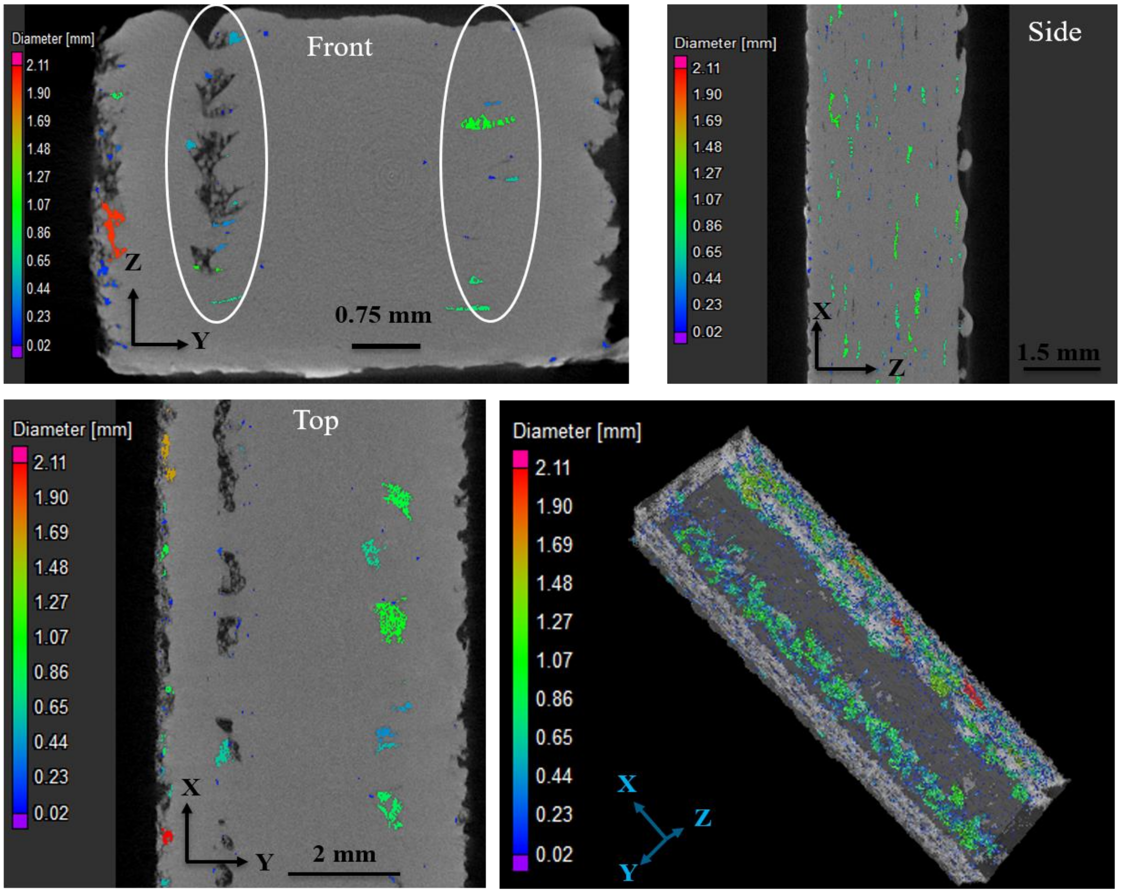

Figure 49 Flat-built sample with severe porosity defects identified on the cross-section of the three planes

4.8 Fatigue Strength Prediction of As-built Ti6Al4V Parts from the Inherent Defects

4.8.1 Fatigue Limit Prediction Model

The fatigue strength of the as-built EBM Ti-6Al-4V sample without any post-processing treatment has been found to be in the range of 150-350 MPa at around 10^7cycles [81],[136–138]. After doing different post-processing treatments such as machining, hot isostatic pressing (HIP), and heat treatment, the fatigue strength could be increased up to 550-600 MPa or more [138]. This increase in fatigue strength is mainly due to the changes in microstructure, surface roughness, porosity, and voids because of those post-treatments. Although high surface roughness is one of the key reasons for low fatigue properties of as-built EBM Ti-6Al-4V parts, the correlation between the fatigue life and surface profile has not been analyzed well enough in the available literature to the author's knowledge. Moreover, though surface defects are more crucial to fatigue performance, the internal defects with acute morphology, mainly lack-of-fusion defects, might also contribute adversely to the fatigue properties of the as-built metal AM parts. As a result, consideration of both the internal and external surface defects would possibly provide a more accurate perdition of fatigue performance of the as-built metal AM parts. In this study, different surface roughness and internal defect parameters were utilized to predict fatigue strength, σ_W quantitively using Murakami’s modified $\sqrt{area}$ parameter model [90] as follows,

$$\sigma_w \quad = \quad \frac{C_1 * (HV + 120)}{(\sqrt{area})^{1/6}} * \left[\frac{1-R}{2}\right]^{\alpha} \qquad 9$$

Where $\sqrt{area}$ is defined as the square root of the projected 'defect area' of a defect on a plane perpendicular to the maximum principal stress. *HV* is Vickers hardness, and C_1 is location parameter (C_1 = 1.43 for surface defects, C_1 = 1.41 for subsurface defects, and C_1 = 1.56 for internal defects). *R* is the stress ratio, $\sigma_{min}/\sigma_{max}$, and the α is dependent upon HV by the equation as, $\alpha = 0.226 + HV \times 10^{-4}$. While HV is in kgf/mm^2 and can be calculated from the hardness measurement of the samples. Thus, the fatigue strength can be approximated from the square root of the defect area, which could also be represented as $\sqrt{area_R}$ and $\sqrt{area_{ID}}$ for surface roughness and internal defect, respectively, and the Vickers hardness without any further destructive fatigue testing.

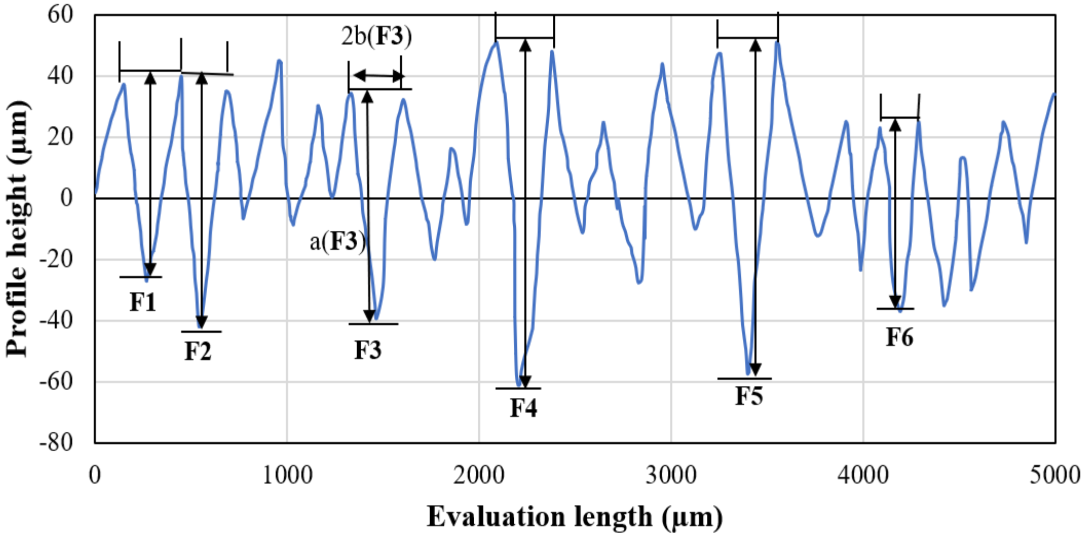

Figure 50 Surface profile of the flat-built sample, taken along the loading direction using a stylus profiler, showing the critical profile valleys along with the pitch (*2b*) and depth (*a*) of them.

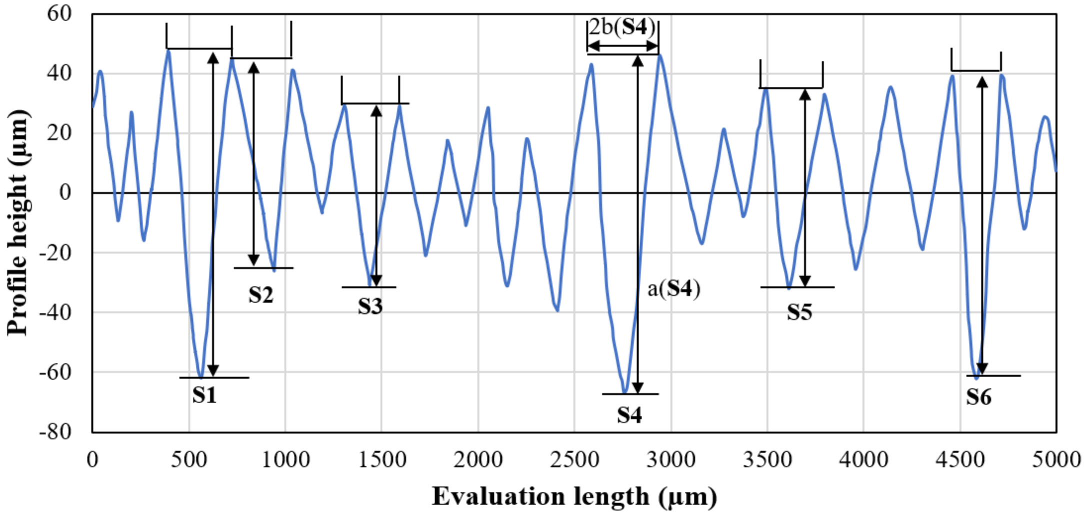

Figure 51 Surface profile of the side-built sample, taken along the loading direction using a stylus profiler, showing the critical profile valleys along with the pitch (*2b*) and depth (*a*) of them.

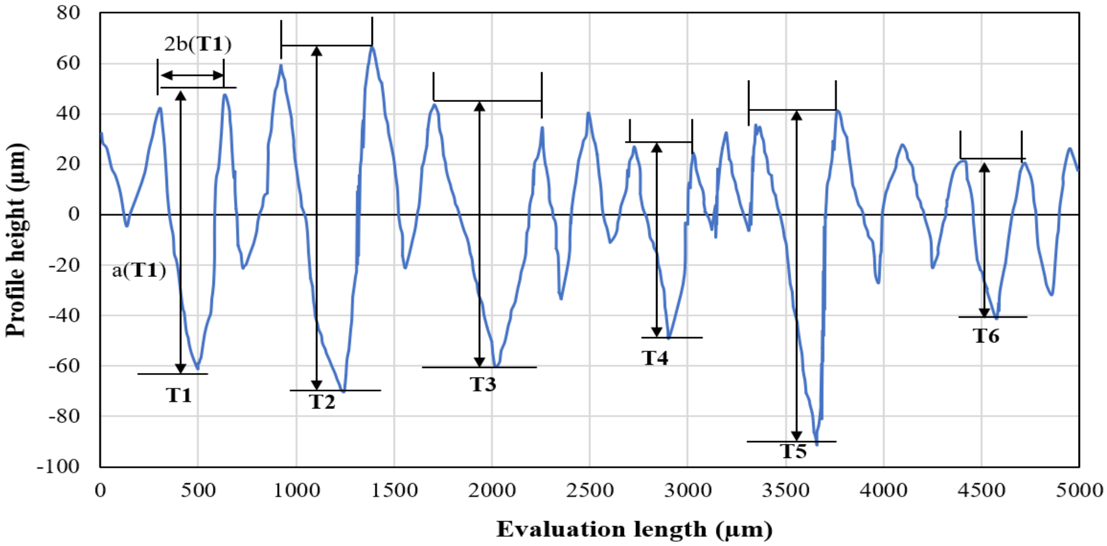

Figure 52 Surface profile of the top-built sample, taken along the loading direction using a stylus profiler, showing the critical profile valleys along with the pitch (*2b*) and depth (*a*) of them.

Surface roughness can be considered as micro notches which could be responsible for the fatigue crack initiation and propagation [81],[139]. Moreover, from the valley of the measured surface profile, two important profile parameters, the pitch (*2b*) and the depth (*a*) of the surface profile, can be extracted as presented in **Figure 50, Figure 51,** and **Figure 52**. These three figures exhibit six critical valleys for each of the surface profiles, which are potential crack initiation and propagation sites, hence are selected for fatigue limit calculation. Furthermore, the equivalent size of these crucial surface defects, $\sqrt{area_R}$ can be found by using an empirical equation derived by Murakami [90] from the relation between $\sqrt{area_R}/2b$ and *a*/*2b* as follows,

$$\frac{\sqrt{area_R}}{2b} \cong 2.97\left(\frac{a}{2b}\right) - 3.51\left(\frac{a}{2b}\right)^2 - 9.74\left(\frac{a}{2b}\right)^3;\ for\frac{a}{2b} < 0.195$$

$$\frac{\sqrt{area_R}}{2b} \cong 0.38;\ \ for\frac{a}{2b} > 0.195 \qquad 10$$

Thus, by determining the ratios of depth and pitch (a/2b) from the different surface profile measurements, as shown in **Figure 50, Figure 51,** and **Figure 52**, the square root of the equivalent surface roughness defect area, $\sqrt{area_R}$ can be obtained using **Equation 10**.

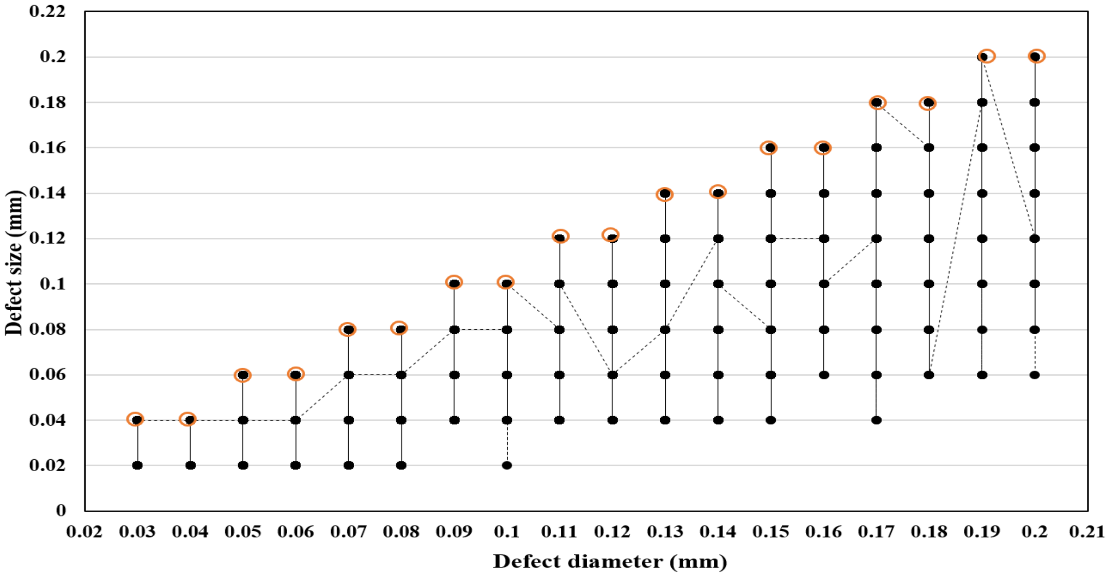

Figure 53 The size distribution along the loading direction of internal defects with various diameters for flat-built sample.

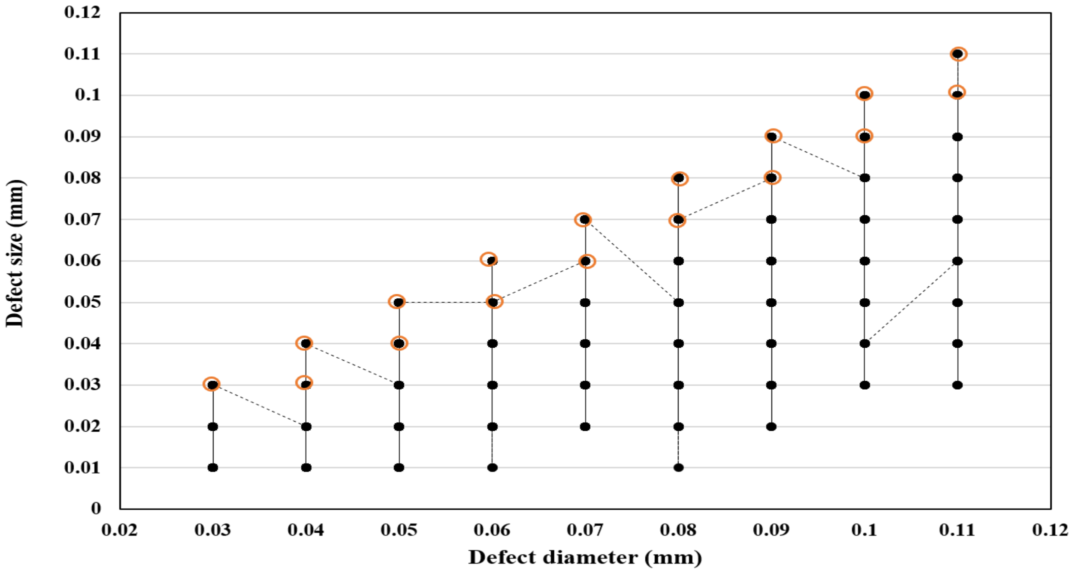

Figure 54 The size distribution along the loading direction of internal defects with various diameters for the side-built sample.

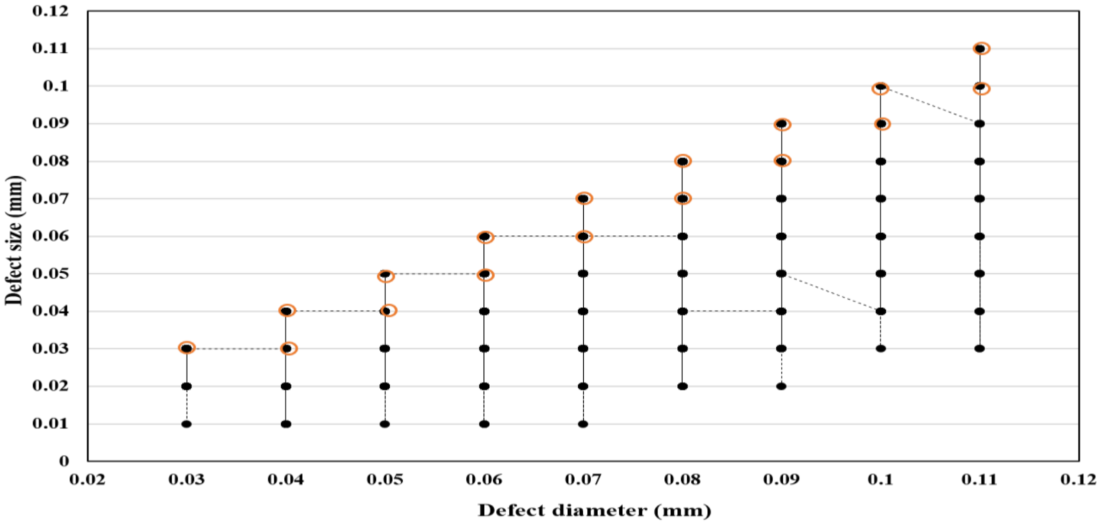

Figure 55 The size distribution along the loading direction of internal defects with various diameters for the top-built sample.

Similarly, the diameter (d) and size (h) of the critical internal defects, as circled in **Figure 53**, **Figure 54**, and **Figure 55** and obtained from X-ray computer tomography (CT), are extracted for all three kinds of samples, which are flat-built, side-built, and top-built. The square root of the projected internal defect area, $\sqrt{area_{ID}}$ can be calculated using the Murakami and Endo's model [90] as shown below,

$$\sqrt{area_{ID}} = \sqrt{dh - d^2/4\sqrt{3}} \qquad 11$$

Furthermore, these calculated values of $\sqrt{area_R}$ and $\sqrt{area_{ID}}$ can be used for predicting the fatigue limit, σ_w , which is the maximum stress a part can take before crack propagation under the constant amplitude fatigue loading at around 10^7 cycles, using **Equation 9**.

4.8.2 Results and Discussions

The current study has applied the fatigue strength prediction model described above for calculating the approximate fatigue strength of as-built EBM Ti-6Al-4V parts, built in three different orientations, using surface roughness measurement data, internal defect, and Vickers hardness values of these samples. Based on the described formulas, an algorithm was developed to compute the fatigue strength values for different a/2b ratios extracted from the surface profiles of the three different samples with three build orientations, as shown in **Table 10**.

Table 10 Fatigue limit, $\boldsymbol{\sigma_w}$ (MPa) calculation using the extracted surface profile data

Build orientation	Observation No.	Profile depth, a (µm)	Profile pitch, 2b (µm)	a/2b ratio	$\sqrt{area_R}$ (µm)	Fatigue limit, σ_w (MPa) (R = -1)	Fatigue limit, σ_w (MPa) (R = 0.1)
Flat-built	F1	66	299	0.22	113.62	302	245
	F2	81	240	0.34	91.2	313	255
	F3	73	282	0.26	107.16	305	248
	F4	112	297	0.38	112.86	303	246
	F5	108	304	0.35	115.52	301	245

	F6	62	203	0.31	77.14	322	262
	Mean	84	270.83	0.31	102.92	308	250
	77	289.5	0.33	110	304	247	77
	Std. dev	21.43	40.63	0.06	15.44	8.24	6.91
Side-built	S1	110	331	0.33	125.78	280	228
	S2	74	313	0.24	118.94	282	230
	S3	58	281	0.21	106.78	288	234
	S4	113	351	0.32	133.38	277	225
	S5	66	305	0.22	115.9	284	231
	S6	101	266	0.38	101.08	290	236
	Mean	87	307.83	0.28	116.98	283	231
	Median	87	309	0.28	117.42	283	230.5
	Std. dev	24	31.32	0.07	11.90	4.89	3.98
Top-built	T1	108	325	0.33	123.5	265	216
	T2	135	456	0.30	173.3	251	204
	T3	101	535	0.19	197.98	245	200
	T4	70	310	0.23	117.8	267	218
	T5	131	415	0.32	157.7	255	208
	T6	61	315	0.19	117.43	267	218
	Mean	101	392.67	0.26	147.95	258	211
	Median	105	370	0.26	140.6	260	212
	Std. dev.	30.55	91.88	0.06	33.70	9.35	7.76

Similarly, the fatigue limits of the three samples have been calculated from the projected square root areas of internal defects as provided in the following tables, which are **Table 11**, **Table 12**, and **Table 13**.

Table 11 Fatigue limit, $\boldsymbol{\sigma_w}$ (MPa) calculation using the internal defect data for flat-built sample

Build Orientation	Observation No.	Defect Diameter, d (µm)	Defect Size, h (µm)	$\sqrt{area_{ID}}$ (µm)	Fatigue limit, σ_w(MPa) (R = -1)	Fatigue limit, σ_w (MPa) (R = 0.1)
Flat-built	1	30	40	32.71	406	329
	2	40	40	37.00	397	323
	3	50	60	51.37	376	306
	4	60	60	55.50	371	302
	5	70	80	69.95	357	290
	6	80	80	74.00	354	287
	7	90	100	88.49	344	279
	8	100	100	92.50	341	277
	9	110	120	107.02	333	270

	10	120	120	111.00	331	269
	11	130	140	125.54	324	263
	12	140	140	129.50	323	262
	13	150	160	144.06	317	257
	14	160	160	148.00	315	256
	15	170	180	162.57	310	252
	16	180	180	166.50	309	251
	17	190	200	181.08	305	248
	18	200	200	185.00	304	247
	Mean	115	120	108.99	340	276
	Median	115	120	109.01	332	269.5
	Std. dev.	53.38	53.14	49.25	31.22	25.39

Table 12 Fatigue limit, $\boldsymbol{\sigma_w}$ (MPa) calculation using the internal defect data for the side-built sample

Build Orientation	Observation No.	Defect Diameter, d (μm)	Defect Size, h (μm)	$\sqrt{area_{ID}}$ (μm)	Fatigue limit, σ_w(MPa) (R = -1)	Fatigue limit, σ_w (MPa) (R = 0.1)

Side-built	1	30	30	27.75	393	320
	2	40	30	31.13	385	314
	3	40	40	37.00	374	305
	4	50	40	40.49	369	300
	5	50	50	46.25	360	293
	5	60	50	49.80	356	290
	7	60	60	55.50	350	285
	8	70	60	59.10	346	282
	9	70	70	64.75	341	277
	10	80	70	68.38	338	275
	11	80	80	74.00	333	271
	12	90	80	77.66	331	269
	13	90	90	83.25	327	266
	14	100	90	86.93	325	264
	15	100	100	92.50	321	261
	16	110	100	96.19	319	260
	17	110	110	101.75	316	257
	Mean	72	68	64.26	346	282
	Median	70	70	64.75	341	277
	Std. dev.	25.38	25.38	23.40	23.58	19.38

Table 13 Fatigue limit, $\boldsymbol{\sigma_w}$ (MPa) calculation using the internal defect data for top-built sample

Build Orientation	Observation No.	Defect Diameter, d (µm)	Defect Size, h (µm)	$\sqrt{area_{ID}}$ (µm)	Fatigue limit, σ_w(MPa) (R = -1)	Fatigue limit, σ_w(MPa) (R = 0.1)
Top-built	1	30	30	27.75	371	303
	2	40	30	31.13	364	297
	3	40	40	37.00	354	288
	4	50	40	40.49	348	284
	5	50	50	46.25	341	278
	5	60	50	49.80	337	274
	7	60	60	55.50	331	270
	8	70	60	59.10	327	267
	9	70	70	64.75	322	263
	10	80	70	68.38	319	260
	11	80	80	74.00	315	257
	12	90	80	77.66	313	255
	13	90	90	83.25	309	252
	14	100	90	86.93	307	250
	15	100	100	92.50	304	248

	16	110	100	96.19	302	246
	17	110	110	101.75	299	244
	Mean	72	68	64.26	327	267
	Median	70	70	64.75	322	263
	Std. dev	25.38	25.38	23.40	22.19	18.13

The obtained fatigue limits from both surface and internal defects have been compared to see which one has a more severe effect on the fatigue strength, as shown in **Figure 56**. The surface defects are more crucial for determining the fatigue limit since they provide a much lower fatigue limit as compared to the internal defect case. Therefore, the fatigue strength calculated from these surface defects will be used for further analysis onward. Besides, the effect of build orientation on the fatigue strength is examined and exhibited in **Figure 56,** for two stress ratios which are R = -1 and R = 0.1. At zero mean stress (R = -1), the flat-built sample has better fatigue strength than the other two samples, in the range of 301 – 322 MPa, which is way better than the top-built sample. This complies well with the fact that the flat-built sample has a smoother surface and superior tensile strength than both the side-built and top-built samples. Conversely, the top-built sample has lower fatigue strength in the range of 245 – 267 MPa, because of having the highest surface roughness and lowest tensile strength among all three orientations. A similar trend has been observed in the case of positive mean stress as well, while the value of R is taken as 0.1. Again, the mean stress has a significant effect on the fatigue limit, which can be noticed from **Figure 56** as well. Here, the fatigue strength decreases considerably with the increase of mean stress from zero to positive values for all the orientations. The average fatigue limit values computed from this predictive model for as-built EBM Ti-6Al-4V parts built in different orientations range between 200 - 322 MPa (considering both stress ratios), which also comply well with different experimental data available in the literature.

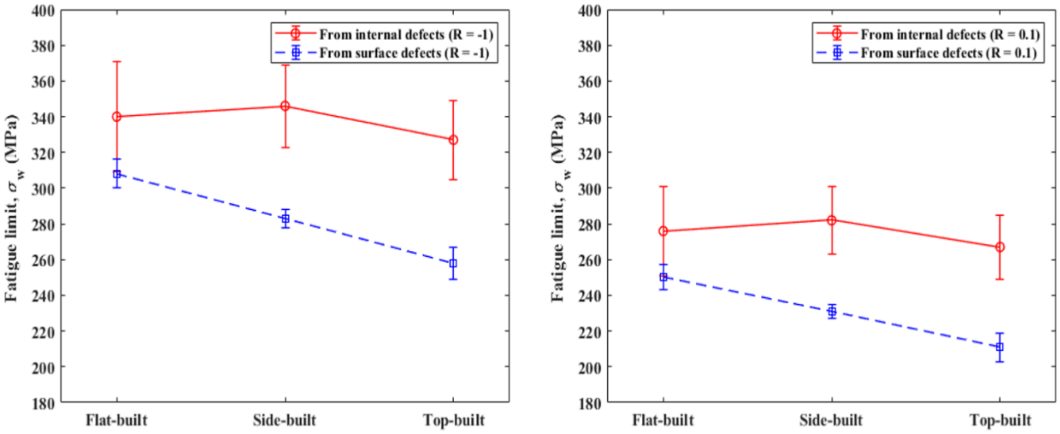

(a) (b)

Figure 56 The fatigue strength prediction data of the three as-built EBM Ti-6Al-4V samples with three different build orientations, (a) at R = -1 (mean stress is zero), and (b) at R = 0.1 (mean stress is greater than zero).

Furthermore, it can be noted from **Table 10** that surface profile depth is very crucial for fatigue strength. The flat-built sample has a minimum average profile depth (83 µm), and consequently, it has superior fatigue strength as compared to the other two orientations. On the contrary, the top-built sample has a larger average profile depth of 101 µm, hence lower fatigue strength than the other two samples. However, as the profile depth dictates the surface roughness of the sample, they have a similar impact on fatigue strength. The effect of surface roughness on the fatigue limit of EBM Ti-6Al-4V parts has been analyzed by comparing the predicted values from the current model, and the experimental values gathered from the literature as shown in **Figure 57**. It further shows the agreement between the predictive model and the experimental values. It also depicts that the fatigue strength decreases with the increasing surface roughness. The Wrought Ti-6Al-4V part exhibits a very high fatigue strength of around 800 MPa, mainly because of having a surface roughness below 5 µm. Various other post-processing treatments also contribute to the improved fatigue strength of wrought Ti64, in addition to the low surface roughness. Furthermore, an exponential physical model can be derived from the exhibited trend among the average surface roughness (Ra) and fatigue limit (σ_w), as $\sigma_w = 1457Ra^{-0.616}$ which can be seen from **Figure 57** as well.

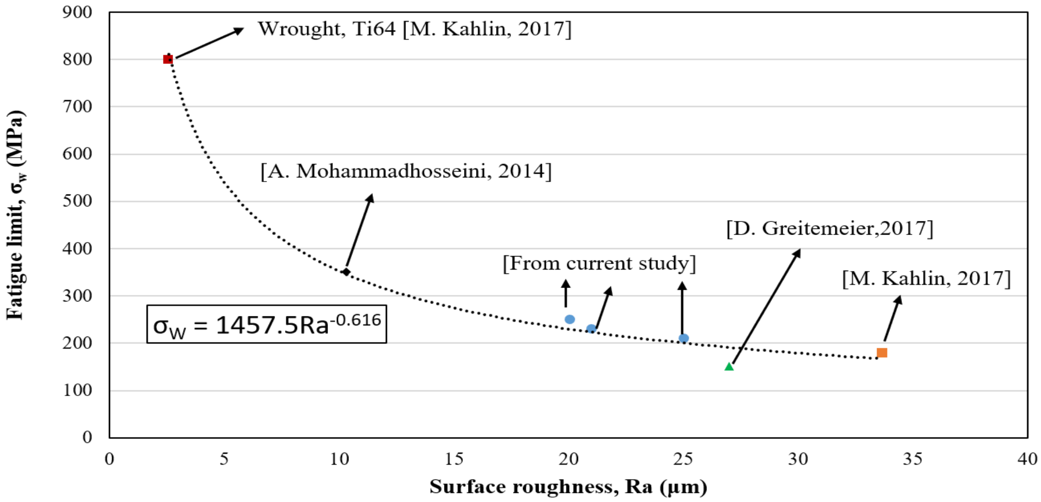

Figure 57 The effect of surface roughness on fatigue limit (R= 0.1) with a power trendline for EBM Ti6Al4V parts, as compared to the wrought machined parts

4.8.3 Fatigue Strength Prediction at 1000 Cycles

Fatigue testing is generally a very tedious and time-consuming process. So a non-destructive and quick method of fatigue life prediction is very crucial [140]. The fatigue limit of as-built EBM Ti-6Al-4V parts at 10^7 cycles has already been determined using Murakami's $\sqrt{area}$ parameter model considering the equivalent surface roughness defects. Similarly, fatigue strength at 1000 cycles can be approximated from the Basquin's model [141] as provided below,

$$(\sigma_f)_{N_f} = \sigma_F(2N_f)^b \tag{12}$$

At 1000 cycles which becomes,

$$(\sigma_f)_{10^3} = \sigma_F(2\ \times 10^3)^b \tag{13}$$

Where, N_f is the number of cycles, and σ_f is the fatigue strength at any specific cycle. σ_F is the fatigue strength coefficient and can be approximated for powder bed AM Ti-6Al-4V as σ_F = 1163 MPa [142]. And b is the fatigue strength exponent, which can be found by inserting the fatigue limit, σ_W and the corresponding cycle, 10^7 in the Basquin's equation as follows,

$$b = -\frac{\log(\sigma_F/\sigma_w)}{\log(2 \times 10^7)} \tag{14}$$

Utilizing the two predictive methods discussed above, the approximation of the stress amplitude vs. number of cycles to failure (S-N) diagram from 1000 cycles to 10^7 cycles was obtained for the as-built EBM Ti6Al4V parts as shown in

Figure 58. S-N curves for three samples, built in the three different orientations, have been predicted at two stress ratios of R = 1 and R = 0.1 from the measurement of surface roughness and Vickers hardness. The top-built sample, in which the loading direction is parallel to the build direction, exhibits the lowest fatigue properties because of having a comparatively poor surface finish and lower hardness as opposed to the other two samples, as shown in **Figure 58**. However, the flat-built sample shows better fatigue strength curves than the side-built sample since the former has relatively less critical surface irregularities as well as higher hardness than the latter one. The predicted model also shows that the fatigue performance of Ti-6Al-4V alloy built by EBM could be very poor because this process produces a very rough surface. When compared with the experimental stress vs number of cycles data of as-built EBM Ti6Al4V alloy available in the literature, the predicted model complies reasonably well with the scatter for both the high cycle fatigue (HCF) region and the low cycle fatigue (LCF) region. The experimental scatter obtained from [Gunther, 2017] and [Hrabe, 2017] are in pretty good agreement with the predicted model at the stress ratios of R=-1 and R=0.1, respectively. Furthermore, a similar approach where the combination of the material property like hardness and manufacturing defects such as surface roughness and internal porosity is used for fatigue strength prediction of as-built metal parts could be applied into other PBF processes as well.

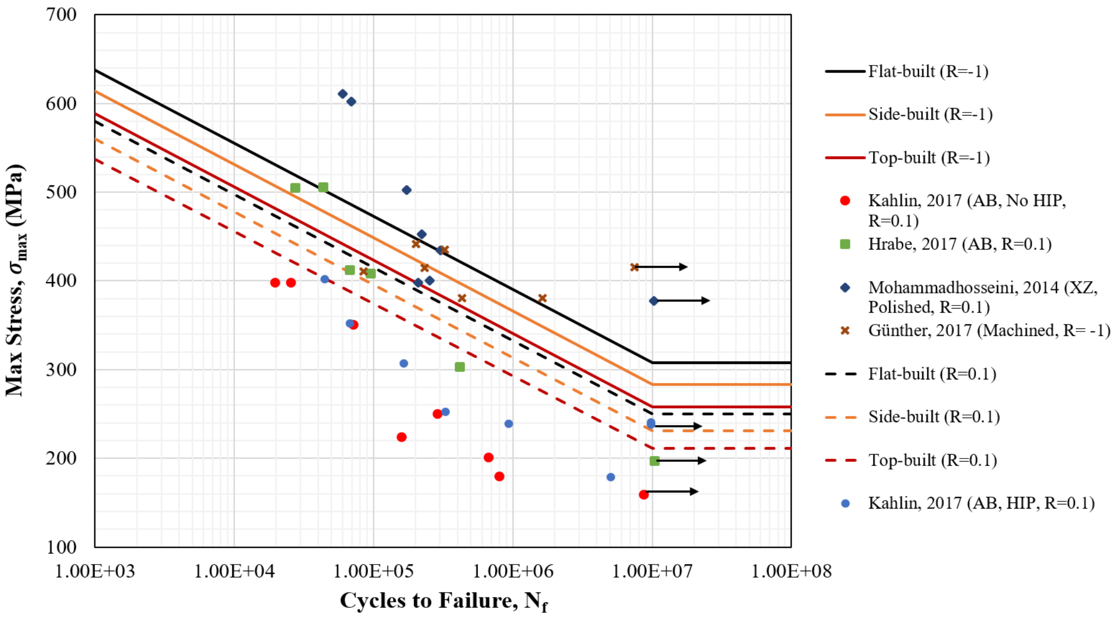

Figure 58 Linear model of maximum stress vs. number of cycles to failure (S-N) curves predicted from surface anomalies and Vickers hardness of as-built EBM Ti6Al4V parts produced in three build orientations and compared with literature values.

CHAPTER 5

CONCLUSIONS

The EB-PBF AM built Ti6Al4V samples showed significant anisotropic behavior mainly because of the variation of cooling rates and subsequent microstructural changes in different built orientations. The flat-built sample displayed greater mechanical properties at all testing temperatures than both the side-built and top-built samples in the case for all tensile properties except percent elongation. The flat-built sample has an excellent ultimate tensile strength which is almost 21% and 32% larger than the other two later orientations, respectively. The variation of the intensity of grain texture, grain orientation, size distribution, and microstructural formation is mainly responsible for anisotropic behaviors. The direction of homoepitaxial growth of the columnar grains, being different with respect to the loading directions of three samples, also contributes to the anisotropic behaviors.

The sample which has a minimum number of layers that are parallel to the loading directions has the highest flow stress properties at all temperatures as compared to the sample that has a maximum number of layers that are perpendicular to the loading direction. But the former loses the ductility with the increase in strength, whereas the latter has the highest ductility. These anisotropic behaviors could be due to mainly the change in microstructure during the building process of the samples due to the variation in cooling rates and temperature gradient in different orientations. Besides, the changes in distribution, location, and shapes of the various formed defects, such as porosity, un-melted powder particles, and surface roughness, with build orientations could also contribute partially to the anisotropic behaviors of EBM Ti6Al4V parts.

The microstructural analysis of Ti6Al4V samples built using electron beam melting PBF AM process showed the presence of both α phase and β phase. More than 90% of the grains consist of the α phase, whereas there is a very small amount of β phases distributed at the grain boundaries of the α matrix. The EBSD analysis revealed that the microstructures of the EBM-built Ti6Al4V parts consist mainly of α colony, α basket-weave platelets along with a small amount of β phases distributed along the grain boundaries of the alpha phases. However, the variation in preferred grain orientation, grain size, the intensity of harmonic grain texture, grain boundary misorientation angles, microstructural formation, and the number of potential α variants as possibly dictated by the variation of the thermal gradient in the build direction, subsequent cooling rates, and thermal annealing phenomena due to an elevated build chamber temperature, are mainly responsible for these anisotropic mechanical behaviors. For the horizontally built sample, positioned perpendicular to the build direction, being closer and sharing a larger cross-section to the build table should result in higher heat flow towards the build direction than the surrounding powders, as opposed to the vertical sample positioned parallel to the build direction during the solidification process. These phenomena of variations of heat flow direction and subsequent cooling rates potentially lead to the observed variation in the preferred grain orientation, microstructure formation, and grain distribution among the three different samples.

The vertical sample, being further away from the build plate, has larger grain sizes with a considerably different preferred grain orientation compared to the other two horizontal samples due to the assumedly considerable change in the thermal gradients, cooling rates, and thermal annealing phenomena. The horizontal sample, which shares a larger area with the build table, also showed a higher average grain boundary misorientation angle than the other two orientations. The maximum intensities of the alpha and beta pole-figure harmonic textures also change with the build orientations of the samples. The higher percentage of the softer β phases in the vertically built sample contributed to its higher ductility versus the other two orientations. Thus, the strong microstructural variation, as observed among EBM Ti6Al4V samples built in different orientations, mainly dictates the component performance and results in the anisotropic mechanical behaviors among different metal AM-built samples.

At high temperatures, Ti6Al4V parts are very sensitive to the strain rate. At a low strain rate of 0.005 mm/mm/min, this titanium sample shows substantial creep behavior, and the elongation becomes more than 50%. As a result, an optimized strain rate should be used to test this material in strain control mode at high temperatures to avoid this creeping behavior. During the ramping up of the temperature, considerable thermal expansion of the test fixtures and grips might happen to cause compressive stress on the specimens. This could be taken care of by continuously applying tensile force on the extension rods until thermal stability is obtained to prevent the test specimen from bending.

Furthermore, substantial temperature dependencies of the mechanical properties were observed for all EBM Ti6Al4V samples with three build orientations. The flow stress property decreases considerably with the increasing temperatures for all orientations. In higher temperatures, the strength of the alloy decreases while its ductility increases significantly. At 600°C temperature, significant softening behavior was observed, following a very short period of hardening behavior, until the fracture. These decreases in flow stress with the increasing temperature and softening behavior at high temperatures could be due to the increased dislocation mobility, which causes the dislocation density to be decreased, and dynamic recrystallization with grain boundary slip at the higher temperature.

The possible key softening mechanisms activated during tensile testing at 600°C temperature were the grain growth, dislocation motion caused by increased temperature, grain boundary slip, and coarsening of the alpha phase. There was no significant change in preferred grain orientation observed as the potential softening mechanism. However, the grain size increased significantly in all types of samples because of the combined interaction of the thermomechanical loading when tensile tested at different high temperatures. For example, in the case of the vertically built sample, the maximum initial grain size increased from 19 μm to 32 μm after tensile testing at 600°C temperature. When comparing the misorientation angles of different samples, both the number fraction of LAGBs (<15°) and HAGBs (>15°) decreases with increasing temperature except at angles greater than 55°. Thus, the average of misorientation angles decreases with increasing temperature accelerating the dislocation motion to the low energy region, thus making dislocation density decrease and making the materials softer. The maximum intensity of harmonic texture decreases from 6.27 to 2.79 for beta pole figures and increases from 7.04 to 12.32 for alpha pole figures with increasing temperature from 200°C to 600°C in the vertically built samples.

However, the preferred orientation of alpha grain doesn’t change considerably from the orientation of <0 0 0 1>, < 1 1 $\bar{2}$ 0> and < 1 1 $\bar{2}$ 1> orientations as the tensile testing temperature increases to 600°C from lower temperatures. Therefore, the change of the preferred grain orientations could be omitted here as a potential softening mechanism at this tested temperature range. But, this mechanism might get active when the deformation temperature is much higher and at the range of recrystallization temperature of either α-β or β phase field. Thus, the growth and coarsening of the alpha grains, change of average misorientation angle, and the maximum texture intensity of the alpha and beta phases, along with dislocation motion as triggered by the high temperature and grain boundary slip are some of the significant potential softening mechanisms which might get activated during high-temperature deformation of EBM-built Ti6Al4V samples. Similar, kind of softening mechanisms could get activated for other types of PBF-built metal parts as well. Therefore, necessary precautions and measures should be taken while using analogous kinds of metal parts in various high-temperature environments.

The fracture surfaces reveal that the samples with a loading direction parallel to the layers undergo cup-and-cone ductile fracture when the sample with the loading direction perpendicular to the layers experiences a ductile shear fracture. Most of the propagating cracks possibly initiate from the partially melted or unmelted powder particles near the sub-surface areas. Whereas various internal defects such as pores, keyholes, and un-melted powder zones could potentially accelerate the crack propagation. The flat-built and the side-built samples exhibit the cleavage mode of fracture where the tensile stress acts normal to the crystallographic cleavage plane. They both undergo intergranular fracture, where the crack propagates along the columnar grain boundaries. The top-built sample fracture surface appears highly fibrous due to a significant amount of plastic deformation before fracture. The fracture pattern, in this case, could be trans granular where the cracks propagate across the columnar grain. The fracture surface of the top-built sample tested at 600°C shows marks of grain boundary slip and dislocation slip, which might be responsible for the significant decrease in flow stress and increase of ductility for this sample.

The flat-built sample has a very poor porosity value (0.17%) with lower sphericity of defects which is sometimes very detrimental to their elongation properties, as opposed to the side-built and top-built samples, both having a porosity of 0.05%. Besides, Surface characterization of the as-built Ti-6Al-4V parts produced using the EBM additive manufacturing process is very crucial because this process is known to create parts with a rougher surface than the other AM processes. The main reason behind this higher surface roughness could be the greater average size of the powder (around 60 μm) used in this process. Surface roughness has also been found to vary depending on the build orientations. Surfaces parallel to the build direction have higher surface roughness than the surfaces perpendicular to the build direction. The perpendicular surfaces analyzed with the optical microscope show grooves along the width direction, which could be the scanning direction of the electron beam. Whereas there are round shape partially sintered powder particles on the parallel surfaces because of the deposition of a large number of powder layers on these surfaces, and since the heat conductivity is favorably larger towards the build table rather than the surrounding powder. However, the effect of the various inherent defects on the mechanical behavior is not that significant compared to their detrimental effect on various fatigue-critical applications.

The surface profile was measured using a stylus profiler on the surfaces parallel to the loading direction to capture defects perpendicular to this direction. The acquired profiles were then utilized to find the equivalent areas of the surface defects projected on a plane perpendicular to the maximum principal stress. Similarly, projected areas of internal defects were calculated from X-ray Computed tomography (CT) analysis results. These defect areas and Vickers hardness were then inputted into Murakami's $\sqrt{area}$ parameter model to find the fatigue strength at 10^7 cycles for various stress ratios. The fatigue limit measured from surface defects is found to be more crucial than those measured from internal defects, therefore, surface defects are rendered as determining factors for fatigue strength. Moreover, the fatigue strengths calculated using such predictive models agree reasonably well with the experimental values recorded in the literature, which are in the range of 150-350 MPa for as-built EBM Ti-6Al-4V samples without any post-treatment. It is also observed that the fatigue strength decreases with the increasing surface roughness. The mean stress also has a significant influence on fatigue properties. The fatigue strength decreases when the mean stress increases from zero to positive values.

Finally, the fatigue strength at 1000 cycles was approximated from fatigue limit calculation using Basquin's model. The maximum stress vs number of cycles to failure (S-N) curve, when plotted from 1000 to 10^7cycles, gives the linear regression model of the scatter of fatigue strength. When compared with the experimental S-N curves of EBM Ti-6Al-4V parts, the obtained estimated curve fitting shows quite good agreement. Therefore, this study predicted the maximum stress vs. fatigue life curve quantitatively by using the internal and external defect values and material hardness data when bypassing the tedious and destructive fatigue testing. The external defects are found to be more dominant than internal defects in determining the critical fatigue limit for as-built EBM AM parts.

CHAPTER 6

FUTURE WORK AND RECOMMENDATION

6.1 Modeling of Fatigue Crack Initiation and Propagation from Various Defects

Ti6Al4V being a sophisticated alloy, has various valuable applications in the aerospace, biomedical, and industrial sectors. Different powder bed fusion (PBF) additive manufacturing processes have proven to be excellent prospects lately for manufacturing near-net shape Ti6Al4V parts due to their poor machinability in conventional removal techniques [32]. However, various powder bed fusion (PBF) process-built Ti6Al4V parts are known to have various internal defects, like lack of fusion (LOF) porosity, keyhole porosity, and entrapped gas porosity [30,63–66]. LOF porosity occurs due to insufficient energy density, whereas keyhole porosity builds up along the scanning path because of excessive energy density. The gas porosity originates from the trapped argon in powder feedstock during the atomization process and from the water vapor on the powder surface as hydrogen pores. All these porosities are detrimental to the fatigue performance of the PBF parts. The surface defects were found to be more critical to the fatigue performance as compared to the internal defects, via numerical and analytical study in the earlier sections. A further computational analysis using finite element analysis (FEA) can be conducted to explore the issue in more detail.

In the future study, an FEA modeling of fatigue crack initiation and propagation from inherent defects of as-built EBM Ti6Al4V parts will be attempted. The microstructural finite element (FE) simulation of fatigue failure could be approached by a global-local model scheme to lessen the computational time and facilitate the microstructural defect features [73]. The global FE model for simulating cyclic fatigue loading will be developed using the material's elastic and plastic properties. Furthermore, a local model representing a portion of the global model will be built with distributed defects throughout the element, as shown in **Figure 59**. Eventually, a continuum damage modeling approach, for example, successive initiation, will be used for predicting crack initiation sites and propagation directions. In the successive initiation model approach, the damages accumulate continually in elements under cyclic loading. A failure criterion is applied to the elements. When an element reaches the failure criterion, it is eliminated from the structure by reducing its stiffness closer to the stiffness of air. Finally, when the damage accumulation reaches a threshold value, then the fatigue crack initiates and propagates from those critically damaged elements. In successive initiation under cyclic loading, the number of cycles to failures can be predicted using the Coffin-Mansion damage model as a function of plastic strain amplitude [143]. All the elements that have fatigue life less than a threshold value will work a crack initiation sites.

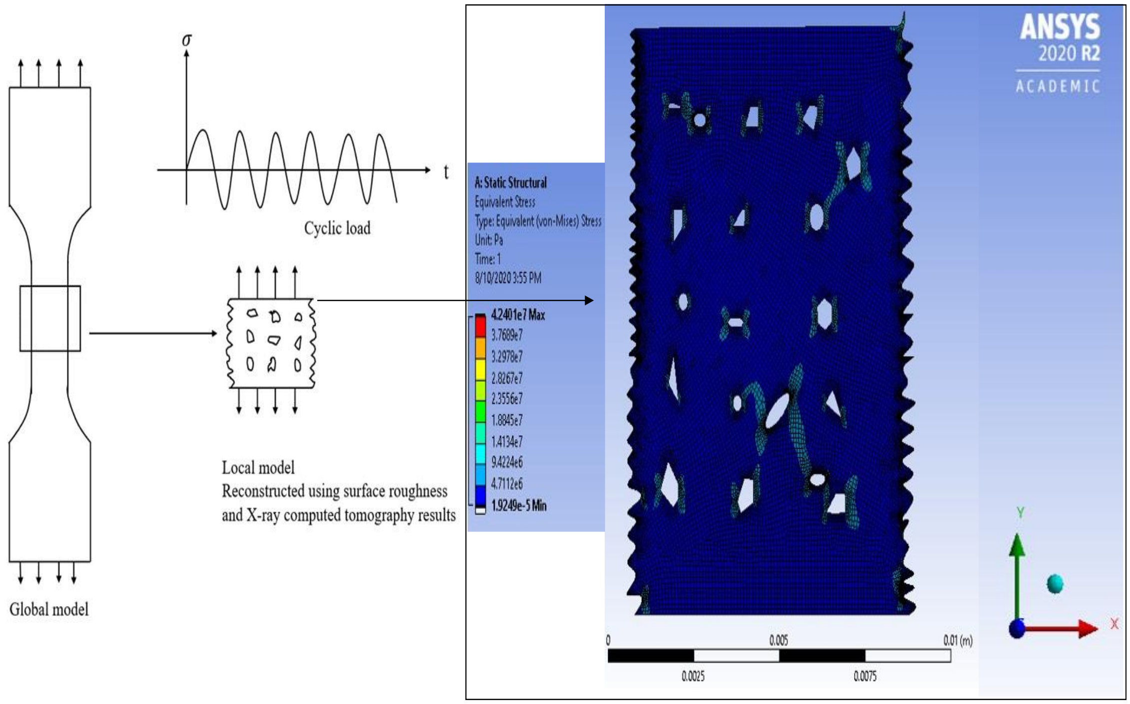

Equivalent (von -Mises) Stress Distribution

Figure 59 Global-local modeling of fatigue failure for as-built EBM Ti6Al4V parts

Therefore, the fatigue crack initiation sites from the inherent defects and the number of cycles for crack initiation (N_I) can be identified using continuum damage mechanics (CDM) models. After that, the number of cycles for crack propagation (N_P) can be identified using linear elastic fracture mechanics (LEFM) based on crack growth concepts, for example, Paris – Erdogan law [144]. Finally, the total fatigue life (N_T) of the as-built Ti6Al4V parts can be determined from the summation of the crack initiation and propagation periods.

6.2 Determining High-Temperature (Greater Than 600°C) Mechanical Properties of PBF AM Built Metal Parts

In the current study, the high-temperature mechanical properties of EB-PBF built Ti6Al4V parts have been analyzed up to 600°C temperature. But, many of these metal parts can be used even at a higher temperature than at 1100°C temperature, such as in heat exchangers, gas turbine rotors and stator blades, and nuclear reactors. Therefore, analyzing the mechanical properties at higher temperatures is also very important. Further experiments should be designed to obtain properties at those higher temperatures. However, at temperatures more than 600°C various issues such as accelerated oxidation of the metals, creeping due to higher might need to be considered as well along with other failure mechanisms such as thermal softening due to DRX and DRV. Further, microstructural and fractography analysis would be needed to confirm these mechanisms and identify further inherent failure mechanisms that get activated at those higher temperatures.

In this study, only EBM AM-produced Ti6Al4V alloy has been analyzed only. Other commonly used metal alloys such as Inconel 718, stainless steel alloy (SS 316L, SS 304L), CoCrMo, and AlSi10Mg [145,146] can be investigated similarly to understand the generalized high temperature of tensile and fatigue failures mechanics and related underlying physics. The fatigue performances of the EBM Ti6Al4V alloy have been analyzed considering only the mechanical cyclic loading. Similarly, cyclic thermal loading can also be considered along with mechanical loading in future studies.

Creating a realistic high-temperature environment for tensile testing might be very difficult in many cases. The modeling and simulation, utilizing the available computational power, could be efficient alternatives for those difficult experimental setups, in obtaining the best possible insight, given that similar kind of application of these metals under various critical conditions.

Though cyclic fatigue testing could be very monotonous and time-consuming, obtaining experimental fatigue data for use in subsequent analytical and computation studies would provide a better understanding and more accurate scenarios of the various physical phenomena responsible for the real-time performances of various structural components.

6.3 Analyzing the Aging Effect

The samples analyzed in this study were produced almost seven years ago from the time when they were tested. This time gap can lead to some aging in the sample, making some inherent unwanted changes in them. For example, this could potentially change some behaviors, including the possibility of the formation of oxides or other intermetallics in the material. Therefore, the effect of aging on the mechanical properties of the sample could be another research gap that needs to be addressed properly to gain a detail understating of the performances of different metals produced by the different PBF additive manufacturing processes.

6.4 Process Parameter Optimization of Different PBF AM Process

Though, a large number of studies have been conducted and currently going on to make the PBF AM processes acceptable and highly adopted across the industries. There are some issues that still need to be solved to make additive manufacturing a suitable choice for bulk manufacturing of functional equipment components. The various manufactured-induced defects are one of those major issues. These defects could be further minimized through the incorporation of artificial intelligence (AI) and machine learning for analyzing the myriad of data produced as a by-product during the manufacturing and post-processing of the various parts. Furthermore, in-situ monitoring and proving control loop feedback (via high-speed camera, ultrasound techniques, etc.) could be another convenient way for process parameter optimization and subsequently minimizing the carious inherent defects. The infographics of the proposed plan for the process parameter optimization of different metal AM process is shown in **Figure 60** as follows.

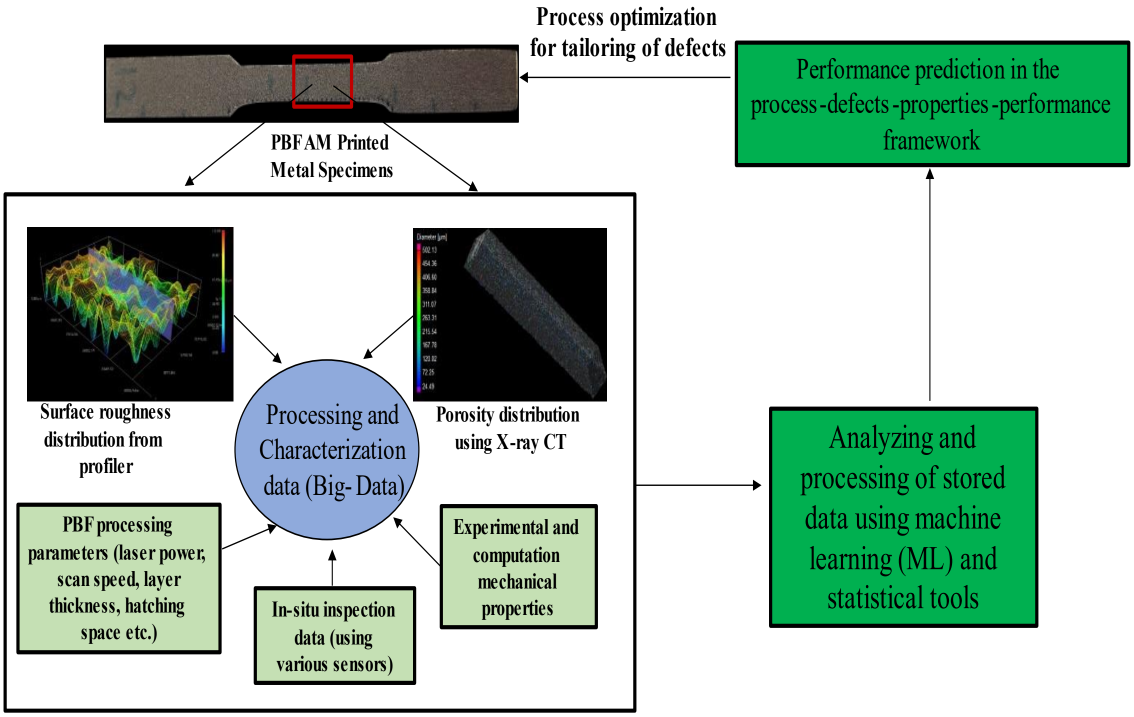

Figure 60 Infographics of the proposed plan for the process parameter optimization of different PBF AM process

REFERENCES

[1] A. Bandyopadhyay, S. Bose, Additive Manufacturing, Second Edition -CRC Press, Taylor & Francis Group, Boca Raton, FL, 2020, in: n.d.

[2] M. Attaran, The rise of 3-D printing: The advantages of additive manufacturing over traditional manufacturing, Bus. Horiz. 60 (2017) 677–688. https://doi.org/10.1016/j.bushor.2017.05.011.

[3] C.K. Chua, C.H. Wong, W.Y. Yeong, Standards, Quality Control, and Measurement Sciences in 3D Printing and Additive Manufacturing, 1st Edition, Academic Press, Elsevier, Cambridge, MA, Pages 95-137, 2017. https://doi.org/10.1016/b978-0-12-813489-4.00005-2.

[4] T.D. Ngo, A. Kashani, G. Imbalzano, K.T.Q. Nguyen, D. Hui, Additive manufacturing (3D printing): A review of materials, methods, applications and challenges, Compos. Part B Eng. 143 (2018) 172–196. https://doi.org/10.1016/j.compositesb.2018.02.012.

[5] K. V. Wong, A. Hernandez, A Review of Additive Manufacturing, ISRN Mech. Eng. 2012 (2012) 1–10. https://doi.org/10.5402/2012/208760.

[6] J.C. Najmon, S. Raeisi, A. Tovar, Review of additive manufacturing technologies and applications in the aerospace industry, Elsevier Inc., 2019. https://doi.org/10.1016/b978-0-12-814062-8.00002-9.

[7] L.E. Murr, S.M. Gaytan, D.A. Ramirez, E. Martinez, J. Hernandez, K.N. Amato, P.W. Shindo, F.R. Medina, R.B. Wicker, Metal Fabrication by Additive Manufacturing Using Laser and Electron Beam Melting Technologies, J. Mater. Sci. Technol. 28 (2012) 1–14. https://doi.org/10.1016/S1005-0302(12)60016-4.

[8] W.E. Frazier, Metal additive manufacturing: A review, J. Mater. Eng. Perform. 23 (2014) 1917–1928. https://doi.org/10.1007/s11665-014-0958-z.

[9] R. Liu, Z. Wang, T. Sparks, F. Liou, J. Newkirk, Aerospace applications of laser additive manufacturing, Elsevier Ltd, 2016. https://doi.org/10.1016/B978-0-08-100433-3.00013-0.

[10] F. Ahsan, L. Ladani, Temperature Profile, Bead Geometry, and Elemental Evaporation in Laser Powder Bed Fusion Additive Manufacturing Process, Jom. 72 (2020) 429–439. https://doi.org/10.1007/s11837-019-03872-3.

[11] R. Stephens, R.R. Stephens, H. Fuchs, METAL FATIGUE Second Edition, 2001.

[12] Application field Additive Manufacturing, or 3D Printing - Simufact software solutions, (n.d.). https://www.simufact.com/additive-manufacturing.html (accessed April 23, 2022).

[13] Arcam EBM_Spectra H_Machine | GE Additive, (n.d.). https://www.ge.com/additive/additive-manufacturing/machines/ebm-machines/arcam-ebm-spectra-h (accessed April 23, 2022).

[14] G. Lütjering, J.C. Williams, Titanium, 2nd Edition, 2003. https://doi.org/10.1017/CBO9781107415324.004.

[15] L. Roy, Variation in Mechanical Behavior due to DIifferent Build Directions of Ti6Al4V Fabricated By Electron Beam, (2013). http://acumen.lib.ua.edu/content/u0015/0000001/0001427/u0015_0000001_0001427.pdf.

[16] http://www.arcam.com/wp-content/uploads/Arcam-Ti6Al4V-Titanium-Alloy.pdf, (n.d.). www.arcam.comArcamEBMsystemTi6Al4VTitaniumAlloy (accessed March 4, 2020).

[17] H.K. Rafi, N. V. Karthik, H. Gong, T.L. Starr, B.E. Stucker, Microstructures and mechanical properties of Ti6Al4V parts fabricated by selective laser melting and electron beam melting, J. Mater. Eng. Perform. 22 (2013) 3872–3883. https://doi.org/10.1007/s11665-013-0658-0.

[18] T.D. Ngo, A. Kashani, G. Imbalzano, K.T.Q. Nguyen, D. Hui, Additive manufacturing (3D printing): A review of materials, methods, applications and challenges, Compos. Part B Eng. 143 (2018) 172–196. https://doi.org/10.1016/j.compositesb.2018.02.012.

[19] http://www.arcam.com/wp-content/uploads/Arcam-Ti6Al4V-Titanium-Alloy.pdf, (n.d.). http://www.arcam.com/wp-content/uploads/Arcam-Ti6Al4V-Titanium-Alloy.pdf (accessed March 12, 2020).

[20] S. Rawal, J. Brantley, N. Karabudak, Additive manufacturing of Ti-6Al-4V alloy components for spacecraft applications, RAST 2013 - Proc. 6th Int. Conf. Recent Adv. Sp. Technol. (2013) 5–11. https://doi.org/10.1109/RAST.2013.6581260.

[21] V. Chastand, P. Quaegebeur, W. Maia, E. Charkaluk, Comparative study of fatigue properties of Ti-6Al-4V specimens built by electron beam melting (EBM) and selective laser melting (SLM), Mater. Charact. 143 (2018) 76–81. https://doi.org/10.1016/j.matchar.2018.03.028.

[22] W.S. Lee, C.F. Lin, Plastic deformation and fracture behaviour of Ti-6Al-4V alloy

loaded with high strain rate under various temperatures, Mater. Sci. Eng. A. 241 (1998) 48–59.

[23] J. Kim, K.H. Kim, D. Kwon, Evaluation of high-temperature tensile properties of Ti-6Al-4V using instrumented indentation testing, Met. Mater. Int. 22 (2016) 209–215. https://doi.org/10.1007/s12540-016-5619-3.

[24] S. Kumar, T.S.N. Sankara Narayanan, S. Ganesh Sundara Raman, S.K. Seshadri, Thermal oxidation of Ti6Al4V alloy: Microstructural and electrochemical characterization, Mater. Chem. Phys. 119 (2010) 337–346. https://doi.org/10.1016/j.matchemphys.2009.09.007.

[25] Arcam, Arcam-Ti6Al4V-Titanium-Alloy, (n.d.). http://www.arcam.com/wp-content/uploads/Arcam-Ti6Al4V-Titanium-Alloy.pdf.

[26] A. Safdar, Microstructures and Surface Roughness of EBM Produced Ti-6A1-4V, 2010.

[27] J. Günther, D. Krewerth, T. Lippmann, S. Leuders, T. Tröster, A. Weidner, H. Biermann, T. Niendorf, Fatigue life of additively manufactured Ti–6Al–4V in the very high cycle fatigue regime, Int. J. Fatigue. 94 (2017) 236–245. https://doi.org/10.1016/j.ijfatigue.2016.05.018.

[28] D. Herzog, V. Seyda, E. Wycisk, C. Emmelmann, Acta Materialia Additive manufacturing of metals, Acta Mater. 117 (2016) 371–392. https://doi.org/10.1016/j.actamat.2016.07.019.

[29] L. Ladani, J. Razmi, S.F. Choudhury, Mechanical anisotropy and strain rate dependency behavior of Ti6Al4V produced using E-beam additive fabrication, J. Eng. Mater. Technol. Trans. ASME. 136 (2014). https://doi.org/10.1115/1.4027729.

[30] X. Zhou, N. Dai, M. Chu, L. Wang, D. Li, L. Zhou, X. Cheng, X-ray CT analysis of the influence of process on defect in Ti-6Al-4V parts produced with Selective Laser Melting technology, Int. J. Adv. Manuf. Technol. 106 (2020) 3–14. https://doi.org/10.1007/s00170-019-04347-0.

[31] C. Körner, Additive manufacturing of metallic components by selective electron beam melting - A review, Int. Mater. Rev. 61 (2016) 361–377. https://doi.org/10.1080/09506608.2016.1176289.

[32] P. Nandwana, Y. Lee, Influence of scan strategy on porosity and microstructure of Ti-6Al-4V fabricated by electron beam powder bed fusion, Mater. Today Commun. 24 (2020) 100962. https://doi.org/10.1016/j.mtcomm.2020.100962.

[33] W. Xu, E.W. Lui, A. Pateras, M. Qian, M. Brandt, In situ tailoring microstructure in additively manufactured Ti-6Al-4V for superior mechanical performance, Acta Mater. 125 (2017) 390–400. https://doi.org/10.1016/j.actamat.2016.12.027.

[34] H. Ali, L. Ma, H. Ghadbeigi, K. Mumtaz, In-situ residual stress reduction, martensitic decomposition and mechanical properties enhancement through high temperature powder bed pre-heating of Selective Laser Melted Ti6Al4V, Mater. Sci. Eng. A. 695 (2017) 211–220. https://doi.org/10.1016/j.msea.2017.04.033.

[35] G.M. Bilgin, Z. Esen, Ş.K. Akın, A.F. Dericioglu, Optimization of the mechanical properties of Ti-6Al-4V alloy fabricated by selective laser melting using thermohydrogen processes, Mater. Sci. Eng. A. 700 (2017) 574–582. https://doi.org/10.1016/j.msea.2017.06.016.

[36] T. Persenot, G. Martin, R. Dendievel, J.Y. Buffiére, E. Maire, Enhancing the tensile properties of EBM as-built thin parts: Effect of HIP and chemical etching, Mater. Charact. 143 (2018) 82–93. https://doi.org/10.1016/j.matchar.2018.01.035.

[37] D. Foehring, H. Chew, J. Lambros, Materials Science & Engineering A Characterizing the tensile behavior of additively manufactured Ti-6Al-4V using multiscale digital image correlation, Mater. Sci. Eng. A. 724 (2018) 536–546. https://doi.org/10.1016/j.msea.2018.03.091.

[38] L. Facchini, E. Magalini, P. Robotti, A. Molinari, S. Höges, K. Wissenbach, Ductility of a Ti-6Al-4V alloy produced by selective laser melting of prealloyed powders, Rapid Prototyp. J. 16 (2010) 450–459. https://doi.org/10.1108/13552541011083371.

[39] I. Yadroitsev, P. Krakhmalev, I. Yadroitsava, A. Du Plessis, Qualification of Ti6Al4V ELI Alloy Produced by Laser Powder Bed Fusion for Biomedical Applications, Jom. 70 (2018) 372–377. https://doi.org/10.1007/s11837-017-2655-5.

[40] X. Wang, K. Chou, EBSD study of beam speed effects on Ti-6Al-4V alloy by powder bed electron beam additive manufacturing, J. Alloys Compd. 748 (2018) 236–244. https://doi.org/10.1016/j.jallcom.2018.03.173.

[41] A.A. Antonysamy, J. Meyer, P.B. Prangnell, Effect of build geometry on the β-grain structure and texture in additive manufacture of Ti6Al4V by selective electron beam melting, Mater. Charact. 84 (2013) 153–168. https://doi.org/10.1016/j.matchar.2013.07.012.

[42] C. de Formanoir, S. Michotte, O. Rigo, L. Germain, S. Godet, Electron beam melted Ti-6Al-4V: Microstructure, texture and mechanical behavior of the as-built

and heat-treated material, Mater. Sci. Eng. A. 652 (2016) 105–119. https://doi.org/10.1016/j.msea.2015.11.052.

[43] S.S. Al-Bermani, M.L. Blackmore, W. Zhang, I. Todd, The origin of microstructural diversity, texture, and mechanical properties in electron beam melted Ti-6Al-4V, Metall. Mater. Trans. A Phys. Metall. Mater. Sci. 41 (2010) 3422–3434. https://doi.org/10.1007/s11661-010-0397-x.

[44] X. Tan, Y. Kok, Y.J. Tan, G. Vastola, Q.X. Pei, G. Zhang, Y.W. Zhang, S.B. Tor, K.F. Leong, C.K. Chua, An experimental and simulation study on build thickness dependent microstructure for electron beam melted Ti-6Al-4V, J. Alloys Compd. 646 (2015) 303–309. https://doi.org/10.1016/j.jallcom.2015.05.178.

[45] L. Ladani, Local and Global Mechanical Behavior and Microstructure of Ti6Al4V Parts Built Using Electron Beam Melting Technology, Metall. Mater. Trans. A Phys. Metall. Mater. Sci. 46 (2015) 3835–3841. https://doi.org/10.1007/s11661-015-2965-6.

[46] B.E. Carroll, T.A. Palmer, A.M. Beese, Anisotropic tensile behavior of Ti-6Al-4V components fabricated with directed energy deposition additive manufacturing, Acta Mater. 87 (2015) 309–320. https://doi.org/10.1016/j.actamat.2014.12.054.

[47] Y.Y. Zong, D.B. Shan, Y. Lü, B. Guo, Effect of 0.3 wt%H addition on the high temperature deformation behaviors of Ti-6Al-4V alloy, Int. J. Hydrogen Energy. 32 (2007) 3936–3940. https://doi.org/10.1016/j.ijhydene.2007.04.032.

[48] J.H. Zhu, P.K. Liaw, J.M. Corum, H.E. McCoy, High-temperature mechanical behavior of Ti-6Al-4V alloy and TiCp/Ti-6AI-4V composite, Metall. Mater. Trans. A Phys. Metall. Mater. Sci. 30 (1999) 1569–1578. https://doi.org/10.1007/s11661-999-0094-9.

[49] S. Nagarjuna, M. Srinivas, High temperature tensile behaviour of a Cu-1.5 wt.% Ti alloy, Mater. Sci. Eng. A. 335 (2002) 89–93. https://doi.org/10.1016/S0921-5093(01)01945-1.

[50] C.T. Yang, Y.C. Lu, C.H. Koo, The high temperature tensile properties and microstructural analysis of Ti-40Al-15Nb alloy, Intermetallics. 10 (2002) 161–169. https://doi.org/10.1016/S0966-9795(01)00123-6.

[51] D. Liu, S.Q. Zhang, A. Li, H.M. Wang, High temperature mechanical properties of a laser melting deposited TiC/TA15 titanium matrix composite, J. Alloys Compd. 496 (2010) 189–195. https://doi.org/10.1016/j.jallcom.2010.02.120.

[52] S.H. Wang, M.D. Wei, L.W. Tsay, Tensile properties of LBW welds in Ti-6Al-4V

alloy at evaluated temperatures below 450 °C, Mater. Lett. 57 (2003) 1815–1823. https://doi.org/10.1016/S0167-577X(02)01074-1.

[53] R. Ding, Z.X. Guo, A. Wilson, Microstructural evolution of a Ti-6Al-4V alloy during thermomechanical processing, Mater. Sci. Eng. A. 327 (2002) 233–245. https://doi.org/10.1016/S0921-5093(01)01531-3.

[54] L. He, A. Dehghan-Manshadi, R.J. Dippenaar, The evolution of microstructure of Ti-6Al-4V alloy during concurrent hot deformation and phase transformation, Mater. Sci. Eng. A. 549 (2012) 163–167. https://doi.org/10.1016/j.msea.2012.04.025.

[55] X. Wang, L. Wang, L.S. Luo, X.D. Liu, Y.C. Tang, X.Z. Li, R.R. Chen, Y.Q. Su, J.J. Guo, H.Z. Fu, Hot deformation behavior and dynamic recrystallization of melt hydrogenated Ti-6Al-4V alloy, J. Alloys Compd. 728 (2017) 709–718. https://doi.org/10.1016/j.jallcom.2017.09.044.

[56] Q. Bai, J. Lin, T.A. Dean, D.S. Balint, T. Gao, Z. Zhang, Modelling of dominant softening mechanisms for Ti-6Al-4V in steady state hot forming conditions, Mater. Sci. Eng. A. 559 (2013) 352–358. https://doi.org/10.1016/j.msea.2012.08.110.

[57] C.H. Park, J.H. Kim, Y.T. Hyun, J.T. Yeom, N.S. Reddy, The origins of flow softening during higherature deformation of a Ti-6Al-4V alloy with a lamellar microstructure, J. Alloys Compd. 582 (2014) 126–129. https://doi.org/10.1016/j.jallcom.2013.08.041.

[58] P.M. Souza, P.D. Hodgson, B. Rolfe, R.P. Singh, H. Beladi, Effect of initial microstructure and beta phase evolution on dynamic recrystallization behaviour of Ti6Al4V alloy - An EBSD based investigation, J. Alloys Compd. 793 (2019) 467–479. https://doi.org/10.1016/j.jallcom.2019.04.183.

[59] S. Zherebtsov, M. Murzinova, G. Salishchev, S.L. Semiatin, Spheroidization of the lamellar microstructure in Ti-6Al-4V alloy during warm deformation and annealing, Acta Mater. 59 (2011) 4138–4150. https://doi.org/10.1016/j.actamat.2011.03.037.

[60] B. Babu, L.E. Lindgren, Dislocation density based model for plastic deformation and globularization of Ti-6Al-4V, Int. J. Plast. 50 (2013) 94–108. https://doi.org/10.1016/j.ijplas.2013.04.003.

[61] I. Weiss, F.H. Froes, D. Eylon, G.E. Welsch, Modification of alpha morphology in Ti-6Al-4V by thermomechanical processing, Metall. Trans. A. 17 (1986) 1935–1947. https://doi.org/10.1007/BF02644991.

[62] N. Stefansson, S.L. Semiatin, Mechanisms of globularization of Ti-6Al-4V during static heat treatment, Metall. Mater. Trans. A Phys. Metall. Mater. Sci. 34 A (2003) 691–698. https://doi.org/10.1007/s11661-003-0103-3.

[63] S. Martínez-Pellitero, M.A. Castro, A.I. Fernández-Abia, S. González, E. Cuesta, Analysis of influence factors on part quality in micro-SLA technology, Procedia Manuf. 13 (2017) 856–863. https://doi.org/10.1016/j.promfg.2017.09.143.

[64] A. du Plessis, Effects of process parameters on porosity in laser powder bed fusion revealed by X-ray tomography, Addit. Manuf. 30 (2019) 100871. https://doi.org/10.1016/j.addma.2019.100871.

[65] Y.S. Lee, M.M. Kirka, R.B. Dinwiddie, N. Raghavan, J. Turner, R.R. Dehoff, S.S. Babu, Role of scan strategies on thermal gradient and solidification rate in electron beam powder bed fusion, Addit. Manuf. 22 (2018) 516–527. https://doi.org/10.1016/j.addma.2018.04.038.

[66] G. Vastola, Q.X. Pei, Y.W. Zhang, Predictive model for porosity in powder-bed fusion additive manufacturing at high beam energy regime, Addit. Manuf. 22 (2018) 817–822. https://doi.org/10.1016/j.addma.2018.05.042.

[67] A. du Plessis, I. Yadroitsava, I. Yadroitsev, Effects of defects on mechanical properties in metal additive manufacturing: A review focusing on X-ray tomography insights, Mater. Des. 187 (2020) 108385. https://doi.org/10.1016/j.matdes.2019.108385.

[68] A.B. Spierings, T.L. Starr, K. Wegener, Fatigue performance of additive manufactured metallic parts, Rapid Prototyp. J. 19 (2013) 88–94. https://doi.org/10.1108/13552541311302932.

[69] P. Li, D.H. Warner, A. Fatemi, N. Phan, Critical assessment of the fatigue performance of additively manufactured Ti-6Al-4V and perspective for future research, Int. J. Fatigue. 85 (2016) 130–143. https://doi.org/10.1016/j.ijfatigue.2015.12.003.

[70] S. Romano, A. Brückner-Foit, A. Brandão, J. Gumpinger, T. Ghidini, S. Beretta, Fatigue properties of AlSi10Mg obtained by additive manufacturing: Defect-based modelling and prediction of fatigue strength, Eng. Fract. Mech. 187 (2018) 165–189. https://doi.org/10.1016/j.engfracmech.2017.11.002.

[71] E. Beevers, A.D. Brandão, J. Gumpinger, M. Gschweitl, C. Seyfert, P. Hofbauer, T. Rohr, T. Ghidini, Fatigue properties and material characteristics of additively manufactured AlSi10Mg – Effect of the contour parameter on the microstructure, density, residual stress, roughness and mechanical properties, Int. J. Fatigue. 117

(2018) 148–162. https://doi.org/10.1016/j.ijfatigue.2018.08.023.

[72] M. Benedetti, E. Torresani, M. Leoni, V. Fontanari, M. Bandini, C. Pederzolli, C. Potrich, The effect of post-sintering treatments on the fatigue and biological behavior of Ti-6Al-4V ELI parts made by selective laser melting, J. Mech. Behav. Biomed. Mater. 71 (2017) 295–306. https://doi.org/10.1016/j.jmbbm.2017.03.024.

[73] S. Nelson, L. Ladani, T. Topping, E. Lavernia, Fatigue and monotonic loading crack nucleation and propagation in bimodal grain size aluminum alloy, Acta Mater. 59 (2011) 3550–3570. https://doi.org/10.1016/j.actamat.2011.02.029.

[74] L.J. Ladani, J. Razmi, Probabilistic design approach for cyclic fatigue life prediction of microelectronic interconnects, IEEE Trans. Adv. Packag. 33 (2010) 559–568. https://doi.org/10.1109/TADVP.2010.2040734.

[75] A. Ramanathan, J. Moverare, N. Dixit, R. Pederson, Materials Science & Engineering A In fl uence of defects and as-built surface roughness on fatigue properties of additively manufactured Alloy 718, 735 (2018) 463–474. https://doi.org/10.1016/j.msea.2018.08.072.

[76] S. Liu, Y.C. Shin, Additive manufacturing of Ti6Al4V alloy: A review, Mater. Des. 164 (2019) 107552. https://doi.org/10.1016/j.matdes.2018.107552.

[77] V. Chastand, P. Quaegebeur, W. Maia, E. Charkaluk, Materials Characterization Comparative study of fatigue properties of Ti-6Al-4V specimens built by electron beam melting (EBM) and selective laser melting (SLM), 143 (2018) 76–81. https://doi.org/10.1016/j.matchar.2018.03.028.

[78] D. Greitemeier, C.D. Donne, F. Syassen, J. Eufinger, T. Melz, D. Greitemeier, C.D. Donne, F. Syassen, J. Eufinger, T. Melz, Effect of surface roughness on fatigue performance of additive manufactured Ti – 6Al – 4V Effect of surface roughness on fatigue performance of additive manufactured Ti – 6Al – 4V, 0836 (2016). https://doi.org/10.1179/1743284715Y.0000000053.

[79] B. Vayssette, N. Saintier, C. Brugger, M. Elmay, E. Pessard, Surface roughness of Ti-6Al-4V parts obtained by SLM and EBM: Effect on the High Cycle Fatigue life, Procedia Eng. 213 (2018) 89–97. https://doi.org/10.1016/j.proeng.2018.02.010.

[80] F.E.I. Cao, T. Zhang, M.A. Ryder, D.A. Lados, A Review of the Fatigue Properties of Additively Manufactured Ti-6Al-4V, JOM. 70 (2018) 349–357. https://doi.org/10.1007/s11837-017-2728-5.

[81] M. Kahlin, H. Ansell, J.J. Moverare, Fatigue behaviour of notched additive

manufactured Ti6Al4V with as-built surfaces, Int. J. Fatigue. 101 (2017) 51–60. https://doi.org/10.1016/j.ijfatigue.2017.04.009.

[82] A. Uriondo, M. Esperon-Miguez, S. Perinpanayagam, The present and future of additive manufacturing in the aerospace sector: A review of important aspects, Proc. Inst. Mech. Eng. Part G J. Aerosp. Eng. 229 (2015) 2132–2147. https://doi.org/10.1177/0954410014568797.

[83] P. Aliprandi, F. Giudice, E. Guglielmino, A. Sili, Tensile and creep properties improvement of Ti-6Al-4V alloy specimens produced by electron beam powder bed fusion additive manufacturing, Metals (Basel). 9 (2019) 1–22. https://doi.org/10.3390/met9111207.

[84] M. Shunmugavel, A. Polishetty, G. Littlefair, Microstructure and Mechanical Properties of Wrought and Additive Manufactured Ti-6Al-4V Cylindrical Bars, Procedia Technol. 20 (2015) 231–236. https://doi.org/10.1016/j.protcy.2015.07.037.

[85] S. Lampman, A.S.M. International, Wrought Titanium and Titanium Alloys, Prop. Sel. Nonferrous Alloy. Spec. Mater. 2 (2018) 592–633. https://doi.org/10.31399/asm.hb.v02.a0001081.

[86] T. Grimm, G. Wiora, G. Witt, Characterization of typical surface effects in additive manufacturing with confocal microscopy, Surf. Topogr. Metrol. Prop. 3 (2015). https://doi.org/10.1088/2051-672X/3/1/014001.

[87] G. Strano, L. Hao, R.M. Everson, K.E. Evans, Surface roughness analysis, modelling and prediction in selective laser melting, J. Mater. Process. Technol. 213 (2013) 589–597. https://doi.org/10.1016/j.jmatprotec.2012.11.011.

[88] L. Ladani, M. Sadeghilaridjani, Review of powder bed fusion additive manufacturing for metals, Metals (Basel). 11 (2021). https://doi.org/10.3390/met11091391.

[89] L. Ladani, Additive Manufacturing of Metals, Materials, Processes, Tests andd Standards, Destech Publ. (2020) 251 pages. https://doi.org/10.1016/j.solener.2019.02.027%0Ahttps://www.golder.com/insights/block-caving-a-viable-alternative/%0A??? (accessed October 31, 2021).

[90] Y. Murakami, Metal Fatigue: Effects of Small Defects and Nonmetallic Inclusions - 1st Edition, (2019). https://www.elsevier.com/books/metal-fatigue-effects-of-small-defects-and-nonmetallic-inclusions/murakami/978-0-08-044064-4%0Ahttp://files/407/978-0-08-044064-4.html (accessed January 30, 2020).

[91] ASTM International E8/E8M-16ae1 Standard Test Methods for Tension Testing of Metallic Materials. West Conshohocken, PA; ASTM International, 2016. doi: https://doi.org/10.1520/E0008_E0008M-16AE01, Astm. (2014) 1–28. https://doi.org/10.1520/E0008.

[92] Arcam AB, Electron Beam Melting - EBM Process, Additive Manufacturing | Arcam AB, ArcamEBM. (2017). http://www.arcam.com/technology/electron-beam-melting/ (accessed September 19, 2019).

[93] L. Ladani, L. Roy, Mechanical behavior of Ti-6Al-4V manufactured by electron beam additive fabrication, ASME 2013 Int. Manuf. Sci. Eng. Conf. Collocated with 41st North Am. Manuf. Res. Conf. MSEC 2013. 1 (2013) 1–5. https://doi.org/10.1115/MSEC2013-1105.

[94] X. Wang, X. Gong, K. Chou, Scanning Speed Effect on Mechanical Properties of Ti-6Al-4V Alloy Processed by Electron Beam Additive Manufacturing, Procedia Manuf. 1 (2015) 287–295. https://doi.org/10.1016/j.promfg.2015.09.026.

[95] M.J. Mian, J. Razmi, L. Ladani, Mechanical behavior of electron beam powder bed fusion additively manufactured Ti6Al4V parts at elevated temperatures, J. Manuf. Sci. Eng. Trans. ASME. 143 (2021) 1–12. https://doi.org/10.1115/1.4049092.

[96] High Speed Steel | H13 Steel | H13 | H13 Technical Data, (n.d.). https://www.hudsontoolsteel.com/technical-data/steelH3 (accessed June 18, 2020).

[97] Tool Steel H13 | Metal Supermarkets - Steel, Aluminum, Stainless, Hot-Rolled, Cold-Rolled, Alloy, Carbon, Galvanized, Brass, Bronze, Copper, (n.d.). https://www.metalsupermarkets.com/metals/tool-steel/tool-steel-h13/ (accessed June 18, 2020).

[98] J.C. Benedyk, High Performance Alloys Database - Example H13, (2008) 135.

[99] A. Schmieder, Measuring the Apparatus Contribution to Bending in Tension Specimens, in: Elev. Temp. Test. Probl. Areas, ASTM International, 2009: pp. 15-15–28. https://doi.org/10.1520/stp26903s.

[100] NDT Resource Center, Property Modification - Strengthening/Hardening Mechanisms, (2019). https://www.nde-ed.org/EducationResources/CommunityCollege/Materials/Structure/strengthening.htm (accessed November 27, 2019).

[101] G.E. DIETER, MECHANICAL METALLURGY, 2012. https://doi.org/10.1093/oxfordhb/9780199238828.013.0020.

[102] X. Gong, T. Anderson, K. Chou, Review on powder-based electron beam additive manufacturing Technology, Manuf. Rev. 1 (2014) 1–9. https://doi.org/10.1051/mfreview/2014001.

[103] S. Wei, P. Deng, Q. Jiangtong, Y. Jin, Tensile deformation behavior of Ti-6Al-4V sheet at elevated temperature, Mater. Res. Express. 6 (2019). https://doi.org/10.1088/2053-1591/ab4b83.

[104] R. Soc, G. Britain, Recrystallization of metals during hot deformation, Philos. Trans. R. Soc. London. Ser. A, Math. Phys. Sci. 288 (1978) 147–158. https://doi.org/10.1098/rsta.1978.0010.

[105] G.Z. Quan, G.C. Luo, J.T. Liang, D. Sen Wu, A. Mao, Q. Liu, Modelling for the dynamic recrystallization evolution of Ti-6Al-4V alloy in two-phase temperature range and a wide strain rate range, Comput. Mater. Sci. 97 (2015) 136–147. https://doi.org/10.1016/j.commatsci.2014.10.009.

[106] Z.X. Zhang, S.J. Qu, A.H. Feng, J. Shen, D.L. Chen, Hot deformation behavior of Ti-6Al-4V alloy: Effect of initial microstructure, J. Alloys Compd. 718 (2017) 170–181. https://doi.org/10.1016/j.jallcom.2017.05.097.

[107] E. Ghasemi, A. Zarei-Hanzaki, E. Farabi, K. Tesař, A. Jäger, M. Rezaee, Flow softening and dynamic recrystallization behavior of BT9 titanium alloy: A study using process map development, J. Alloys Compd. 695 (2017) 1706–1718. https://doi.org/10.1016/j.jallcom.2016.10.322.

[108] T. Kurzynowski, M. Madeja, R. Dziedzic, K. Kobiela, The effect of EBM process parameters on porosity and microstructure of Ti-5Al-5Mo-5V-1Cr-1Fe alloy, Scanning. 2019 (2019). https://doi.org/10.1155/2019/2903920.

[109] M.J. Mian, J. Razmi, L. Ladani, Defect analysis and fatigue strength prediction of as-built Ti6Al4V parts, produced using electron beam melting (EBM) AM technology, Materialia. 16 (2021) 101041. https://doi.org/10.1016/j.mtla.2021.101041.

[110] F.J. Humphreys, Characterisation of fine-scale microstructures by electron backscatter diffraction (EBSD), Scr. Mater. 51 (2004) 771–776. https://doi.org/10.1016/j.scriptamat.2004.05.016.

[111] L. Pelcastre, Microstructural Evolution of Ti-6Al-4V Alloy, Luleå University of Technology, 2008. https://doi.org/urn:nbn:se:ltu:diva-51162.

[112] X. Tao, An EBSD Study on Mapping of Small Orientation Differences in Lattice Mismatched Heterostructures, Lehigh Univ. 130 (2003) 556.

http://dx.doi.org/10.1016/j.jaci.2012.05.050.

[113] K.P. Mingard, M. Stewart, M.G. Gee, S. Vespucci, C. Trager-Cowan, Practical application of direct electron detectors to EBSD mapping in 2D and 3D, Ultramicroscopy. 184 (2018) 242–251. https://doi.org/10.1016/j.ultramic.2017.09.008.

[114] I. Weiss, S.L. Semiatin, Thermomechanical processing of alpha titanium alloys - An overview, Mater. Sci. Eng. A. 263 (1999) 243–256. https://doi.org/10.1016/s0921-5093(98)01155-1.

[115] K. Ma, H. Wen, T. Hu, T.D. Topping, D. Isheim, D.N. Seidman, E.J. Lavernia, J.M. Schoenung, Mechanical behavior and strengthening mechanisms in ultrafine grain precipitation-strengthened aluminum alloy, Acta Mater. 62 (2014) 141–155. https://doi.org/10.1016/j.actamat.2013.09.042.

[116] D. Junker, O. Hentschel, M. Schmidt, M. Merklein, Tailor-made forging tools by Laser Metal Deposition, Key Eng. Mater. 651–653 (2015) 707–712. https://doi.org/10.4028/www.scientific.net/KEM.651-653.707.

[117] R.J. Moat, A.J. Pinkerton, L. Li, P.J. Withers, M. Preuss, Crystallographic texture and microstructure of pulsed diode laser-deposited Waspaloy, Acta Mater. 57 (2009) 1220–1229. https://doi.org/10.1016/j.actamat.2008.11.004.

[118] M.J. Mian, J. Razmi, L. Ladani, Grain Scale Investigation of the Mechanical Anisotropic Behavior of Electron Beam Powder Bed Additively Manufactured Ti6Al4V Parts, Metals (Basel). 12 (2022). https://doi.org/10.3390/met12010163.

[119] S.V.S.N. Murty, N. Nayan, P. Kumar, P.R. Narayanan, S.C. Sharma, K.M. George, Microstructure–texture–mechanical properties relationship in multi-pass warm rolled Ti–6Al–4V Alloy, Mater. Sci. Eng. A. 589 (2014) 174–181. https://doi.org/10.1016/j.msea.2013.09.087.

[120] Y. Kim, Y.B. Song, S.H. Lee, Y.S. Kwon, Characterization of the hot deformation behavior and microstructural evolution of Ti-6Al-4V sintered preforms using materials modeling techniques, J. Alloys Compd. 676 (2016) 15–25. https://doi.org/10.1016/j.jallcom.2016.03.146.

[121] A. Townsend, N. Senin, L. Blunt, R.K. Leach, J.S. Taylor, Surface texture metrology for metal additive manufacturing: a review, Precis. Eng. 46 (2016) 34–47. https://doi.org/10.1016/j.precisioneng.2016.06.001.

[122] E. Morrison, A prototype scanning stylus profilometer for rapid measurement of small surface areas, Int. J. Mach. Tools Manuf. 35 (1995) 325–331.

https://doi.org/10.1016/0890-6955(94)P2390-2.

[123] C.Y. Poon, B. Bhushan, Comparison of surface roughness measurements by stylus profiler, AFM and non-contact optical profiler, Wear. 190 (1995) 76–88. https://doi.org/10.1016/0043-1648(95)06697-7.

[124] S. Interferometry, Good Practice Guide No . 116 The Measurement of Rough Surface, (n.d.).

[125] S.-W. Kim, G.-H. Kim, Thickness-profile measurement of transparent thin-film layers by white-light scanning interferometry, Appl. Opt. 38 (1999) 5968. https://doi.org/10.1364/ao.38.005968.

[126] Ambios Technology Inc., XP Series Stylus Profiler User 's Manual, Ambios. (2003). http://www.htskorea.com/product/ambios/manual.pdf.

[127] E.S. Gadelmawla, M.M. Koura, T.M.A. Maksoud, I.M. Elewa, H.H. Soliman, Roughness parameters, J. Mater. Process. Technol. 123 (2002) 133–145. https://doi.org/10.1016/S0924-0136(02)00060-2.

[128] M. Suraratchai, J. Limido, C. Mabru, R. Chieragatti, Modelling the influence of machined surface roughness on the fatigue life of aluminium alloy, Int. J. Fatigue. 30 (2008) 2119–2126. https://doi.org/10.1016/j.ijfatigue.2008.06.003.

[129] S.K. Ås, B. Skallerud, B.W. Tveiten, B. Holme, Fatigue life prediction of machined components using finite element analysis of surface topography, Int. J. Fatigue. 27 (2005) 1590–1596. https://doi.org/10.1016/j.ijfatigue.2005.07.031.

[130] M.J. Mian, J. Razmi, L. Ladani, Mechanical Behavior of Electron Beam Powder Bed Fusion Additively Manufactured Ti6Al4V Parts at Elevated Temperatures, J. Manuf. Sci. Eng. (2020). https://doi.org/10.1115/1.4049092.

[131] P.J. Withers, D. Grimaldi, C.K. Hagen, E. Maire, M. Manley, A. Du Plessis, X-ray computed tomography, Nat. Rev. Methods Prim. (n.d.). https://doi.org/10.1038/s43586-021-00015-4.

[132] L. Brabant, J. Vlassenbroeck, Y. De Witte, V. Cnudde, M.N. Boone, J. Dewanckele, L. Van Hoorebeke, Three-dimensional analysis of high-resolution X-ray computed tomography data with morpho+, Microsc. Microanal. 17 (2011) 252–263. https://doi.org/10.1017/S1431927610094389.

[133] A. Pierret, Y. Capowiez, L. Belzunces, C.J. Moran, 3D reconstruction and quantification of macropores using X-ray computed tomography and image analysis, 2002. https://doi.org/10.1016/S0016-7061(01)00127-6.

[134] A. Thompson, N. Senin, I. Maskery, R. Leach, Effects of magnification and sampling resolution in X-ray computed tomography for the measurement of additively manufactured metal surfaces, Precis. Eng. 53 (2018) 54–64. https://doi.org/10.1016/j.precisioneng.2018.02.014.

[135] H. Galarraga, D.A. Lados, R.R. Dehoff, M.M. Kirka, P. Nandwana, Effects of the microstructure and porosity on properties of Ti-6Al-4V ELI alloy fabricated by electron beam melting (EBM), Addit. Manuf. 10 (2016) 47–57. https://doi.org/10.1016/j.addma.2016.02.003.

[136] D. Greitemeier, F. Palm, F. Syassen, T. Melz, Fatigue performance of additive manufactured TiAl6V4 using electron and laser beam melting, Int. J. Fatigue. 94 (2017) 211–217. https://doi.org/10.1016/j.ijfatigue.2016.05.001.

[137] A. Mohammadhosseini, D. Fraser, S.H. Masood, M. Jahedi, Microstructure and mechanical properties of Ti–6Al–4V manufactured by electron beam melting process, Mater. Res. Innov. 17 (2014) s106–s112. https://doi.org/10.1179/1432891713z.000000000302.

[138] N. Hrabe, T. Gnäupel-Herold, T. Quinn, Fatigue properties of a titanium alloy (Ti–6Al–4V) fabricated via electron beam melting (EBM): Effects of internal defects and residual stress, Int. J. Fatigue. 94 (2017) 202–210. https://doi.org/10.1016/j.ijfatigue.2016.04.022.

[139] J.W. Pegues, N. Shamsaei, M.D. Roach, R.S. Williamson, Fatigue life estimation of additive manufactured parts in the as-built surface condition, Mater. Des. Process. Commun. 1 (2019) e36. https://doi.org/10.1002/mdp2.36.

[140] Titanium - Gerd Lütjering, James C. Williams - Google Books, (n.d.). https://books.google.com/books?hl=en&lr=&id=c9iR1Lm43GEC&oi=fnd&pg=PA4&dq=Titanium+Authors:+Lütjering,+Gerd,+Williams,+James+C.&ots=aIuMt1GbR3&sig=v0e2PtkPJzRe64ubK3_LzcPF1ak#v=onepage&q=Titanium Authors%3A Lütjering%2C Gerd%2C Williams%2C James C.&f=false (accessed January 30, 2020).

[141] R.I. Stephens, A. Fatemi, R.R. Stephens, H.O. Fuchs, Metal Fatigue in Engineering, 2001.

[142] R. Biswal, A.K. Syed, X. Zhang, Assessment of the effect of isolated porosity defects on the fatigue performance of additive manufactured titanium alloy, Addit. Manuf. 23 (2018) 433–442. https://doi.org/10.1016/j.addma.2018.08.024.

[143] J.P. Jing, Y. Sun, S.B. Xia, G.T. Feng, A continuum damage mechanics model on low cycle fatigue life assessment of steam turbine rotor, Int. J. Press. Vessel. Pip.

78 (2001) 59–64. https://doi.org/10.1016/S0308-0161(01)00005-9.

[144] B. Bhattacharya, B. Ellingwood, Continuum damage mechanics analysis of fatigue crack initiation, Int. J. Fatigue. 20 (1998) 631–639. https://doi.org/10.1016/S0142-1123(98)00032-2.

[145] F. Ahsan, J. Razmi, L. Ladani, Experimental measurement of thermal diffusivity, conductivity and specific heat capacity of metallic powders at room and high temperatures, Powder Technol. 374 (2020) 648–657. https://doi.org/10.1016/j.powtec.2020.07.043.

[146] Materials | Additive Manufacturing Research Group | Loughborough University, (n.d.). https://www.lboro.ac.uk/research/amrg/about/materials/ (accessed January 26, 2022).

APPENDIX A

MATLAB CODES

MATLAB code used for plotting the variation of mechanical properties with temperature:

```
%Plotting the variation of mechanical properties with temperatures

%Define variable
 clear all
 T=[200 400 600] %Temperature

 %Modulus of elasticity

 F_E=[ 103.22 87.88 72.74 ]

 err1=[1.02 2.08 1.83]

 S_E=[82.08 75.64 63.86]

 err2=[0.39 1.70 4.89]

 T_E=[85.59 71.63 63.74]

 err3=[3.29 2.83 3.57]

 %Yield strength

 F_YS=[864.81 622.68 392.06]

 err4=[5.96 8.79 15.20]

 S_YS=[665.70 514.28 354.60]

 err5=[26.86 11.27 11.77]

 T_YS=[623.30 412.43 338.78]

 err6=[9.38 3.76 18.8]

 %Ultimate tensile strength

 F_UTS=[870.65 701.87 495.23]

 err7=[7.97 13.44 11.09]

 S_UTS=[713.34 608.99 423.74]

 err8=[ 14.38 5.09 13.85]

 T_UTS=[677.14 514.34 392.28]

 err9=[7.08 5.76 15.16]

 %Percent elongation

 F_PE=[2.62 4.07 22.29]

 err10=[0.75 1.10 5.07]
```

```
 S_PE=[12.23 7.73 24.60]
 err11=[3.39 0.52 9.06]
 T_PE=[18.31 10.18 32.96]
 err12=[2.95 4.38 15.92]
%Plotting of graphs for UTS and percent elongation
 hold on
 box on
 yyaxis left
%  plot(T,F_UTS,'ro--', 'lineWidth',1)
 errorbar(T,F_UTS,err7,'ro--', 'lineWidth',1)
%  plot(T,S_UTS,'bs--', 'lineWidth',1)
 errorbar(T,S_UTS,err8,'bs--', 'lineWidth',1)
%  plot(T, T_UTS, 'kd--', 'lineWidth',1)
 errorbar(T,T_UTS,err9,'kd--', 'lineWidth',1)
 xlim([150 650])
 ylim([250 1050])
 yyaxis right
%  plot(T,F_PE,'mh-', 'lineWidth',1)
 errorbar(T,F_PE,err10,'mh-', 'lineWidth',1)
%  plot(T,S_PE,'g+-', 'lineWidth',1)
 errorbar(T,S_PE,err11,'g+-', 'lineWidth',1)
%  plot(T, T_PE, 'c*-', 'lineWidth',1)
 errorbar(T,T_PE,err12,'c*-', 'lineWidth',1)
 ylim('auto')
 yyaxis left
 xlabel('Temperature (°C)')
 ylabel('Ultimate Tensile Strength (MPa)')
 legend('Flat-built (UTS)',  'Side-built (UTS)',....
```

```
 'Top-built (UTS)','Flat-built (PE)',  'Side-built (PE)', ....
'Top-built (PE)', 'Location', 'North')
 yyaxis right
 ylabel('Percent Elongation (%)')
%Plotting graphs for Yield strength and modulus of elasticity
 hold on
 box on
 yyaxis left
 errorbar(T,F_YS,err4,'ro--', 'lineWidth',1)
 errorbar(T,S_YS,err5,'bs--', 'lineWidth',1)
 errorbar(T, T_YS,err6, 'kd--', 'lineWidth',1)
 xlim([150 650])
 ylim('auto')
 yyaxis right
 errorbar(T,F_E,err1,'mh-', 'lineWidth',1)
 errorbar(T,S_E,err2,'g+-','lineWidth',1)
 errorbar(T, T_E,err3,'c*-', 'lineWidth',1)
 ylim('auto')
 yyaxis left
 xlabel('Temperature (°C)')
 ylabel('0.2% Yield Strength (MPa)')
 legend('Flat-built (YS)',  'Side-built (YS)',.....
    'Top-built (YS)','Flat-built (E)',  'Side-built (E)',.....
    'Top-built (E)', 'Location', 'NorthEast')
 yyaxis right
 ylabel('Modulus of Elasticity (GPa)')
            %End of Code%
```

MATLAB code used for fatigue limit calculation:

```
% Fatigue limit prediction from surface profile data
% Define variable
depth=a; % peak to valley height, a (extracted from the surface profile).
pitch=2b; % peak to peak length, 2b (extracted from the surface profile);
%Calculations
r=depth/pitch % r=a/2b;
HV =X; % hardness value, top build: X=248, side build: %X=310, flat build: X=382;
alpha=0.226+HV*10^-4;
R=-1 (or 0.1); % R=Sigma_min/Sigma_max;
if r > 0.194
   sqrt_area=0.38*pitch; %r> 0.194;
else
   sqrt_area=(2.97*r-3.51*r^2-9.74*r^3)*pitch; %r<0.194
end
SigmaW=(1.43*(HV+120)/(sqrt_area)^(1/6))*((1-R)/2)^alpha
sqrt=sqrt_area
Sigma=SigmaW
                  %End of code%
```